



In-operando degradation studies of zirconia electrolyte supported solid oxide cells under harsh operating conditions

Sierra Trujillo, Jose Xavier

Publication date:
2018

Document Version
Publisher's PDF, also known as Version of record

[Link back to DTU Orbit](#)

Citation (APA):
Sierra Trujillo, J. X. (2018). *In-operando degradation studies of zirconia electrolyte supported solid oxide cells under harsh operating conditions*. Technical University of Denmark.

General rights

Copyright and moral rights for the publications made accessible in the public portal are retained by the authors and/or other copyright owners and it is a condition of accessing publications that users recognise and abide by the legal requirements associated with these rights.

- Users may download and print one copy of any publication from the public portal for the purpose of private study or research.
- You may not further distribute the material or use it for any profit-making activity or commercial gain
- You may freely distribute the URL identifying the publication in the public portal

If you believe that this document breaches copyright please contact us providing details, and we will remove access to the work immediately and investigate your claim.

In-operando degradation studies of zirconia electrolyte supported solid oxide cells under harsh operating conditions

Ph.D Thesis

José Xavier Sierra Trujillo

Supervisors:

Senior Researcher: Jacob Ross Bowen

Professor: Henning Friis Poulsen

Senior Researcher: Peter Stanley Jørgensen

Department of Energy Conversion and Storage

Technical University of Denmark



Roskilde, Denmark

December, 2018

Preface

This thesis is the product of three years of studies, from June 2015 to July 2018 at the Department of Energy Conversion and Storage at the Technical University of Denmark, in complete fulfillment of the requirements for a PhD degree. The project focused on the study of the degradation occurring in solid oxide cells at operating conditions and challenging experiments were carried out at European Synchrotron Radiation Facility (ESRF), complemented by experiments performed at DTU Risø laboratories. The travels related to beamtimes were financed by DanScatt and Interreg.

In the first chapter an introduction to the solid oxide cells and its basic principles is given. In Chapter 2 some of the most common characterization techniques to study these systems are presented, introducing a new promising technique based on X-ray diffraction. Later chapters contain the motivation, results and discussion of the two main experiments.

Acknowledgements

During all these three amazing years, I have been supported by many people. First, I would like to thank to my family that were the first contributors to this work. My mother for spoiling me since the beginning and giving me the best advice. My father... specially my father for loving me beyond limits, and despite he is not here with us anymore I know that he is still loving me with all his heart and feeling proud of me, as his only child. To Mary for having the greatest patience during my worse and frustrating days and taking care of me as the best wife and guardian angel in my life.

I want to also thank to all my friends at work, that in many cases supported me with good ideas and specially for relaxing time, which is of extreme importance to achieve good performance. The Italian group, or better said, the Italian mafia that is always increasing in people. Simon for giving me one of my first enjoyable conversations during my first days. Ilaria, Elisa, Stefano and others Italians for having a lot of fun and letting me practice their language and vice versa. My dear beloved Peyman, Yu Xu and Grichar, who with their daily discussions during lunch time made me forget most of my work related problems. And Rocío for being a good friend to me and my wife.

I want to express my gratitude to all the people of this department who participated directly in this work. Ebtisam Abdellahi, Annelise Mikkelsen, Pernille Hedemark Nielsen, John Johnson, Rune E. Johnsen, Karen Brodersen, Jens Østergaard, Lene Knudsen, Søren Koch, Karl Tor Sude Thydén, Karin Vels Hansen, Torben Jacobsen, Mogens Bjerg Mogensen, Poul Norby, Ming Chen, Tiago Ramos and Janet Jonna Bentzen for helping me in the sample preparation, experimental setup, electronic microscopy and provided me with fruitful conversations that illuminated me when I was struggling with data analysis.

Many thanks to Carsten Detlefs, Phil Cook and Can Yildirim for supporting me during beamtimes and data analysis, especially during my three months of external stay at the ESRF, which I really enjoyed and learn about synchrotrons, despite spending many hours without sleeping !!! I also include here to Hugh Simon, who contributed enormously to the experiments and data analysis from synchrotron days.

To Kent K. Hansen and Christodoulos Chatzichristodoulou for accepting and giving the special courses proposed in the study plan for this PhD.

To my dear head of section, Luise Theil Kuhn that was always taking care of me and worried about my life as a student in this great place. Thanks for sharing productive moments that make my stay here easier. Thanks also to the secretaries, especially Lene Christensen and Lotte Mongaard who helped me infinitely before and after arriving at this place and for being so gentle.

And if “by coincidence” my supervisors are reading this, please don’t worry, I can never forget you. If I would one day express all my gratitude to you, for sure it will take longer than this thesis. There are not enough words to say “Thank you”, not even in Spanish, English and Danish combined. Thank you for being so supportive and sharing with me fantastic and “crazy” ideas that ended up being crucial for the fulfillment of the thesis. Thanks for accompanying me in and spending long nights during beamtimes and for having the patience to teach me and transfer me part of your knowledges that have made me improve substantially as a personally and as a scientist. Without you this work could never have been achieved and besides being the supervisors, I also consider you as authors of this work.

Thanks to all of you who have contributed in one way or another to the realization of this thesis.
and..... See you... Vi ses... Nos vemos !!!



José Xavier (Tato)

Roskilde, Denmark, July 2018

Abstract

Solid oxide cells are promising systems for energy production and storage. One of the advantages is the capability to work in cyclic mode, where they can efficiently generate electricity by an electrochemical reaction involving fuel and oxygen, and in reverse mode hydrogen and oxygen can be obtained, in which hydrogen can be used later as a fuel. Due to the harsh working conditions, they exhibit degradation, which is detrimental to the performance and lifetime of the cells.

In this work, *in-operando* studies on the degradation of Zirconia electrolyte based cells under harsh working conditions are carried out. To conduct such study, powerful characterization tools, like scanning electron microscopy/energy dispersive spectroscopy, electrochemical impedance spectroscopy and X-ray diffraction are combined to provide valuable information on the degradation mechanisms observed in the experiments. Moreover, here we introduce dark field X-ray microscopy as a novel technique for mapping the structure of individual grain. The achievements of the experiments are based upon the development of a novel sample fabrication method, enabling microstructural studies as a function of position across the cell. Furthermore, challenging sample stage is design to provide the required working conditions.

This work can be divided into two major experiments regarding the type of electrolyte: ScYSZ and YSZ. In the former, several individual experiments are carried out on symmetrical YSZ electrolyte based cell with LSM/YSZ electrodes, to evaluate the influence of void formation on the electrolyte from a statistical point of view, given by extensive *post-mortem* electron microscopy. The cells are tested at high temperatures in air and at high polarization. Furthermore, electrochemical impedance spectroscopy is performed on cells showing higher degradation, due to grain size, at equivalent working conditions to provide essential electrochemical information for understanding internal process in the cell. In order to overcome the problem of grain statistics in X-rays studies, classical X-ray powder diffraction is replaced by strain mapping using multigrain crystallography methods. In addition, on the grain scale, strain mapping is performed on one diffracting electrolyte grain in the region of interest, demonstrating the capabilities of such tool on the local microstructural characterization of individual elements deeply embedded in the material.

In the second major experiment, YSZ electrolyte based cell with Ni/YSZ and Pt electrodes is built on the basis of the experience gained in the previous experiments. A novel sample stage is developed as an essential component for supporting the experiment, enabling gas environment at high temperature and polarization. Electrochemical impedance spectroscopy and X-ray diffraction are performed simultaneously, and elemental composition assessment is carried out *post-mortem* to complement the observations. Although the experiment was not completely successful, the results are discussed in terms of the findings and the major problems experienced.

Dansk Resumé

Fastoxidceller er lovende systemer til energi konvertering og lagring. En af fordelene er cellernes evnen til at arbejde cyklisk, hvor de effektivt kan generere elektricitet ved en elektrokemisk reaktion der involverer brændstof og ilt, og i omvendt tilstand kan generere hydrogen og ilt fra elektricitet, hvorved hydrogen kan bruges senere som brændstof. På grund af de hårde driftsbetingelser nedbrydes de over tid, hvilket er skadeligt for cellernes ydeevne og levetid.

I dette arbejde udføres *in-operando* undersøgelser af nedbrydning af Zirconia-elektrolytbaserede celler under hårde arbejdsvilkår. For at gennemføre en sådan undersøgelse kombineres kraftige karakteriseringsværktøjer, såsom scanningelektronmikroskopi / energidispersionspektroskopi, elektrokemisk impedansspektroskopi og røntgendiffraction for at tilvejebringe værdifuld information om de nedbrydningsmekanismer, der observeres i forsøgene. Herudover introducerer vi mørkt felt røntgenmikroskopi som en ny teknik til kortlægning af strukturen af individuel korn. Resultaterne af forsøgene er baseret på udviklingen af en ny prøvefremstillingsmetode, der muliggør mikrostrukturelle undersøgelser som en funktion af position på tværs af cellen. Desuden er udfordrende prøvefase design for at give de nødvendige arbejdsvilkår.

Dette arbejde kan opdeles i to større eksperimenter vedrørende typen af elektrolyt: ScYSZ og YSZ. I det første udføres flere individuelle eksperimenter på symmetrisk YSZ elektrolytbaseret celle med LSM / YSZ-elektroder for at evaluere indflydelsen af huldannelse på elektrolytten ud fra et statistisk synspunkt, givet ved omfattende post-mortem-elektronmikroskopi. Cellerne testes ved høje temperaturer i luft og ved høj polarisering. Desuden udføres elektrokemisk impedansspektroskopi på celler, der viser højere nedbrydning på grund af kornstørrelse ved ækvivalente arbejdsvilkår for at tilvejebringe væsentlige elektrokemiske oplysninger til forståelse af intern proces i cellen. For at overvinde problemet med kornstatistikker i røntgenstudier erstattes klassisk røntgenpulverdiffraction med stamkortlægning ved anvendelse af multigrain-krytallografi-metoder. Derudover udføres på stammen skalaen på et diffraktionselektrolytkorn i området af interesse, hvilket viser kapaciteten af et sådant værktøj på lokal mikrostrukturel karakterisering af individuelle elementer dybt indlejret i materialet.

I det andet større eksperiment bygges YSZ-elektrolytbaseret celle med Ni / YSZ og Pt-elektroder ud fra erfaringerne fra de tidligere eksperimenter. En ny prøve fase er udviklet som en væsentlig

komponent til at støtte eksperimentet, hvilket muliggør gasmiljø ved høj temperatur og polarisering. Elektrokemisk impedansspektroskopi og røntgendiffraktion udføres samtidigt, og elementskompositions vurdering udføres efter mortem for at komplementere observationerne. Selv om eksperimentet ikke var helt vellykket, diskuteres resultaterne med hensyn til resultaterne og de store problemer, der opstår.

Table of Contents

1.	Introduction	1
2.	Solid Oxide Cells	4
2.1	Solid Oxide Fuel Cell	4
2.2	Solid oxide electrolyzer cell	6
2.3	Triple Phase Boundaries	8
2.4	Void formation	8
2.5	Electrolyte materials	10
2.5.1	Doping with Scandia	12
2.6	Electrode properties.....	12
2.7	Electrodes materials.....	13
2.7.1	Fuel electrode.....	14
2.7.2	Oxygen electrode	14
2.8	Electrolyte structure.....	15
2.8.1	Structure of ZrO ₂	15
2.8.2	Ionic conductivity	17
2.8.3	Chemical expansion.....	19
3.	Characterization methods in SOCs	21
3.1	Scanning Electron Microscopy (SEM)	21
3.2	Electrochemical Impedance Spectroscopy (EIS).....	22
3.3	X-ray diffraction.....	24
3.3.1	Mosaicity	26
3.3.2	Strain	27
3.3.3	Synchrotron radiation	28
3.3.4	Dark Field X-ray Microscopy.....	28
3.3.5	Thermal expansion	31
4.	Evolution of void formation on ScYSZ grain boundaries in symmetrical LSM/YSZ – ScYSZ cells	
4.1	Introduction to the chapter.....	33
4.2	Materials and sample preparation	34
4.2.1	Electrolyte material	34
4.2.2	Electrode material	35
4.2.3	Cell components and assembly	36
4.3	<i>Void statistic</i> experiments	37

4.3.1	Electron microscopy	38
4.3.2	EDS analysis	38
4.3.3	EIS analysis	38
4.4	<i>In-operando</i> experiment	39
4.5	Results	43
4.5.1	Grain size of electrolyte.....	44
4.5.2	Characteristics of void formation close to the anode/electrolyte interface	45
4.5.3	EDS to a highly degraded cell	47
4.5.4	Statistics of void formation	49
4.5.5	Evolution of R_s and R_p	52
4.5.6	Evolution of pO_2	57
4.5.7	<i>In-operando</i> study of grain-averaged electrolyte d-spacing change	59
4.5.8	<i>In-operando</i> mapping of the strain evolution within a ScYSZ grain.....	60
4.5.9	TEC measured by DFXRM	62
4.5.10	Characterization of grain boundary void formation after operation	63
4.6	Discussion	64
4.6.1	Conditions and factors influencing void formation	64
4.6.2	Microstructural changes close to the anode/electrolyte interface.....	66
4.6.3	d-spacing decrease close to the cathode/electrolyte interface	67
4.7	Conclusions.....	69
5.	<i>In-operando</i> experiment on YSZ electrolyte based cell with Ni/YSZ cathode under high polarizations.....	71
5.1	Introduction to the chapter.....	71
5.2	Sample and sealing.....	72
5.2.1	Sample materials	73
5.2.2	Sintering of electrodes and reducing NiO	73
5.2.3	Sample fabrication and mounting	74
5.2.4	Quartz tube	75
5.2.5	Assembling the components	76
5.3	Experimental setup	78
5.3.1	Sample stage	78
5.3.2	IR furnace	80
5.3.3	Beamline configuration	81
5.4	Experimental procedure.....	83

5.4.1	Data analysis.....	86
5.5	Results and discussion.....	88
5.5.1	<i>Post-mortem</i> EDS.....	88
5.5.2	Evolution of current.....	92
5.5.3	Evolution of R_s and R_p	95
5.5.4	Interface position	97
5.5.5	Phases in XRD	101
5.5.6	Strain in Ni and YSZ close to the electrode/electrolyte interface	105
5.5.7	Mosaicity	108
5.6	Discussion.....	111
5.6.1	Partial reduction of NiO.....	111
5.6.2	“Dark” layers between Ni/YSZ electrode and Pt paste.....	112
5.6.3	R_s and R_p	112
5.6.4	Similar findings to another report.....	113
5.6.5	Strain mapping	114
5.7	Conclusions.....	114
6.	Summary and Outlook.....	117
6.1	Summary and conclusions.....	117
6.2	Outlook.....	119
7.	Bibliography	122
8.	Abbreviations	130
9.	Appendix	131
9.1	Notes about experiments and data analysis	131

1. Introduction

It is known that the energy produced by fossil fuels will end eventually; in addition, the combustion of fuels leads to chemical residues that usually are released to the atmosphere and are potentially harmful to life on our planet. Consumption of energy is increasing yearly and is imperative for the society to find better and more attractive alternatives. Many efforts have been made in order to develop technologies to generate energy in a sustainable way. Among the most common ways solar and wind power are getting high acceptance, although there are many other interesting alternatives, like biomass, hydropower, geothermal, etc. These are known as renewable energies since the produced energy comes from renewable sources.

Solid Oxide Cells (SOCs) is becoming also a promising technology to efficiently generate power from fuel by an electrochemical reaction and vice versa. This kind of system can work in two modes: fuel and electrolysis modes and its efficiency has been demonstrated to be higher than standard engine combustion when running in fuel mode and for hydrogen and oxygen production in electrolysis mode (1). Typically, when running in fuel mode, hydrogen and oxygen directly produce electricity by an electrochemical reaction, with water as the main residual product, being this one of the most interesting advantages, since it contributes to a much cleaner energy generation. In electrolysis mode, high purity hydrogen and oxygen are split from water by the reverse reaction, where hydrogen can be stored as a fuel for later use in fuel mode (2) (3) (4) (5) (6). Cycling between fuel and electrolysis mode has been of great concern since the lifetime has been reported to increase significantly compared to single mode use (7). When used in fuel and electrolysis modes they are commonly referred to the kind of cell, which are called: solid oxide fuel cell (SOFC) and solid oxide electrolyzer cell (SOEC).

However, due to the harsh operating conditions at which the SOCs work, they exhibit degradation (8) (9) (10), which negatively impacts on the performance and lifetime of these systems. Several degradation mechanisms have been extensively studied and reported in the literature, according to the characteristics of the materials, environmental conditions (temperature, gas, polarization) and working mode (fuel or electrolysis). It is also said that the major degradations occur in

electrolysis mode (11). Void formation in grain boundaries, porosity inside dense structures, segregation of phases, cracks, delamination, formation of nanoparticles, oxidation and reduction of metallic phases, particle coarsening, etc. are examples of a long list of degradations reported in the literature (7) (8) (9) (10) (12) (13) (14).

Understanding degradation mechanisms in SOCs is crucial when it comes to improve their performance and lifetime. Studying these systems involve the use of several techniques for materials characterization. Common and powerful techniques are, for example, X-ray diffraction (XRD), Electrochemical Impedance Spectroscopy (EIS), Scanning Electron Microscopy (SEM) and its alternatives, like Energy Dispersive X-ray Spectroscopy (EDS). Other non-common techniques can be found in large and special facilities, for example based on X-ray radiation, like synchrotron facilities, with brilliances so extreme that cannot be found in commercial devices.

Post-mortem studies have been widely used in general and also applied to SOCs (15) (16), in which the results are based on the initial and final characteristics of the sample. However, *in-situ* and *in-operando* studies offer a much better overview regarding the processes occurring in “real time”, with the possibility of detecting intermediate processes that are not possible to see in *post-mortem* studies. In SOCs, due to their variety of materials and working conditions, chemical and physical processes are of extreme complexities and could evolve in different time scales. Thus, the evolution of specific characteristics related to the investigated system is a key factor on understanding the processes, including the expected electrochemical reactions and unexpected behavior related to degradation mechanisms.

Therefore, in an attempt to answer the questions of degradation mechanisms, in this work we emphasized on *in-operando* studies on solid oxide cells under harsh working conditions, by simultaneously combining powerful techniques and presenting novel methods for X-rays. The experiments were achieved upon the development of unique methods of sample fabrication and novel design of sample stage, in order to provide the required working conditions. Furthermore, in this research we describe the first use of *in-operando* multiscale Dark Field X-ray Microscopy (DFXRM), a synchrotron based equivalent of a transmission electron microscope, to study microstructural evolution of a solid oxide cell (SOC) electrolyte during degradation.

In general, this work is divided into two major experiments. The first main experiment is based on the assessment of the void formation evolving in the grain boundaries of Yttria Stabilized Zirconia (YSZ) based cell, with a symmetrical configuration with Lanthanum – Strontium – Manganate (LSM) composites as electrodes under a temperature range between 700 and 900 °C at a polarization of 2V in air. The second main experiment involves the study of a YSZ electrolyte based cell with Ni/YSZ and Platinum (Pt) electrodes in a reducing atmosphere of wet 5% H₂ in N₂ at 650 °C and at polarization up to -1.8V during almost 40 hours.

For a better understanding of this work, a brief description of the thesis layout is given below.

In Chapter 2 an introduction to the working principles of SOFC and SOEC is given, focusing later on electrolysis mode. Common materials used in SOCs are mentioned, including some of the main properties and the role they play in SOEC. Furthermore, a description focused on the relation between the structure and the working principle of the electrolytes used in this work, is provided.

In Chapter 3 a description of the characterization methods used in this work is given, covering basic introduction to XRD, SEM, and EIS. Moreover, a novel technique based on X-ray diffraction microscopy, known as Dark Field X-ray Microscopy (DFXRM) is presented as a promising method to non-destructively characterize the evolution of strain domains on isolated grains in the structure.

In Chapter 4 the motivation of the first main experiment, with the materials used to build the cells are described in the initial sections. Later sections containing the results and discussion are given, based on the synergy provided by the used techniques. Part of the results of this chapter has been currently accepted for publication.

In Chapter 5 the main motivation of the second experiment is presented. Then, we emphasize on the challenges of the sample preparation and experimental setup, followed by the experimental procedure and description of the data analysis. Finally, the results are presented, along with some discussion focused on the major findings and problems of the experiment.

Chapters 6 and 7 contain the overall conclusions, summary and outlook of this work.

2. Solid Oxide Cells

2.1 Solid Oxide Fuel Cell

Solid oxide cells working in fuel mode are systems that directly produce electricity by an electrochemical reaction (6). In fuel mode the reaction consists of the oxidation of fuel, which can be hydrogen (H_2) and/or carbon monoxide (CO). The exothermic electrochemical oxidation of the oxide ions with the fuel takes place at the anode side. Fuel gas diffuses into the porous anode, reaching the triple phase boundaries where it combines with oxide ions coming from the reduction of oxygen gas molecules at the cathode side and transported by the dense electrolyte, producing electrons, water in steam form and/or carbon dioxide (CO_2). The steam and CO_2 are diffused back through the anode and entering the fuel stream and the produced electrons are then transferred through the conducting anode to the interconnects, and if the electrodes are electrically connected through an external circuit, a current/electricity is produced and electrons reach the cathode side to reduce again oxygen gas molecules to continue the electrochemical reaction. In Figure 2.1 is represented the main components and the basic processes of a SOFC (metallic interconnects are not shown but they are in contact with the electrodes).

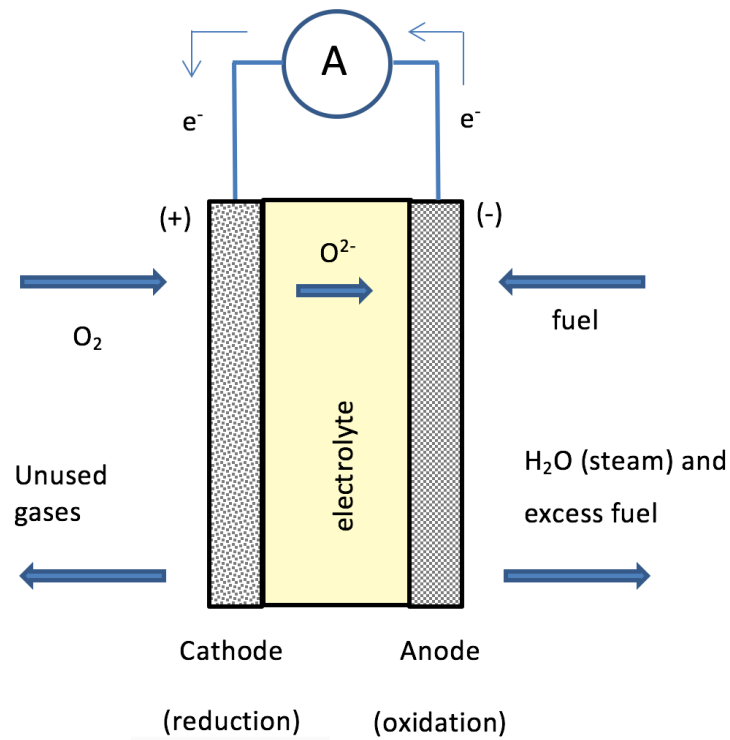
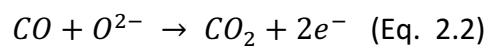
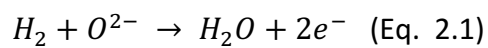
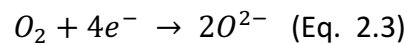


Figure 2.1. Schematic view of a SOFC. Oxide ions move inside the electrolyte from the cathode to the anode. Electrons produced by the oxidation at the anode can travel to an external circuit, generating a potential difference.

The overall reaction at the anode side can be represented as (17):



And the reaction at the cathode side:



2.2 Solid oxide electrolyzer cell

A solid oxide electrolysis cell (SOEC) can be seen as the reverse process of a SOFC. A potential difference is applied to the electrodes and the electrolysis of water and/or CO₂ is achieved to produce H₂ and/or CO and O₂ (6).

The components, materials and working temperature of SOEC are similar to as SOFC. Actually, solid oxide cells have been tested in cycling mode (fuel and electrolysis mode) , where degradation process have been found to reduce significantly compared to degradation when using the cell either in fuel mode or electrolysis mode independently (7) (18), thus increasing drastically the lifetime of these systems.

The reaction of SOEC, as opposed to SOFC, can be described as follow:

Water in steam form and/or CO₂ is supplied to the cathode side, where they split into oxide ions and hydrogen and/or CO due to the electrons coming from the power source. Oxide ions are transported through the electrolyte, from the cathode to the anode driven by the applied potential, reaching the anode/electrolyte interface, where they oxidize, producing oxygen molecules O₂ and electrons, which are then conducted to the external circuit. In Figure 2.2 is represented the main components and the basic processes of a SOEC.

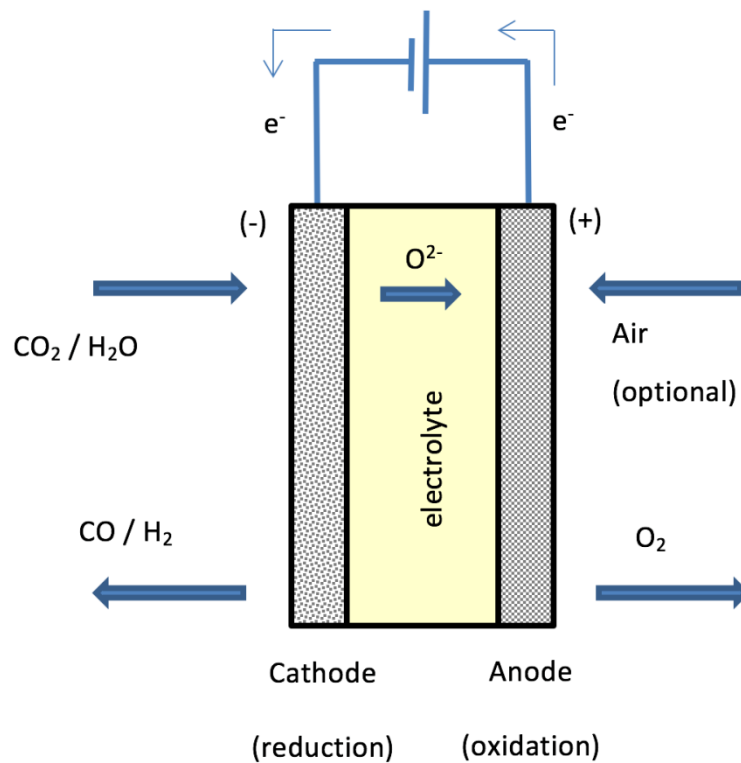
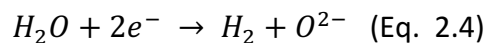
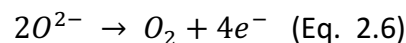


Figure 2.2. Schematic view of a SOEC. An external voltage is applied to create the conditions for the electrochemical reaction.

The equation of the mentioned reaction can be show as (5) (19), where at the cathode side:



And at the anode side:



The final products at the cathode side: H_2 and/or CO can be easily stored for later use as fuels in SOFC. Up to date electrolysis is considered the most promising method to produce pure H_2 from H_2O because of the relatively low cost in comparison to other methods, like thermomechanical and photocatalytic, and its very high efficiency of conversion. Moreover the oxygen gas generated at the anode side is also of high purity.

2.3 Triple Phase Boundaries

The triple phase boundary (TPB) is the region where the three phases involved in the electrochemical reaction meet, as shown in the regions marked with red circles in Figure 2.3. These three phases are: electrolyte, electrode and a gaseous phase. The ionic and electronic conductivities are provided by the electrolyte and electrodes respectively and the porosity of the electrodes allows the gases diffuse to reach the TPB. As mentioned above, adding YSZ to electrodes composites enhance the ionic conductivity and increase the TPB length, thus the performance of the cell (20) (21) (22) (23).

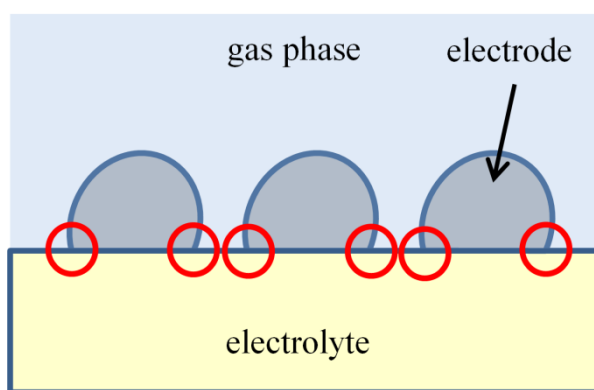


Figure 2.3. Schematic view of triple phase boundaries (TPB). TPB are marked with small red circles in which the electrolyte, electrode and the gas phase are in contact.

2.4 Void formation

Solid oxide cells in general exhibits degradation mechanisms attributed mainly to the harsh working conditions. It has been reported that in electrolysis mode is where the major degradation occurs compared to fuel mode (5), mostly due to the oxygen electrode. Delamination of electrolyte/oxygen electrode interface, internal cracks and void formation in the electrolyte has been observed in long term experiments under high current densities (10) (8) (7).

In Knibbe et al. (8) they discovered intergranular and transgranular fractures running along the YSZ grain boundaries and the formation of pores in the grain boundaries of an YSZ electrolyte based cell. The fuel and oxygen electrodes consisted of Ni-YSZ and LSM-YSZ and the cell was tested at 850 °C for 188 hours under a current density of -2 A/cm^2 . Energy dispersive X-ray spectroscopy (EDS) revealed the composition of the entrapped gas to be mainly oxygen.

Similar pore formations and transgranular fractures were observed after 9000 hours at a current density of -1 A/cm^2 by (10) in micrographs of fractured surfaces. The cell consisted of an 8%mol-YSZ electrolyte and a porous diffusion barrier layer of gadolinia doped Ceria (CGO) with lanthanum strontium cobalt ferrite (LSCF) and Ni/YSZ as the oxygen and fuel electrodes respectively.

Also cracks, detachment and cavities close to the anode interface were observed by Sun et al. (24) by means of SEM in the polished cross-section of cells with similar electrode/electrolyte composition as in Knibbe et al. (8) after 900 hours at 850 °C and -1.5 A/cm^2 .

In Graves et al. (7), by means of scanning transmission electron microscopy they observed nanosized pores in YSZ electrolyte grain boundaries of a cell composed of the same electrode materials as in Knibbe et al. (8) in electrolysis mode after 420 hours at 800 °C and -1 A/cm^2 .

This formation of porosity in the grain boundaries of the electrolyte close to the oxygen electrode/electrolyte interface has been proposed to be due to an increase in oxygen activity, caused by the distribution of the electromotive potential and resulting in an oxygen build up in this region (8) (25) (12).

Therefore, from a logical point of view it is expected that the high oxygen pressure results in compressive stresses and thus a reduction of electrolyte lattice parameter close to the anode interface. Void formation can negatively impact the performance and lifetime, therefore understanding the mechanisms could mitigate significantly the issues related to it; however, the mechanism of formation of voids has not been well studied yet. Direct observation is difficult due to the limitations dictated by the high temperature, gas atmosphere, geometry of the system and nanometric size of the pores.

The capabilities of X-ray to penetrate and see deep inside objects in a non-destructive way have been widely exploited. 3D imaging techniques, like X-ray nanotomography has been used to study the microstructural properties of Ni-YSZ cermet as SOFC anode with a high resolution voxel size of

25 nm (26). Moreover ex-situ studies of Ni-YSZ cermet were performed by high resolution ptychographic nanotomography, achieving spatial resolution of 55 nm in voxel size (27) (14). Other techniques, like X-ray Absorption Near Edge tomography and X-ray holo-tomography are also capable to reconstruct the SOC 3D microstructure with a resolution close to 50 nm (27).

Despite the relatively high resolution achieved by these state-of-the-art imaging techniques, they are yet not powerful enough to fully detect nanosized void formation; in the best case they can detect the bigger voids, which typically have a size of approximately 100 nm or more but these are believed to be the voids at the latest stages and should not represent the initial stage of void formation.

SEM and/or TEM are also very powerful and widely used techniques to detect features within few nanometers resolution, but due to the microscopy configuration is not possible to look inside the cell during operando conditions. X-ray diffraction could provide indirect information of the void formation inside the electrolyte and in addition, there is a new technique currently in development known as Dark Field X-ray Microscopy, capable to zoom in into independent diffracting grains with possibility to perform strain mapping and mosaicity studies (28) (29) (30).

2.5 Electrolyte materials

The electrochemical cell based on solid oxide materials is basically composed by an electrolyte in contact with two electrodes: anode and cathode with a fuel and oxidant elements continuously supplied. Interconnectors or current collectors are included in the system to allow the electronic current to flow through to an external circuit. In general, the material used as electrolyte in SOC applications must meet some crucial requirements for satisfactory performance (20) (10) (31) (8) (25) (6):

- good ionic conductivity and negligible electronic conductivity at the operating temperature, as the ions are the responsible for charge transport between electrodes, promoting the electrochemical reaction.

- high chemical stability under high temperature, as the material is exposed to high oxidizing and reducing environments, and negligible chemical interaction with electrodes during operating and fabrication conditions to avoid the formation of blocking interface phases.
- Suitable mechanical properties to withstand external forces when producing in stacks.
- High density to avoid permeation of gases across it.
- Thermal expansion coefficient similar to the electrodes to prevent the formation of cracks and other structural defects during heating from ambient temperature to operating temperature.
- Ability to fabricate thin layers in order to minimize ohmic losses (in electrolyte supported cells and anode supported cells the electrolyte thickness is typically in the range of 50-150 μm and 5-20 μm respectively).

Among the materials with high ionic conductivity are: zirconia, ceria and bismuth oxide based materials. The latest shows an ionic conductivity even higher than zirconia based materials, but its chemical instability at high temperatures in reducing atmospheres, high corrosion activity, low mechanical strength and relatively easy decomposition into bismuth metal makes it not very well suitable for electrolyte applications (32) (33) (34) (35). Ceria based materials are widely used as electrolyte in SOCs systems because of its higher conductivity than zirconia based, in particular at lower temperatures. A very common dopant used in ceria based ceramics is gadolinia, where the material is known as CGO. The disadvantages of ceria doped materials as electrolyte are from the partial reduction of Ce^{4+} to Ce^{3+} at reducing conditions of the anode, resulting in an increase of electronic conductivity and mechanical failure due to expansion of the lattice (35) (36).

Besides ceria based ceramics, zirconia based materials are also extremely wide used as electrolyte. Zirconia is typically doped with other oxides and the structure is stabilized at room temperature (6) (37) (38), providing suitable properties for SOCs application due to its high ionic conductivity in opposite to low electronic conductivity, as well as its high chemical and structural stability and resistance to oxidizing and reducing atmospheres under typical operating temperatures, 800 - 1000 $^{\circ}\text{C}$ (39) (40) (41). Yttria Stabilized Zirconia, known as YSZ, is considered practically the best option in terms of cost effectiveness as dopant for ZrO_2 , and when doped with Scandia, ScYSZ, offers better ionic conductivity at lower temperatures. Therefore, Yttria (Y_2O_3) and Scandia (Sc_2O_3)

are used as dopants for ZrO_2 in electrolytes based cells in the experiments of this work. Among other oxides used to dope ZrO_2 are Sm_2O_3 and Yb_2O_3 .

2.5.1 Doping with Scandia

Doping ZrO_2 by Scandia (Sc_2O_3) is a well-known method to enhance significantly its ionic conductivity compared to 8YSZ when used as electrolyte in SOCs. This composite is known as Scandia Stabilized Zirconia (ScSZ). Higher ionic conductivities may result in a decrease of the working temperature of the system, thus having a positive impact regarding lifetime, design and costs (40). Despite Scandia is considered an expensive material, this is now changing as availability is increasing from other countries and price is reducing (42). However, ScSZ is not stable below $650\text{ }^\circ\text{C}$ and also, due to aging effects, tetragonal phase forms in the cubic matrix at high temperatures. Co-doping Scandia and Yttria with ZrO_2 has been reported to suppress the decrease in conductivity with aging in the high temperature range, typically $800\text{-}1000\text{ }^\circ\text{C}$, especially for low Yttria concentrations of 1-2%mol and Sc concentrations of 9-10%mol (38) (43).

Because of the suitable properties of co-doped Scandia and Yttria with ZrO_2 exhibited as electrolyte in terms of structural and chemical stability and ionic conductivity, we decided to use it as a part of the experimental research on this work. The preparation method and structural properties of the specific material used are addressed later in experimental section.

2.6 Electrode properties

The materials used as electrodes in solid oxide systems have to fulfill certain conditions in order to maximize the efficiency and structural properties. The main conditions are listed below (44):

- Thermal expansion coefficient: One of the major problems in building a solid oxide cell is to achieve a suitable thermal expansion coefficient between the components, since they are going to be sintered at very high temperature, usually above $1000\text{ }^\circ\text{C}$ and moreover its operating temperature conditions is commonly between 800 and $1000\text{ }^\circ\text{C}$. Mismatch of thermal expansion coefficient when rising up the temperature is known to result in cracking at the interface of different materials. Thus, electrodes and electrolyte must have

a very close thermal expansion coefficient in order to adhere to each other without failure (17) (45) (46) (47).

- Chemical stability and compatibility: since solid oxide cells are made to last several thousands of hours and/or more under extreme degradation conditions, like high temperature, oxidizing and reducing atmospheres, materials have to withstand these requirements as long as possible without any major structural and chemical changes. Moreover, electrode materials must have low chemical reaction rate with the other components, like electrolyte and interconnects (45).
- Porosity: In order to let the gases diffuse into the electrode to participate in the electrochemical reaction, electrodes need to have an adequate porosity (17). Too low porosity can act as more obstacles for gases to flow from electrodes to electrolyte interface due to a denser structure and high porosity can result in a decreasing region for the reaction to take place.
- Conducting properties: in addition to the above, electrode materials have to be a good electronic conductor in order to transport the electrons to and from the regions where the electrochemical reaction occurs and to the interconnects. It is also desirable to have proper ionic conductivity to increase the active regions of the electrochemical reaction (17) (6).

Other examples of the properties of electrodes are tortuosity and percolation, but they are not discussed here in this work.

2.7 Electrodes materials

Several materials and compounds are currently used as electrodes. As discussed in next sections, electrodes can be classified in anode and cathode, where oxidation and reduction occurs respectively or oxygen electrode and fuel electrode, specifying where the reactants participate in the electrochemical reaction.

2.7.1 Fuel electrode

Ni is currently one of the most common materials used as fuel electrode due to its relatively low cost, high electrical conductivity and electrocatalytic activity (5). However, in order to improve the adhesion to the electrolyte, thermal and structural stability and reduce the thermal expansion coefficient mismatch, it is usually mixed with YSZ, forming the so called Ni-YSZ composite or cermet (from the mixture of ceramic and metal), which also allows the electrode to be ionically conductive, increase the triple phase boundary length and help stopping the Ni grain coarsening (48). Other oxides having simultaneously ionic and electronic conduction have been investigated, such as: LaCrO_3 , SrTiO_3 and $\text{Sr}_2\text{MgMoO}_6$ based perovskites, although they have some disadvantages, like not sufficient electronic conductivity, the long term stability is questionable and above a critical concentration of dopants the structure can be destabilized (49).

As Ni/YSZ is going to be used in the experiment presented in Chapter 5, more detailed information on how Ni electrodes are made is given in later section.

2.7.2 Oxygen electrode

One of the conditions that oxygen electrode has to meet is to withstand highly oxidizing environments, since is the electrode where oxygen gas is present, either to become oxide ions or vice versa depending on the mode of operation of the cell. Noble metals like platinum and gold can be used, but due to their relatively high cost they are rejected. Instead, other ceramic materials are used. A composite of Lanthanum Strontium Manganite ($\text{La}_{0.8}\text{Sr}_{0.2}\text{MnO}_3$), known as LSM is currently the material of choice used as electrode due to its low level chemical reactivity with YSZ, similar thermal expansion coefficient to YSZ and high oxidizing environment resistance. It is a very good electronic conductor; however, due to its low ionic conductivity the electrochemical reaction region is limited to the TPB, thus, analogous to the Ni-YSZ, LSM is typically mixed with YSZ, usually in a proportion of 50/50%, to form the very well-known composite LSM-YSZ. The addition of YSZ improves thermal expansion coefficient mismatches, increase the TPB length and increase significantly the ionic conductivity. Among other ceramic materials with suitable characteristics for electrode application are: lanthanum cobaltite (LC), strontium-doped lanthanum cobaltite (LSC) and strontium-doped lanthanum ferrite partial substituted (LSCF) (48).

In this work Ni-YSZ and LSM-YSZ materials are used as electrodes (disregarding the dense Pt electrode used in Chapter 5) due to its high acceptance, relatively easy production and very well-known characteristics.

2.8 Electrolyte structure

As briefly discussed in §2.5, YSZ is one of the most common materials used in SOCs applications due to its remarkable properties. However, it is of importance to know the role of dopants to the main structure (in this case ZrO_2). In this section a more thorough description of these structures and the relation to ionic conductivities is given.

2.8.1 Structure of ZrO_2

It is known that ZrO_2 has stable phases at different temperature ranges in atmospheric pressure. Below 1180 °C it exhibits monoclinic structure, above the mentioned temperature and up to 2370 °C it is tetragonal and above that it is cubic, with space groups $P 2_1/C$, $P 4_2/nmc$ and $Fm\bar{3}m$ respectively. The tetragonal-monoclinic and cubic-tetragonal transformations are accompanied by a significant change in volume during cooling from high temperatures due to the change in lattice size, resulting in defective fabrication process of this material (50). Thus, when producing ZrO_2 components, it is necessary to stabilize it into cubic structure by doping with other materials with suitable properties, in our case Yttria and Scandia. Cubic structure of ZrO_2 is known as fluorite type structure. This term comes from the mineral fluorite CaF_2 . The fluorite ZrO_2 structure can be seen as a face centered cubic (fcc) sublattice of Zr^{4+} cations and forming 8 tetrahedra with the cations in the corners, and a cubic sublattice of O^{2-} anions, where the anions are located at the center of the tetrahedral holes of the cation sublattice. A simplified view can be seen in Figure 2.4.

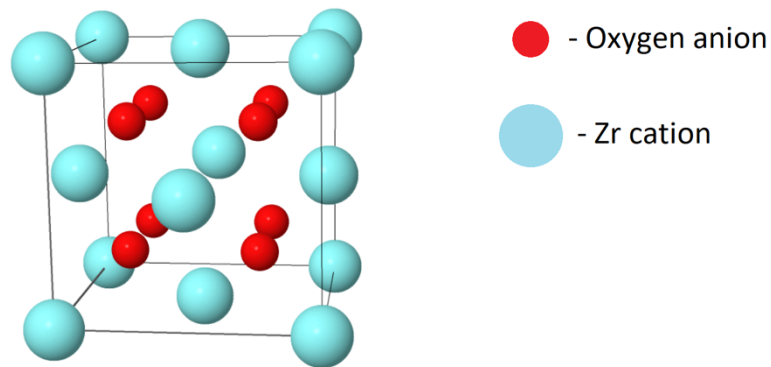
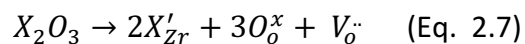


Figure 2.4. Cubic fluorite structure of ZrO_2 . For better visualization, the oxygen anions (red spheres) are smaller than the zirconium cations (cyan spheres), but in reality is in the opposite way.

Due to geometrical considerations, the stability of fluorite structure can be evaluated on the basis of the ionic radii of cations and anions, R^+/R^- (50). The structure is stable if this ratio is larger than 0.732. However, at room temperature and ambient pressure the ionic radii ratio of ZrO_2 is 0.62, in agreement to the known instability of this compound. The condition for stability changes for different temperatures and pressures, but it is not addressed in this work.

When doping ZrO_2 with oxide trivalent cations, like Y^{3+} and Sc^{3+} , the dopant cations substitute some of the Zr cations and to maintain the charge neutrality in the system, one oxygen vacancy is formed for every two dopant cations substituting two Zr cations (51) (52) (53). In general, the defect reaction can be represented by the Kröger-Vink notation as (20) (54):



Where X represents the type of cation dopant.

The structure of YSZ depends on the dopant concentration; for Ytria concentration below 3%mol is monoclinic, in the range between 2 and 6 mol% is tetragonal and is known as partially stabilized zirconia (PSZ), where above 8%mol the structure fully stabilizes into cubic fluorite structure, but for contents of around 8%mol a cubic-like tetragonal phase has been reported in which oxygens are shifted from the ideal positions of the fluorite structure (55). When doping ZrO_2 with Sc in a

concentration of 11%mol (11Sc89Zr), the structure exhibits two phases, rhombohedral and cubic. However, with the substitution of only 1%mol of Sc by Y, which is the Scandia doped electrolyte material used in this work (10Sc1YSZ), the system stabilizes into cubic fluorite single phase, remaining stabilized for higher contents of Y. At lowest dopant concentration of Y (1-2%mol Y) the system exhibits the highest conductivities and best aging properties at high temperatures compared to that of higher content of Y, with very low decrease in conductivity of around 8% after 1500 hours (43).

At room temperature the lattice parameter of 8 mol% YSZ and 10Sc1YSZ are approximately 5.14 Å and 5.09 Å respectively, where at high temperatures the lattice increases according to the thermal expansion coefficient, that for these systems is around $1 \times 10^{-5} \text{ K}^{-1}$ (43) (46) (56) (57).

2.8.2 Ionic conductivity

At typical SOCs operating conditions oxygen vacancies are mobile, thereby providing oxygen ionic conductivity (σ) in the structure via vacancy diffusion mechanism, as oxide ions can hop through vacancies (58). By means of molecular dynamics simulations, this is described as the migration of some anions from one regular site to another with a preferential direction, while the other anions just vibrate around their tetrahedral sites and cations vibrate around their regular sites; this is known as discrete hopping mechanism (59).

In the YSZ material, the ionic conductivity increases for increasing Yttria content up to 8-9 mol%, almost independent in the temperature range 800 - 1200 °C and at higher concentrations of Yttria the ionic conductivity decreases even for increasing oxygen vacancy concentration induced by addition of Yttria (20) (49) (57) (40). Also, at a fixed concentration of dopant the ionic conductivity has a direct dependence with the temperature as the oxygen vacancies are more mobile with increasing temperature due to its lower activation energy at common SOCs operating temperatures (57) (60). Thorough investigation regarding the decrease of ionic conductivity with increasing Yttria content above concentration of 8mol% is given by Yamamura et al. (61) in terms of the number of vacancies and decrease of vacancy mobility; and in Ahamer et al. (57) a very complete expression of the ionic conductivity involving vacancy concentration, mobility, temperature and activation energy is given.

Moreover, the ionic conductivity has also been reported to have a dependence to the cation size, which can be explained in terms of steric blocking effects (62). For example, the ionic radius of Sc^{3+} is similar to the size of cation Zr^{4+} and smaller than Y^{3+} (63). Therefore, the ionic conductivity of Sc_2O_3 doped ZrO_2 (ScSZ) based electrolytes is higher than Y_2O_3 doped ZrO_2 (YSZ) based electrolytes in general, as the larger cation size of Y^{3+} can block more effectively the migration of vacancies than Sc^{3+} cations (43). This is why it is acknowledged that doping with Sc_2O_3 the ionic conductivity of ZrO_2 based electrolyte is improved (40).

It is also known that ionic conductivity depends on the sintering conditions. Different sintering conditions results in different characteristics of the microstructure of the material, like grain size, relative density and intergranular phases (60). In polycrystalline materials, the total ionic conductivity is a contribution from the grain interior (bulk) and the grain boundary conductivities. These contributions can be discern depending on the temperature and by choosing proper electrochemical parameters when performing EIS measurements (43) (57). Also, variation of ionic conductivities have been reported for lamellar structures in thermal-sprayed coating using YSZ, suggesting an anisotropy of ionic conductivity associated to the relative orientation of the structure and the direction of the ionic current (64).

Summarizing what has been stated so far, Table 2.1 shows ionic conductivities of 8YSZ and 10Sc1YSZ in a range of temperatures equivalent to that used in this work, and obtained by different methods.

Electrolyte composition	Method of fabrication	Final material	σ (S/cm) ($\times 10^{-2}$) T = 700 °C	σ (S/cm) ($\times 10^{-2}$) T = 800 °C	σ (S/cm) ($\times 10^{-2}$) T = 900 °C	Reference
8YSZ	Direct melt crystallization in cold container by high frequency heating	Single crystal	1.6	3.2	5.6	Artemov et al (40)
8YSZ	YSZ powder sintered at 1700 °C for 12 hours	Polycrystal Grain size: 18 μm	1.8	4.7	9.6	Ahamer et al. (57)
10Sc1YSZ	Direct melt crystallization in cold container by high frequency heating	Single crystal	4.0	10.0	19.9	Artemov et al (40)
10Sc1YSZ	solid solution grown by directional crystallization of the melt in a cold crucible	Single crystal	4.1	10.3	16.8	Borik et al. (65)
10Sc1YSZ	YSZ powder sintered at 1600 °C for 16 hours	Polycrystal Grain size: 10 μm	2.0	5.1	10	Politova et al. (43)

Table 2.1. Ionic conductivities of electrolyte materials at temperatures 700, 800 and 900 °C, obtained by different methods.

2.8.3 Chemical expansion

Under operating conditions, SOCs can exhibit mechanical stresses from defect induced lattice parameter. For example, under the large oxygen partial pressure gradient cracking of ceria membranes has been reported by Sato et al. (66). This phenomenon is also referred to as chemical expansion or chemically induced expansion (66) (67) (68). The chemical expansion is defined as the change of the dimensions of the material upon a change of the composition and, in general, is believed to be the result from a combined effect of oxygen vacancy formation and cation radii change (67). When creating oxygen vacancies in the structure, the effect can be considered as positively charged particles surrounded by the other cations and anions, thus the positive ions move away from the vacancy while the oxygen anions get attracted, resulting in a net local lattice contraction, as shown in Figure 2.5 in the case of ZrO_2 .

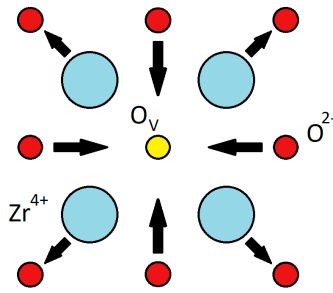


Figure 2.5. Local lattice change around an oxygen ion vacancy (yellow circle). Zr cations (cyan circles) move away from the vacancy while oxygen anions (red circles) move toward the vacancy. Black arrows represent the direction of the movements.

In the case of cation radii change, for example in the reduction from the valence state 4+ to 3+, the ionic radius increases due to the capture of an electron, supported by the Shannon radii data (63), thus resulting in an expansion of the lattice.

The chemical expansion ε is usually described by a chemical expansion coefficient α_c and a factor related to the fractions in terms of valence states of the dopant concentration x , as:

$$\varepsilon = \alpha_c x \quad \text{Eq. 2.8 (67)}$$

From the equation above, the chemical expansion is positive when $\alpha_c > 0$ and chemical expansion is negative for $\alpha_c < 0$. Positive and negative chemical expansion can be interpreted as real expansion and contraction of the lattice respectively. In the work by Marrocchelli et al. (67), the condition at which the chemical expansion coefficient is positive, $\alpha_c > 0$, exists for many dopants in ZrO_2 , and for Y dopant the average α_c is approximately 0.035. However, the only exception where the chemical expansion coefficient is negative, $\alpha_c < 0$, shown in that work occurs when doping ZrO_2 with Sc, where α_c is approximately -0.035. It should be noted that in their work the concentration of Sc is not specified, they only said that the values of dopant concentration of the investigation were up to 25%mol. Some fundamental knowledge of the chemical expansion is going to be used later in Chapter **Error! Reference source not found.** as a support of the observed microstructural changes.

3. Characterization methods in SOCs

In this chapter three main characterization methods for studying the samples in the presented work are described. In our case Scanning Electron Microscopy is used as a *post-mortem* method to assess the degradation and chemical composition at regions of interest of the samples after subjecting to operating conditions, while Electrochemical Impedance Spectroscopy and X-ray diffraction techniques were used to *in-operando* characterize our systems.

3.1 Scanning Electron Microscopy (SEM)

Scanning electron microscopy has been a powerful technique for several decades for materials characterization. It is based on the detection of electrons coming from the sample due to the interaction of its surface with an impinging focused electron beam generated at the tip of an electron source at high voltage in vacuum. The volume of interaction depends on the energy and intensity of the incoming electron beam and on the structural and geometrical characteristics of the sample. The generated electron beam is scanned on the surface of the sample by a set of electromagnetic coils and lenses that deflect and focus the electrons in specific positions on the sample. At each position the sample emits electrons and X-rays and a detector is synchronized to the position of the beam, allowing the reconstruction of an image of the scanned area. If an X-ray detector is placed inside the microscope chamber, then elemental composition analysis is possible, knowing this as Energy Dispersive X-ray Spectroscopy, commonly abbreviated as EDS or EDX (69) (70). It is hard to quantify the abundant literature regarding the studies of materials using this technique, in which solid oxide cells are included. Spatial resolutions of 1 nm or even better are achievable. In common SEM samples are in high vacuum, however in some cases with special configuration of the instrument, low vacuum close to the sample chamber can be used as well. In addition, a wide range of temperatures can also be provided. Nevertheless, performing SEM to solid oxide cells under realistic operando conditions is extremely difficult mainly due to gas

environment. In this work we use SEM/EDS to analyze the topology, perform elemental composition and grain size measurement of cracked and polished cross-section of solid oxide cells.

In the list below are the three types of SEM devices used in this work:

- a. Carl Zeiss SUPRA-35 Gemini FEGSEM
- b. Zeiss Merlin (FEGSEM) + ThermoFisher Noran System 6 EDS detector
- c. Hitachi Tabletop microscope TM3000.

The use of each of these devices are presented in their corresponding chapter.

3.2 Electrochemical Impedance Spectroscopy (EIS)

Electrochemical Impedance Spectroscopy, abbreviated as EIS, is considered one of the most important techniques for characterization of electrochemical systems, like solid oxide cells (20) (71) . When applying an oscillating potential between the electrodes of the cell, the response recorded can provide very useful information regarding the electrochemical processes occurring in the system (72).

The resistance of the system depends on the applied frequency, and in more general way this resistance is known as the impedance. Several processes occur in the electrodes and electrolyte of the electrochemical cell. The behavior of the components and the chemical processes is usually represented by an equivalent circuit model composed by different electrical elements, for example: inductor, resistor and capacitor connected in serial and/or in parallel, in which their values provide determination about the performance / degradation of the system (73) (74). A simple equivalent circuit model is shown in

Figure 3.1:

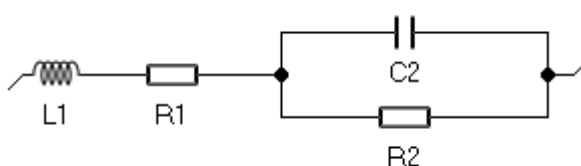


Figure 3.1. Simple equivalent circuit model having an RC circuit connected in series.

The impedances can be usually represented in a Nyquist plot with the imaginary component of the impedance, $-\text{Im}(Z)$ and the real component, $\text{Re}(Z)$ as “Y” and “X” axis respectively. In a typical Nyquist plot the EIS spectrum can follow one or more semicircular shape, depending on the number of RC circuits. In many cases is better to substitute the RC for an RQ circuit in order to improve the quality of the fitting since it offers more flexibility as the shape of the semicircle can now be changed, accordingly to the collected data.

Two basic parameters can be extracted from the Nyquist plot: series resistance R_s and polarization resistance R_p . Series resistance is related to the ohmic contribution from the components of the cell and electrical configuration, including current collectors and cabling. In general, the major contribution to the series resistance is from the electrolyte and depends on the material, thickness and temperature. The polarization resistance is related to the losses (activity) of the electrodes. Thus, the higher the polarization resistance less active is the electrode and vice versa (75).

In order to understand better this, an example of a typical EIS spectrum is illustrated in

Figure 3.2:

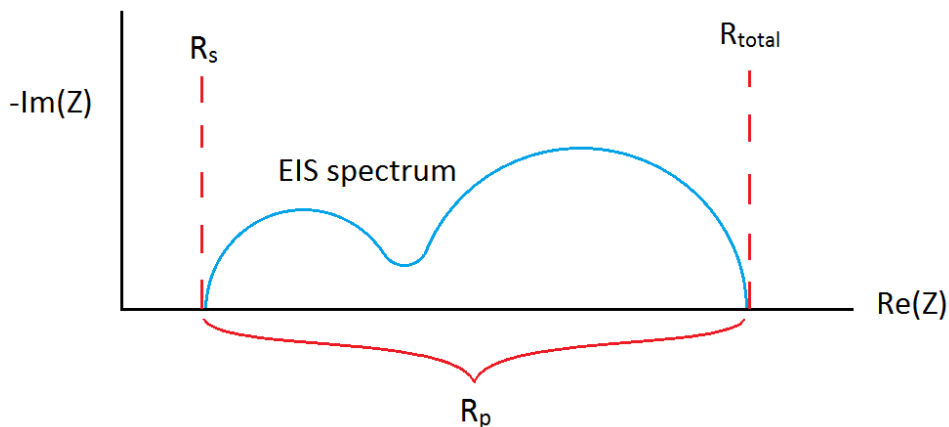


Figure 3.2. Schematic of an EIS spectrum.

In

Figure 3.2, when applying high frequencies the RC circuit acts as an electrical conductor, thus a negligible resistance, so the total resistance of the circuit is given by R1, which is here the so called series resistance R_s , and for low frequencies the capacitor becomes an insulator, the the RC circuit acts like a resistor with resistance R_2 , which is in this case the polarization resistance R_p , then the total resistance of the circuit is the contribution from R1 and R2 or R_s and R_p . The value of R_p can be calculated by subtracting the total resistance from R_s . Therefore, in a Nyquist plot, the R_s can be obtained by the high frequency interception of the EIS spectrum at $-\text{Im}(Z) = 0$ and R_p is then estimated by the difference of the low frequency interception at $-\text{Im}(Z) = 0$ and the R_s .

Moreover, in order to estimate the oxygen partial pressure at the interfaces, we used the well-known equation reported for this kind of systems (8) (76):

$$p_{O_2}^{eff} = p_{O_2}^{air} \cdot \exp\left(\frac{4F\eta}{RT}\right) \quad (\text{Eq. 3.1})$$

Where:

$p_{O_2}^{eff}$ and $p_{O_2}^{air}$ – oxygen partial pressure at the electrode and in air respectively

η - overpotential

T – temperature of the system

R – Universal gas constant

F – Faraday constant

The overpotential is the potential away from the potential at equilibrium and can be obtained by multiplying the current flowing in the system and the R_p . In this work all the electrochemical measurements were carried out using the potentiostat Biologic SP-200 coupled to an ultra-low current module with a current resolution of 760 fA.

3.3 X-ray diffraction

X-ray diffraction is an extensively known non-destructive technique to study the microstructure and properties of materials. It is based on the scattering of X-ray by the electrons of the atoms in

the material structure. Its suitability lies on the fact the X-ray wavelength is typically in the same order of the atomic distances in the structure, which is in the order of Angstroms.

In crystalline materials, the atoms are arranged periodically, so when an electromagnetic wave reaches the structure, the electrons of the atoms scatter the electromagnetic radiation, producing a regular array of spherical waves, that in most of the cases are cancelled out due to destructive interference, but when certain specific condition is fulfilled the interference is constructive, resulting in a high intensity peak (77) (78). This principle is shown in

Figure 3.3:

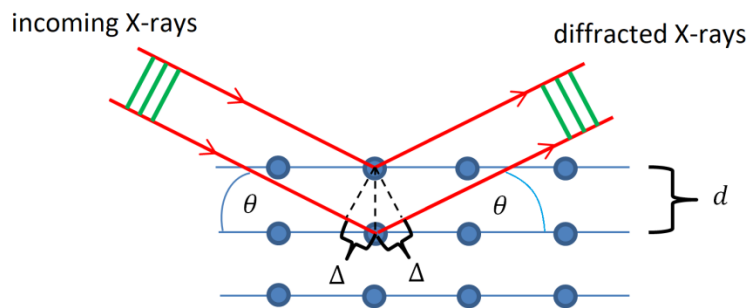


Figure 3.3. Geometrical principle of X-ray diffraction.

The condition at which the interference is constructive is determined by the very well-known Bragg's law that states (77):

$$n\lambda = 2d\sin(\theta) \quad (\text{Eq. 3.2})$$

Where:

λ – wavelength of the electromagnetic wave

d – distance between the atomic planes, also known as interplanar distance or d-spacing.

θ – angle determined by the atomic planes and the incident electromagnetic waves

n – integer number

In X-ray diffraction technique, the incident beam is scanned from low to high angle θ , either by moving the X-ray source or the sample, and the diffracted intensity is collected by an X-ray detector, which also moves respect to the sample to fulfil the Bragg condition. Each crystalline material has its own diffraction pattern, and up to date large databases are used for comparison in order to identify phases. Due to the complexity and variety of the diffraction patterns from hundreds of thousands of known crystalline materials, X-ray diffraction technique is usually complemented by other techniques to improve the reliability of the results.

3.3.1 Mosaicity

In general, crystalline materials are divided in grains/crystals. Grains are not always perfect, containing in many cases dislocations, vacancies and other type of defects that can influence the structural properties of the material (79). Domains without imperfections, considered as perfect crystals inside grains are known as crystallites and because of the presence of defects, planes of crystallites are not oriented in the same direction, but forming mosaic like structures (77), as shown schematically in

Figure 3.4.

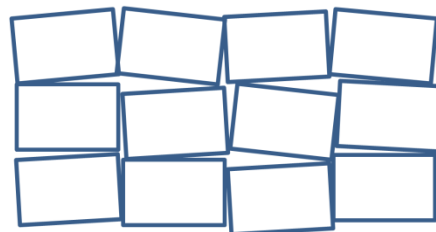


Figure 3.4. Mosaic structure of a grain. Orientation of mosaics is exaggerated here for better visualization.

Thus the term mosaicity is used to describe the spread of crystal plane orientation. Mosaicity can be measured using X-ray diffraction by rocking curves. A full procedure on how to map the mosaicity of a grain is described by S. R. Ahl (80). When tilting the sample with respect to the incoming beam and leaving the detector fixed, subgrain domains fulfil the Bragg condition for

different tilting angles and the intensity profile recorded by the detector follows typically a Gaussian distribution function (81) (82).

3.3.2 Strain

In material science, strain usually refers to the degree of deformation present in the material. The deformation is any change in the shape or size of the object and could be caused by external forces or by thermal change. In general, the strain can be described as a tensor containing axial strain (diagonal elements of the matrix) and shear strain (off-diagonal elements of the matrix) (80). In this work we only treat the axial strain component.

In a simple way, the strain can be quantified by the following equation:

$$\varepsilon = \frac{\Delta L}{L} = \frac{L_{final} - L_{initial}}{L_{initial}} \quad (\text{Eq. 3.3})$$

Where ΔL is the change in length, defined by the difference between the final and initial lengths, L_{final} and $L_{initial}$ respectively.

In the microscopic scale, strain is related to the deformation of the atomic planes for crystalline structures, so the lengths in this case are related to the distance between planes. According to Eq. 3.3 the strain is negative for compression and positive for tension. As the strain is a dimensionless quantity, the relation that involves the strain with real forces involved in the deformation is given by the Young Modulus, which is a coefficient specific for each material and states the amount of real applied force to deform a material. This is known as the stress and the common equation, valid in the elastic range is given by:

$$\sigma = E\varepsilon \quad (\text{Eq. 3.4})$$

Where σ is the applied stress, E is the Young Modulus and ε is the strain (83) (84).

In this work we are going to use the strain and stress of the deformation of the atomic planes of the ScYSZ(111) during operando conditions, averaged in a relatively large distance over the sample and for an individual ScYSZ grain located in the interested region for the experiment in Chapter 4.

In Chapter 5 the strain evolution in Ni and YSZ phases close to the cathode/electrolyte interface is also performed.

3.3.3 Synchrotron radiation

Synchrotron light sources are up to date one of the most powerful tools to investigate all kind of materials that include inorganic, organic and biological matter. Due to its large scale characteristics it produces very intense X-ray beam, with superior properties compared to other facilities and/or instruments, like monochromatic, coherence and extremely small cross-section, achieving nowadays sizes in the order of nanometers. In a simple way, synchrotron radiation is based on the light emission (with wavelength in the order of X-ray) by the rapid deviation from the original direction of fast electrons previously accelerated by other means, moving cyclically inside the storage ring. Several small deviations are commonly produced by a set of small powerful magnets, called undulator and wiggler, resulting in an extremely bright radiation emitted in the direction of the original movement of electrons. In order to optimize the capabilities of generated X-rays, several of these magnets are placed at different positions in the storage ring, and from each position a beamline is built. The optics of each beamline defines the final characteristics of the X-ray beam. In §4.3.1 more detailed information is given regarding the beamline setup used specifically in our experiments.

3.3.4 Dark Field X-ray Microscopy

The advantages of using synchrotron radiation increase enormously the possibilities of implementing new techniques. Here in this work we present Dark Field X-ray Microscopy, a novel non-destructive X-ray diffraction technique for mapping structures, orientation and strain of crystalline elements deeply embedded in materials. A number of works, performed by colleagues at DTU, demonstrating the capabilities of this technique can be found in (29) (30) (28) (80).

Dark Field X-ray Microscopy is analogous to dark field electron microscopy in TEM, in which an image coming from diffraction features of a sample is magnified by means of an objective lens (70). As electrons are more absorbed by the matter than X-ray radiation of equivalent energy,

samples in TEM need to be very thin, usually in the order of nanometers. However, X-ray radiation can penetrate more in the sample, thus allowing obtaining more information from deeper volumetric regions. Therefore, synchrotron radiation provides suitable energies for Dark Field X-ray Microscopy.

In our case, a Dark Field X-ray microscope has been developed in ID06 beamline, at the European Synchrotron Radiation Facility. The final set-up, including classical X-ray diffraction set-up used in our experiments, can be seen in Figure 3.5.

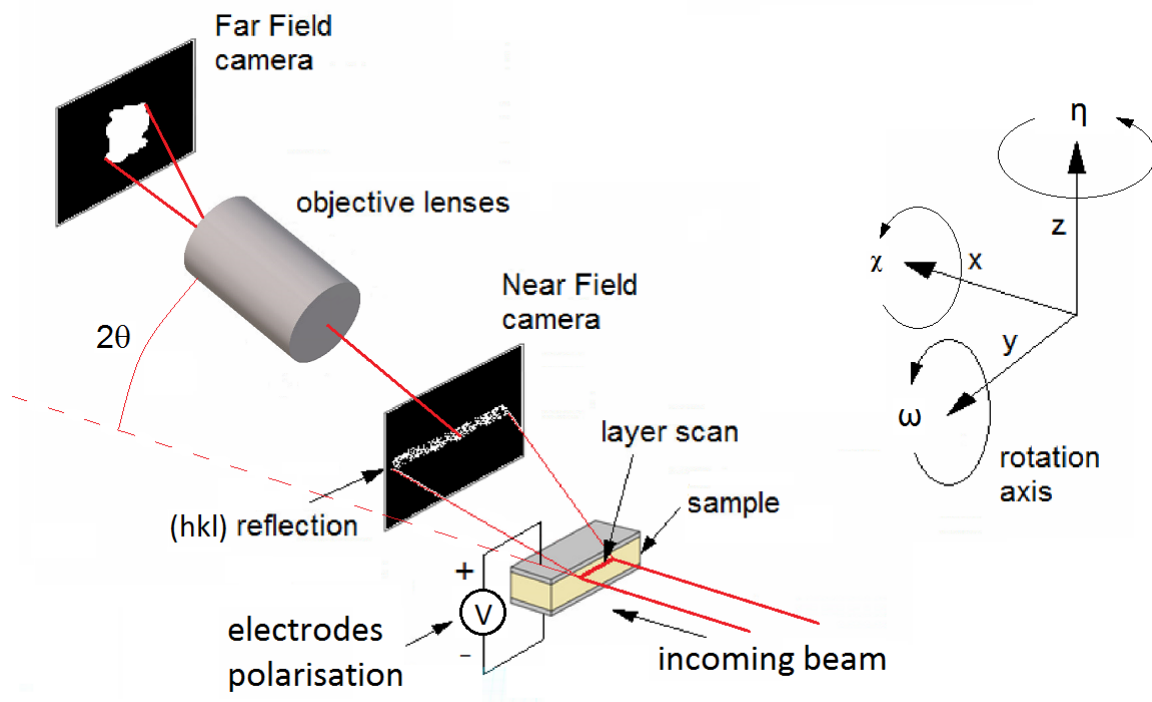


Figure 3.5. Schematic view of the sample setup at beamline ID06 (furnace is not included). The near field camera can be translated out of the diffracted beam enabling dark field microscopy by means of an X-ray objective.

Due to the relatively high energy of X-rays the refractive index for most materials is very close to 1, thus the direction of propagation and beam profile is not significantly affected, mostly for thin thickness as in single X-ray lenses. However, when placing several lenses in serial configuration, commonly known as Compound Refractive Lenses (CRL), the effect cannot be neglected for carefully designed material properties and geometries, thus acting like optical lenses. In our setup,

the objective is a CRL containing 72 Beryllium lenses with a radius of curvature of 50 μm . The objective is aligned on the diffracted beam and its center is placed approximately 350 mm from the sample for the focused position, and the distance sample-to-detector is approximately 5m in horizontal direction (is higher when placing the detector at the required 2θ), giving a total magnification of the image of 16X and theoretical spatial resolution of approximately 110 nm can be achieved (in principle spatial resolution of CRL have been claimed to be in the order of 10 nm, however, the resolution is limited to 100 nm due to by manufacturing processes, associated to optical imperfections and aberrations). A thorough optical description of CRL with application on X-ray microscopes is given in Simon et al. (85)

The principle of this microscope is based on the properties of the objective to generates magnified real space images (inverted) from the diffracted beam of the sample. The objective has a very small numerical aperture NA in the order of 3.5×10^{-4} , as estimated in the supplementary notes by Simon et al. (30) , providing two main advantages:

- very high angular resolution in three dimensions (2θ , χ and ω), where the angular resolutions of 2θ and ω are related to NA and angular resolution of χ is defined by the divergence of the condensed incoming beam (see supplementary notes in (30)).
- acting as an effective filter in reciprocal space, thus removing diffraction signals from other diffracting elements in the sample, thereby avoiding overlap of diffraction spots.

Combining Eq. 3.2 and 3.3:

$$d = d_o(\varepsilon + 1) = \frac{\lambda}{2} \cdot \frac{1}{\sin(2\theta/2)} \quad \text{Eq. 3.5}$$

Where d is the d-spacing of the strained region of the diffracting plane and d_o is the d-spacing for a strain-free condition. The equation above (Eq. 3.6) establishes the relation between the axial strain ε and the 2θ angular position of the diffracting element of the grain/crystal when knowing its spatial position, for a given X-ray energy. This is the basic principle for strain mapping using DFMRM, where the angular resolution plays a key role in the determination of strain.

One limitation of the microscope is that orientation spread of individual structural elements must be known prior to set the limits of angular movements of the sample and objective. This information can be obtained by mapping the structure in a coarse scale or directly from the

structure of interest before performing the final measurement. For example, in our case the YSZ grain, corresponding to mosaicity mapping in Chapter 5 shows a very narrow orientation spread in 2θ , less than 0.06° , while in annealing studies of plastically deformed aluminium was significantly higher, in the order of 3° (30). In addition, depending on the total orientation spread of the analyzed element and the chosen ω angular step, the acquisition time could vary from few minutes to hours in a 2D orientation/strain mapping and even more in 3D mapping (as several layers of 2D mapping has to be scanned through the diffracting element). This may be seen as another limitation in time-resolved studies where structural changes occur in the order of seconds or less. However, with upcoming upgrading of X-ray synchrotron storage ring and optimization of beamline set-up, time resolution is expected to be improved, enabling for *in-situ* and/or *in-operando* studies of even more challenging dynamic processes.

In this work DFXRM is going to be used for strain and mosaicity mapping of single diffracting grain. In order to reduce the time of experiment using the objective, a low resolution Basler camera is placed next to the Far Field detector, as the Basler camera has a larger field of view, making the spot finding much quicker. Specification on high resolution cameras (Far Field and Near Field) are given in further sections.

3.3.5 Thermal expansion

The thermal expansion is the property of materials to change its shape at different temperatures. The majority of existing materials (solid, liquid and gas) expand for increasing temperatures, although there are a few substances that contract in a certain range of temperatures. The rate of change of the shape is quantified by the thermal expansion coefficient (TEC), that can be given in volumetric, area and linear (86). The TEC is a function of temperature and normally does not follow a linear behavior, especially for a wide range of temperatures. For isotropic materials the expansion occurs at the same rate in all directions. In this work we only asses the linear thermal expansion.

The equation to determine the linear TEC is:

$$TEC_{linear} = \frac{L_f - L_o}{L_o} \times \frac{1}{\Delta T} = \frac{\Delta L}{L_o} \times \frac{1}{\Delta T} \quad (\text{Eq. 3.6})$$

Where

TEC_{linear} – linear thermal expansion coefficient

ΔL – difference between final and initial length of the sample (L_f and L_o respectively)

ΔT – difference between final and initial temperature

Since the thermal expansion is dependent on the nature of atomic structure arrangements (87), X-ray diffraction has been used to determine TEC by the change of lattice parameters (86) (88). In this experiment we make use of the capabilities of DFXRM to estimate the linear TEC of a diffracting ScYSZ grain from room temperature to the final temperature used in experiments presented in Chapter **Error! Reference source not found.**

4. Evolution of void formation on ScYSZ grain boundaries in symmetrical LSM/YSZ – ScYSZ cells

This chapter is based on the manuscript: “In-operando observation of microstructural evolution in a solid oxide cell electrolyte operating at high polarization” with authors: J. X. Sierra, H. F. Poulsen, P. S. Jørgensen, C. Detlefs, P. Cook, H. Simons, A. C. Jakobsen, J. R. Bowen. The manuscript has been accepted for publication in Journal of Power Sources and it is also attached in the Appendix at the end of this work.

4.1 Introduction to the chapter

The mechanism of void formation in electrolyte grain boundaries has not been deeply studied yet because of the difficulties dictated by harsh working conditions, configuration of the system and nanometric size of the pores. Hence, this represents a motivation in our research and a step forward on elucidate the conditions and electrolyte structural changes, believed to be related to void formation.

The study presented in this chapter have been carried out by using typical characterization techniques involving, in general, electron microscopy, electrochemical impedance and X-rays. A novel method to build the samples has been developed in order to meet the limitations of the experimental setup. Several experiments have been performed in-house in order to statistically assess information regarding the conditions and factors influencing the formation of voids. For this, *post-mortem* SEM was employed to explore the morphology of the electrolyte. Furthermore, EIS was performed as a complementary technique to analyze electrochemical parameters related to the performance/degradation of the system. In general, the cells were tested in a range of temperatures between 700 and 900 °C in air at a polarization of 2V during up to 72 hours.

Moreover, a cell with identical composition and similar geometry is tested *in-operando* by synchrotron X-ray in diffraction mode, aiming for the changes of structural parameters under

700 °C in air at 2V. As a part of the *in-operando* experiment, DFXRM is performed to a diffracting grain for strain mapping, showing the capabilities of this novel technique. *Post-mortem* SEM is performed to complement the results of the *in-operando* experiment.

Specific details concerning the sample materials, characteristics of the experiments and setup are given in further sections, along with the corresponding results and discussion.

4.2 Materials and sample preparation

The choice of materials and cell geometry was based on a balance between simplicity, easy to obtain, very well-known properties for SOC purposes and more importantly on the limitations of the beamline configuration where the *in-operando* experiments were carried out.

For the simplicity in our experiments, a symmetric cell configuration was selected. This is also in good agreement to the limitation that no dual atmosphere is going to be used, therefore there is no necessity to use different materials as electrodes as in realistic SOCs.

4.2.1 Electrolyte material

The material of the electrolyte is a mixture of 10mol% of Sc₂O₃ and 1mol% of Y₂O₃ in a Zirconia structure, that in this case is represented as (Y₂O₃)_{0.01}(Sc₂O₃)_{0.10}(ZrO₂)_{0.89}, which is also commonly known as 10Sc1YSZ. Since no other type of Sc₂O₃ and Y₂O₃ doped Zirconia based material is used as electrolyte in the work presented in this chapter, from now on we denote it as ScYSZ. The ScYSZ powder was provided by Daiichi Kigenso Kagaku Kogyo Co., LTD. The electrolyte was prepared by tape casting by Risø lab technicians and sintered with the following thermal program: from room temperature (RT) to 600 °C at 30 °C/hour for 10 hours, then from 600 °C to 1450 °C at 100 °C/hour for 8 hours and finally from this temperature to RT at 100 °C/hour, with a final sheet thickness of approximately 180 μm. To explore the effects of grain size in the void formation, two grain size based electrolyte were examined; one with the grain size obtained by the sintering method described above (pristine sample) and the other with a larger grain size. To increase the grain size, a portion extracted from the ScYSZ sheet was subjected to a thermal treatment, that consisted of heating from RT to 1600 °C at 300 °C/hour for 1 hour and a cooling rate of 60 °C/hour to RT.

Moreover, a larger grain size is also desired in order to improve the study when performing the *in-operando* experiment with X-rays, especially the X-ray microscopy on a single grain, as seen later in this chapter.

To estimate the grain size, portions with dimension of approximately $2 \times 2 \text{ mm}^2$ of the corresponding sheets were taken for the thermal etching method. In this case thermal etching consists of polishing the sample with $1 \text{ }\mu\text{m}$ grain, followed by a thermal treatment at $1400 \text{ }^\circ\text{C}$ with a ramp up speed of $300 \text{ }^\circ\text{C}/\text{hour}$ for 12 minutes and a cooling rate of $60 \text{ }^\circ\text{C}/\text{hour}$ to RT, similarly as used by (89) for 8YSZ. After applying the thermal treatment, the grain boundaries become easier to outline under SEM micrograph due to the formation of grooves at the intersections of ScYSZ grain boundaries with the already polished surface at high temperature in which the grooves remain after cooling to RT. The samples selected for grain size estimation were then cleaned in high purity acetone to remove any kind of residues/debris on the surface from the furnace and manipulation after collecting.

The grain size was estimated by the linear intercept method from 5 images of each kind of sample, taking into consideration a correction factor accounting for the intercepts of the plane and of the test line with respect to the grains (90) (91). The average intercept lengths were multiplied by the factor 1.56 given in Mendelson (90) for polycrystalline ceramics undergoing normal grain growth. The effectiveness of the thermal treatment and the distribution of the pristine and thermally treated electrolytes are shown later in the results.

4.2.2 Electrode material

As electrode material, 50/50% slurry of LSM-YSZ was sprayed on both sides of each sheet, thereby forming the symmetrical cell. The cells were then sintered from RT to $600 \text{ }^\circ\text{C}$ for 4 hours with a speed rate of $15 \text{ }^\circ\text{C}/\text{hour}$ and from $600 \text{ }^\circ\text{C}$ to $1300 \text{ }^\circ\text{C}$ for 6 hours at $60 \text{ }^\circ\text{C}/\text{hour}$, with a cooling rate of $60 \text{ }^\circ\text{C}/\text{hour}$, achieving an electrode thickness in the order of $5\text{-}10 \text{ }\mu\text{m}$. Sintering temperatures above $1300 \text{ }^\circ\text{C}$ are not applied because it can cause the formation of unwanted phases, like $\text{La}_2\text{Zr}_2\text{O}_7$ and SrZrO_3 , as they can be electronically insulating, thereby reducing the electronic conductivity of the electrodes (92) (93).

4.2.3 Cell components and assembly

The cells were sandwiched between protective alumina plates and rectangular pieces with dimensions specified in next sections were carefully cut using a diamond blade wheel (Minitom, Struers A/S). To ensure electronic conductivity, platinum cables with a 2 mm flattened tip were bonded to the electrodes with platinum paste. When putting the flattened Pt cable with Pt paste on the electrode surfaces, a small object with sharp end was placed on the Pt cable for a few minutes to avoid detachment while drying in air. To hold all components together an Aron Ceramic, class D inorganic adhesive paste was used and cure at 150 °C in air, as the manual recommends. This ceramic paste performs very well as an electrical insulator and has good structural stability at SOC's operating temperature. Approximately half of the cell was left exposed to the furnace air atmosphere as the most active part. The assembly of the cell is shown in Figure 4.1. The other side of the cell was assembled by the same method as described above in this paragraph.

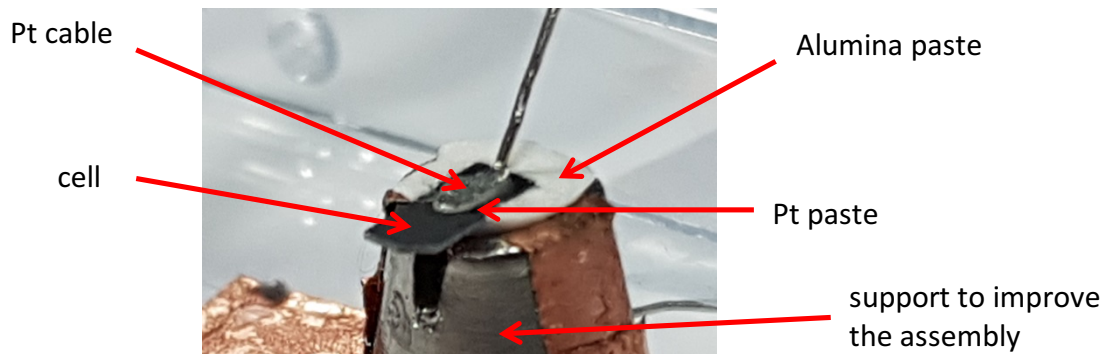


Figure 4.1. Cell assembly and parts for the void statistics experiments.

Two types of experiments were performed:

- 1) Void statistic experiment, where cells were tested off line for a specific duration and condition after which their internal structure was examined.
- 2) *In-operando* experiment, where the structure of grains was probed over time by X-ray diffraction.

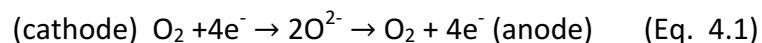
A similar sample setup was utilized for both types of experiments primarily dictated by the constraints of the synchrotron experiment, i.e. small cell size in the beam direction to avoid X-ray absorption, large grain size suitable for incoming condensed beam, atmospheric air gas environment and high polarization to induce degradation, like void formation to be detectable within the beamtime duration.

In the following sections §4.3 and §4.4 a complete description of the cell assembly and the methodology used for each kind of experiment is given.

4.3 Void statistic experiments

Samples with dimensions in the order of $1.6 \times 5 \text{ mm}^2$ were tested in atmospheric air at 700, 800, and 900 °C. A fixed potential of 2V was applied for durations of 6 to 48 hours and 6 to 72 hours for thermally treated and non-thermally treated ScYSZ electrolytes based cells respectively. The experiments were carried out in an alumina tube furnace and the cells were placed at a maximum distance of 15 mm from the thermocouple to ensure a realistic temperature measurement. During these experiments, bunch of four cells were simultaneously put into the furnace at high temperature and polarization was applied one at a time, after finishing the desired testing time with the previous cell. The cells were then fractured *post-mortem* as close as possible to the interface of the active region and the ceramic paste to perform electron microscopy.

According to this configuration, the cell acts as an electrochemical oxygen pump. Oxygen reduction occurs at the cathode/electrolyte interface and the oxide ions created by the reduction conduct through the electrolyte, driven by the potential difference at the electrodes, reaching the anode where they are oxidized and released as oxygen molecules (94) (22). The overall equation is given by:



4.3.1 Electron microscopy

To analyze the morphology of the *post-mortem* fractured cells after been subjected to operating conditions, a Carl Zeiss SUPRA-35 Gemini FEGSEM scanning electron microscope was used. A secondary electron detector SE2 (Everhart-Thornley) was used with an accelerating voltage of 2kV. The relatively low voltage of the microscope allows for better image quality with no carbon coated surfaces of cells, avoiding charging of surface that may result in distorted and blurred images.

4.3.2 EDS analysis

To examine the elemental composition and gradients across the electrolyte after operation, a highly degraded cell was selected for EDS. The side not used for *post-mortem* analysis of the fractured cell was embedded in epoxy, polished and carbon coated in order to prevent charge effects when performing SEM/EDS. To perform the carbon coating a BAL-TEC CEA 035 Carbon Evaporation Supply coupled to a BAL-TEC SCD Sputter Coater was used. According to the distance sample-thread using a single carbon thread, it gives a carbon layer thickness of approximately between 5 and 10 nm. Polished cross-sections were imaged at 2kV and EDS analysis was carried out using a ThermoFisher Noran System 6 EDS detector with an electron beam set at 29 kV in order to avoid Zr and Y *k*-alpha peak overlap.

4.3.3 EIS analysis

In the electrochemical study three cells with a grain size of 6 μm fabricated from the same group described in §4.2, was used. Since the EIS experiments and void statistics experiments were carried out separately, it should be noted that the samples at equivalent operating conditions in both experiments are not the same, although they are morphologically and structurally identical as they come from the same group of samples. Therefore, the results given by these experiments should be consistent to each other.

The electrochemical measurements were performed using the potentiostat described in §3.2 and a constant polarization of 2V was applied during approximately 120 hours. The high frequency was set to 1MHz and the low frequency was chosen in every case depending on the noise and the intercept at $\text{Im}(Z) = 0$. The number of frequency per decade and average points per measurement

were set such that the total time to acquire an impedance spectrum is between 15 and 30 minutes, which can be considered as suitable for monitoring the evolution of electrochemical parameters of the cells.

R_s was estimated from the interception point of a linear fitting from the closest frequencies to $-\text{Im}(Z) = 0$, and R_t was estimated by the following two methods:

- 1 - averaging $\text{Re}(Z)$ values in the vicinities of $\text{Im}(Z)=0$ in the cases with relatively low noise at the right side of the spectrum.
- 2 - fitting using EC-Lab software tool in cases with relatively higher noise and when the low frequencies do not reach the vicinities of $-\text{Im}(Z)=0$.

The EIS profile was fit to two semicircles, considering the equivalent circuit as shown in Figure 4.2:

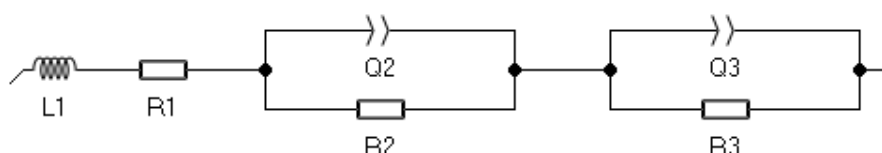


Figure 4.2. Equivalent circuit model used to fit the EIS profiles.

As this is a symmetrical cell, the overpotential of each electrode was estimated by dividing by 2 the R_p , as recommended by C. Chatzichristodoulou (private communication, March 2018: Senior Researcher at DTU, Department of Energy Conversion and Storage). This is not a rigorous estimation, as theoretically the R_p at each electrode should be different according to the reactions occurring at each interface. This is a limitation of the experiment; therefore, it is recommended to find alternatives to determine the overpotential more accurately.

4.4 *In-operando* experiment

The experimental geometry used to carry out the *in-operando* experiment is sketched in Figure 3.5. The *in-operando* cell was made using the same procedure as described in §4.2 but with dimension 0.33x4x0.18 mm in directions “x”, “y” and “z” respectively, with reference to the

coordinate system shown in Figure 3.5. The dimensions in the plane “xy” and components of the cell are shown in Figure 4.3.

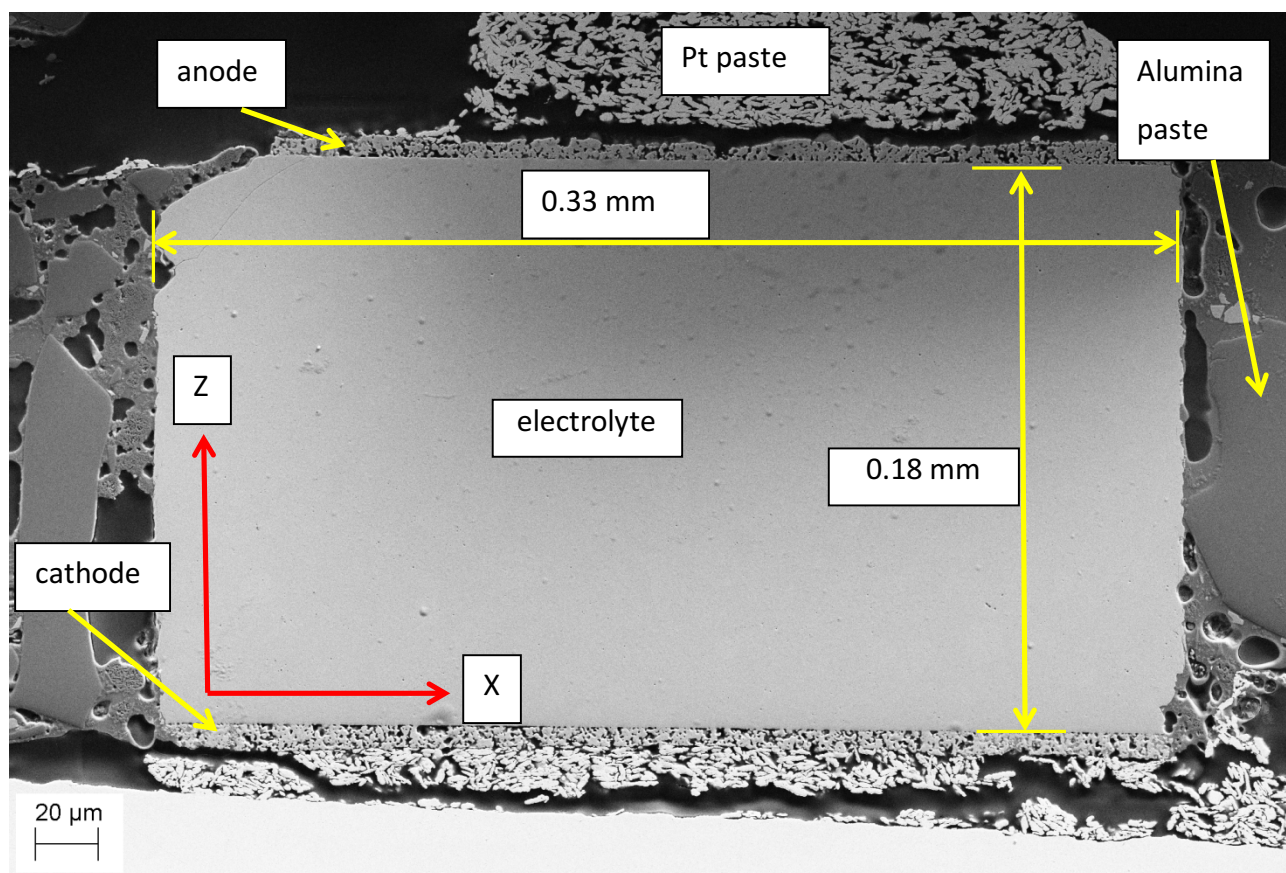


Figure 4.3. *Post-mortem* SEM image from a polished cross-section of the cell selected for the *in-operando* experiment. Directions “x” and “z” as in beamline setup are indicated by red arrows. Vertical and horizontal dimensions are indicated by text boxes of the corresponding yellow lines delimiting the electrolyte. Yellow arrows attached to text boxes indicate the parts of the cell and cell support.

The experiment took place at the European Synchrotron Radiation Facility (ESRF) beamline ID06 using 17 keV X-rays. The cross-section of the incident beam was defined by a silicon condenser – a CRL – with a resulting FWHM of 350x17 μm in “y” and “z” directions respectively. The sample was annealed *in-operando* at 700 °C for a total of 32 hours. It was scanned repeatedly with respect to the beam in the “z” direction in 51 steps covering a range of 0.25 mm, which is more than the size

of the cell to ensure comprising information from both electrodes and electrolyte. The top and bottom of the cell were identified from the absence of the diffracted signal outside the sample.

The goniometer allows rotations around both the y- and z-axis. The diffraction signal from ScYSZ (111) was studied using alternately a near field camera and the dark field microscope using a far field camera.

The near field set-up involves a FreLoN camera coupled to a scintillator screen, with a resulting effective pixel size of $0.622\ \mu\text{m}$, giving an image resolution of 2048×2048 pixels. Placed at a distance of 50 mm from the sample in “x”, a segment of the (111) Debye-Scherrer ring is observed. An example of a raw image can be seen in Figure 4.4. The grains in the illuminated volume give rise to distinct diffraction spots. These are sampled while performing a continuous scan in ω , with a range of 4° in steps of 0.01° . From the center-of-mass position of the spots on the detector we can derive statistics of grain average properties, in particular grain volume, and the average axial strain within a grain (95).

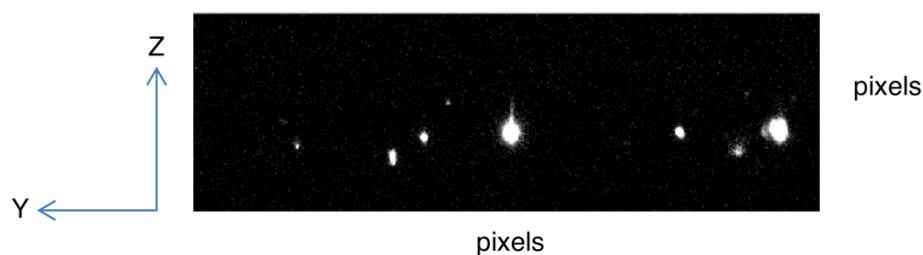


Figure 4.4. Near field image showing (111) diffraction spots from ScYSZ grains at a specific layer and angle ω , with background subtracted. The image resolution is 512×160 pixels in “y” and “z” respectively.

The near field data were analyzed using the program: “peaksearch” in Fable (96). A background image was created by the median of 10 images containing the peaks and subtracted from all images to obtain a cleaner image with the contribution only of real peaks. The filtering rejected peaks with less than 5 pixels, saturated pixels, and peaks associated with low integrated intensity and a mosaicity lower than twice of the ω step, in order to remove noise and uncertainties in the

center of mass position in the images. The average d-spacing of the (111) was estimated by the positions of the filtered peaks in the “z” direction of the near field images at all “ ω ” of each layer.

The objective lens of the DFXRM was positioned at 2θ angle of the same diffraction line. This set-up allows mapping of the structure and strain within selected grains. The far field detector is a FreLoN camera coupled to a scintillator screen, with a resulting effective pixel size of $1.4\ \mu\text{m}$ and 2048×2048 pixels of resolution. In order to improve the signal-to-noise ratio the images of the far field detector were binned to 4×4 , giving a final spatial resolution of approximately $300\ \text{nm}$ (97). By scanning the scattering angle 2θ the local axial strain component is probed (97). To integrate over the rocking curve during acquisition for strain mapping the sample was continuously rotated over a ± 0.05 range in ω . The data analysis followed the procedure presented by Ahl et al. (28).

Hot air gas blower from the ESRF lab, with a nominal maximum temperature of $1000\ ^\circ\text{C}$ was used. The temperature was raised from RT to the maximum in approximately 5 hours. Relatively slow ramp up of temperature was chosen to avoid cracking of the cell components due to thermal expansion mismatch. Due to the limitations of the furnace-detector geometry, the sample was placed a few millimeters away from the hottest part of the furnace, to allow detection of the (111) diffraction line, as shown in Figure 4.5.

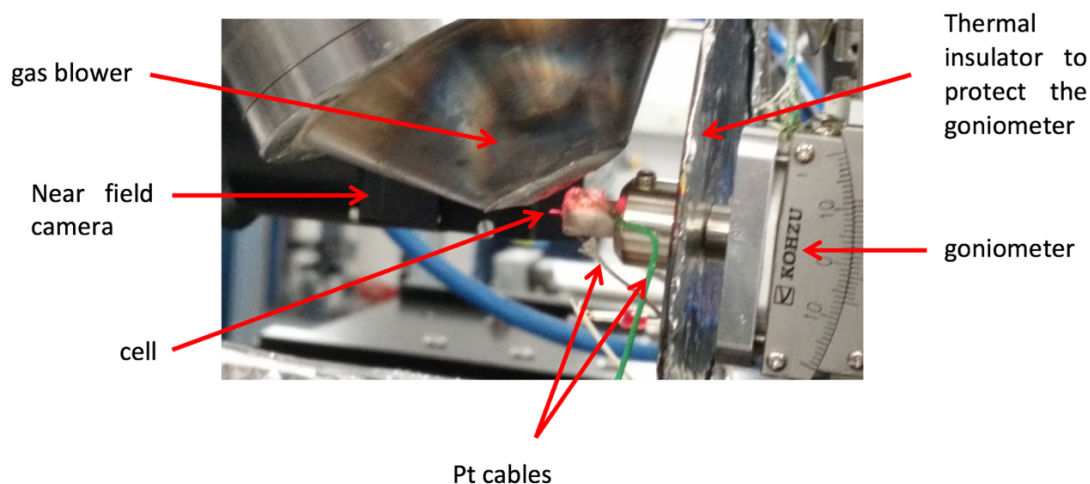


Figure 4.5. Setup close to the *in-operando* cell. In this image the cell is glowing due to the high temperature provided by the gas blower. Near field camera can be seen behind the gas blower, although it is off the working position.

With this geometry, the temperature of the sample was 700 °C, estimated by a thermocouple placed approximately 2 mm away from the sample. The calibration of the temperature was done as follows: first the thermocouple was placed in analogous position of the cell by using the same sample holder, the second step was to move the thermocouple 2 mm away to allow measuring the temperature difference, and then the *in-operando* experiment temperature was estimated considering that difference previously measured with the thermocouple at 2 mm from the cell.

After reaching the desired temperature the voltage was set at 2.0V, provided by a power source from ESRF. The time of the last layer scan performed was 24.7 h after applying the voltage and the total exposure time at operating conditions was 32 hours. Collection of diffraction data after the 24.7 h measurement was not experimentally possible due to random failure of the acquisition system.

At high temperature, five stages were defined as follows, excluding the room temperature stage as the starting point of the experiment:

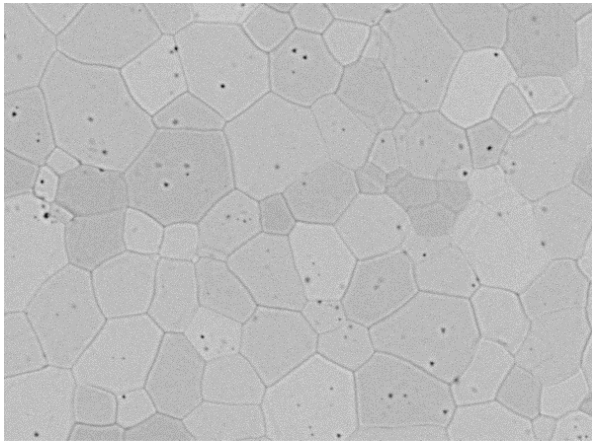
- 0V: no applied voltage
- 0h@V: applied voltage of 2V at initial time
- 2.4h@V: applied voltage of 2V for 2.4 hours
- 17h@V: applied voltage of 2V for 17 hours
- 24.7h@V: applied voltage of 2V for 24.7 hours

4.5 Results

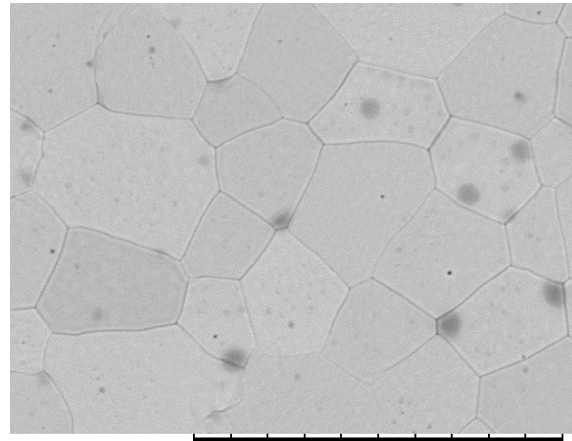
The results presented in the following sections correspond to the two main experiments described above. The first sections, from §4.5.2 to §4.5.5 describe the results related to the void statistics experiments, including the EIS testing, while sections from §4.5.7 to §4.5.10 correspond to the results of the *in-operando* experiment done with X-rays.

4.5.1 Grain size of electrolyte

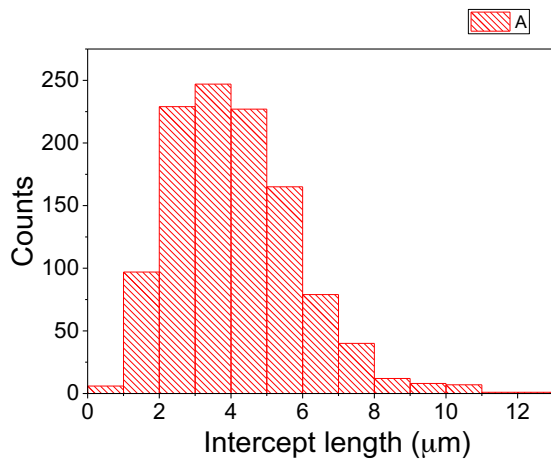
The images in Figure 4.6, show the effectiveness of the thermal treatment applied to grown the grains, with the corresponding length intercept distribution for the pristine and thermally treated electrolytes.



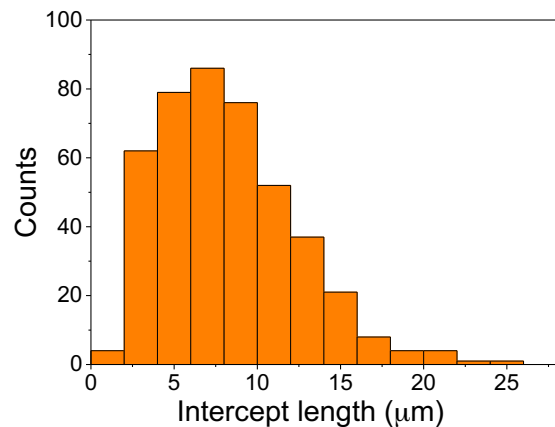
a)



b)



c)



d)

Figure 4.6. SEM micrographs of thermally etched ScYSZ surface. a) Non-thermally treated and b) thermally treated at 1600 °C for 1 hour. Note the easy visualization of the grain boundaries. Images in c) and d) are the distributions of the intercept lengths measured between grain boundaries for the non-thermally treated and thermally treated at 1600 °C sheet respectively.

The average grain size of the pristine and thermally treated ScYSZ electrolytes are 6.3 ± 1.8 and 12.8 ± 4.1 μm (± 1 standard deviation) respectively. For simplicity, cells based on these electrolytes are then referred to as $6\mu\text{m-ScYSZ}$ and $13\mu\text{m-ScYSZ}$ respectively and the *in-operando* cell described in §4.4 will be designated as $13\mu\text{m-ScYSZ-op}$.

4.5.2 Characteristics of void formation close to the anode/electrolyte interface

Two representative examples of void formation on cleaved grain boundaries are shown in Figure 4.7 for the 13 and 6 μm grain size electrolytes ($13\mu\text{m-ScYSZ}$ and $6\mu\text{m-ScYSZ}$ respectively). The structures have a similar appearance as to those reported in the literature, where the voids size are from a few nanometers to approximately 100 nm (8) (9) (10). Furthermore, no void formation was found in any of the cathode/electrolyte interfaces of the samples subjected to a polarization of 2V.

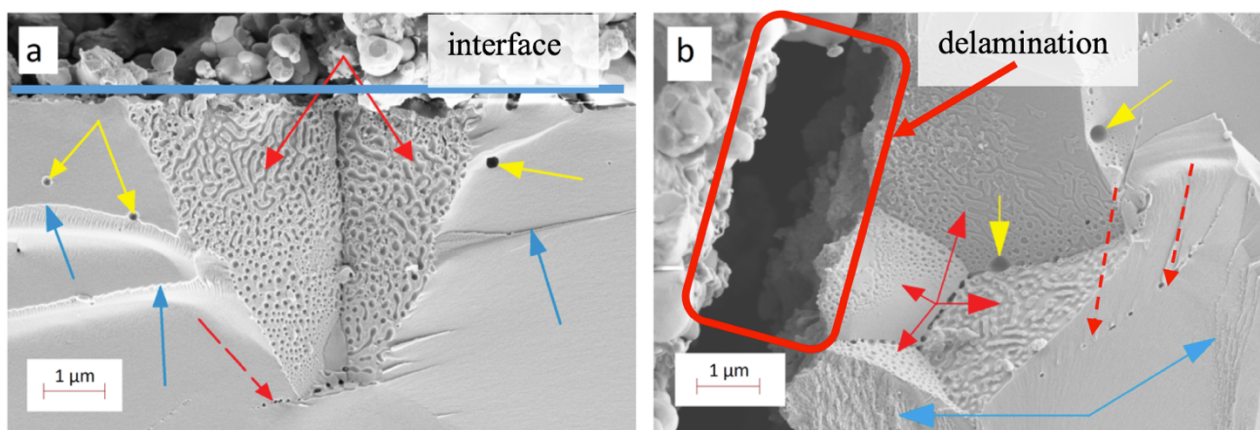


Figure 4.7. Examples of void formation indicated by red arrows, mainly in the grain boundaries of a) $13\mu\text{m-ScYSZ}$ at 900 °C for 12 hours and b) $6\mu\text{m-ScYSZ}$ at 900 °C for 72 hours. The anode/electrolyte interface in a) is indicated by the horizontal blue line and a delamination of the anode can be observed in b) indicated by the red box. Blue arrows indicate intra-grain structures when fracturing the sample, yellow arrows indicate intrinsic pinholes and dashed red arrows indicate void formation that could possibly be on a plane non-parallel to the fractured surface.

Regions pointed out by blue arrows in Figure 4.7 indicate surfaces where the fracture surface passes through grain interiors (intra-grain fracture) during the sample preparation. These fracture

surfaces contain features typical of fracture in low toughness materials. No extended surface areas of void formation were found in these regions, only lines of voids (dashed red arrows) were observed. These, “pearl-on-a-string” voids decorate grain boundaries oriented approximately orthogonal to the SEM images and represent a cross-section of the void patterns indicated by the red arrows on cleaved grain boundaries. Extensive void formation indicated by the red arrows corresponds to regions where the fracture path has followed grain boundaries weakened by void formation. Yellow arrows correspond to pre-existing pinholes and are identified by different characteristics compared to void clusters. For example, pinholes were observed randomly inside grains and on grain boundaries, their size, in many cases is significantly larger than the observed voids and are more isolated in a similar manner to untested material.

For comparison, a sample subjected to 850 °C for 72 hours with no potential difference between electrodes was taken as a reference, showing no void formation. The image can be seen in the Figure S3 of the supplementary material of the manuscript submitted for publication, attached at the end of this work.

Void formation was also observed adjacent to edges of pinholes and at intragranular cracks, as observed in Figure 4.8. These observations of voids close to pinholes, cracks and in the majority of the cases on grain boundaries may suggest that these defects can act as nucleation sites for voids to be formed.

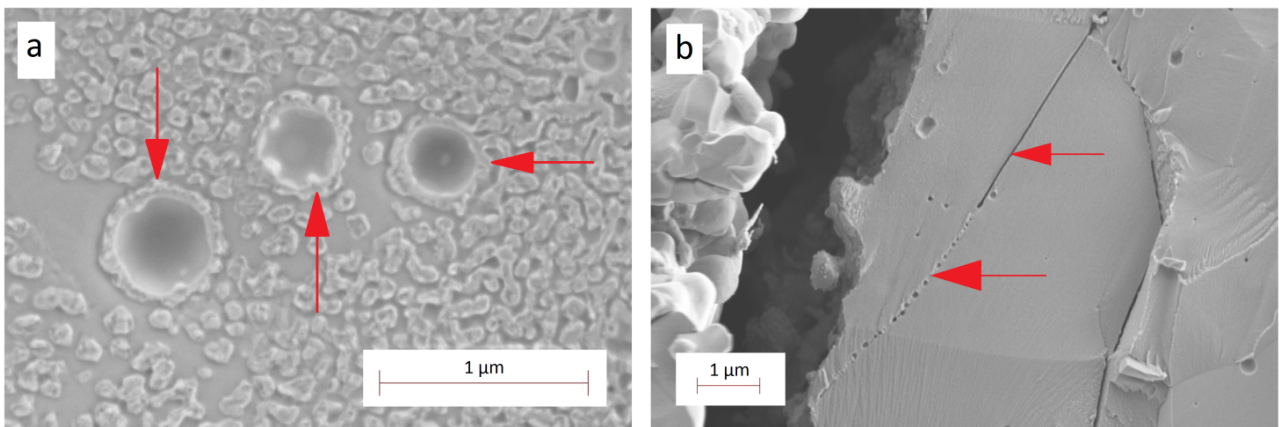


Figure 4.8. Void formation found in 6µm-ScYSZ at 900 °C for 72 hours a) surrounding intrinsic pinholes and b) continuing a crack in the electrolyte material, indicated by the red arrows.

Also in typical surveyed images, with a width of 20.5 μm in the direction parallel to the scanned surface along the interface and a pixel size in the order of 10 nm, the smallest individual voids that can be distinguished are estimated to be between 20-30 nm, as shown in Figure 4.9. However, occurrences of voids were only quantified when observed as an agglomeration of voids. Isolated voids were not considered as significant.

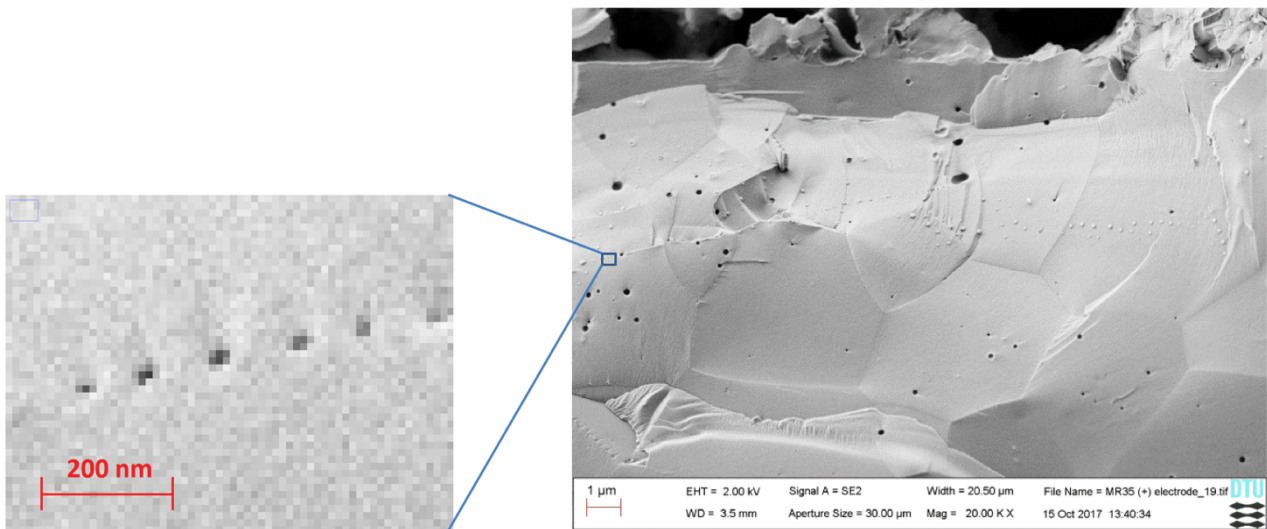


Figure 4.9. Limits of void detection. Estimation by visual inspection of the limits of void detection, using a typical image with 20.5 μm width and a pixel size of 10 nm. Individual voids can be seen as dark spots of minimum 2-3 pixels and forming clusters in the grain boundaries.

4.5.3 EDS to a highly degraded cell

The cell 6 μm -ScYSZ @900 $^{\circ}\text{C}$ x 72 hours was chosen for EDS due to its higher degradation exhibited in comparison to the other cells. The region scanned during EDS measurement is shown in Figure 4.10, with a line width of approximately 140 μm .

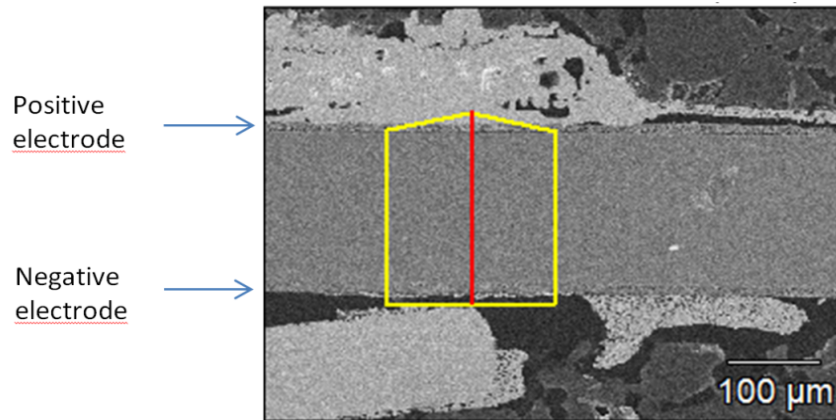


Figure 4.10. EDS performed to the cell 6 μm -ScYSZ @900 °C x 72 hours. Red vertical line shows the direction of EDS and yellow polygon delimits the entire region to integrate detected counts.

The elemental composition is shown in Figure 4.11:

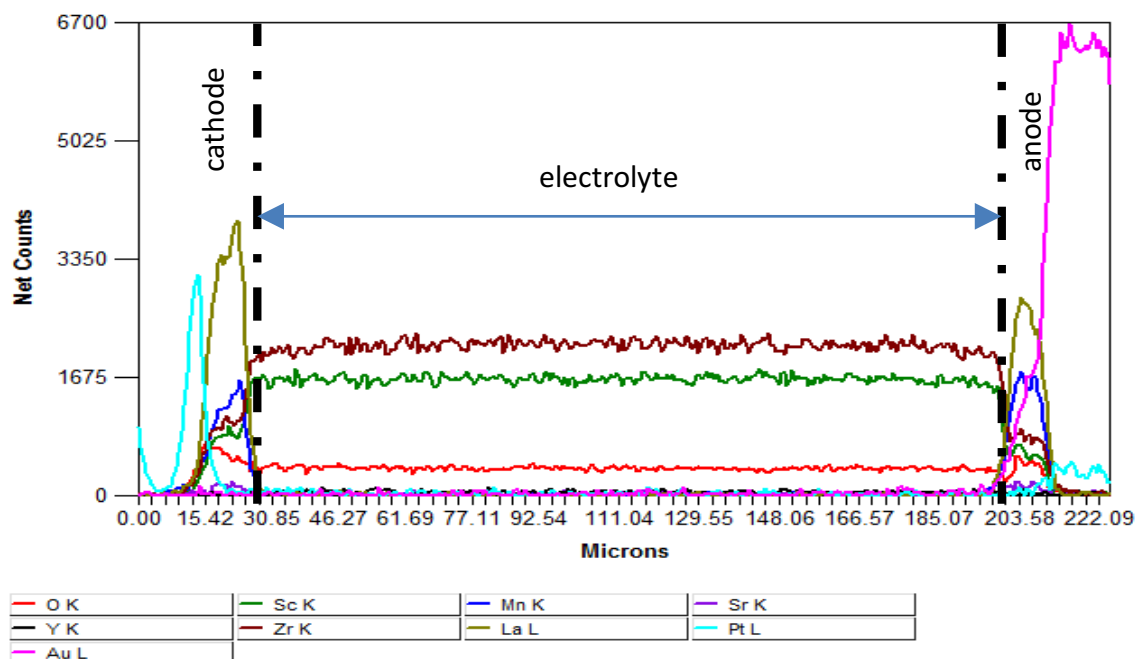


Figure 4.11. Elemental composition of the EDS region of cell 6 μm -ScYSZ @900 °C x 72 hours. Vertical axis represent the net counts integrated along the horizontal direction, perpendicular to the red line shown in Figure 4.10. The left and right side of the EDS correspond to the cathode and anode respectively. The vertical dashed-dot black lines indicate the limits within the electrolyte region.

From Figure 4.11 it can be seen that the regions at the top and bottom (see Figure 4.10) have gold and platinum. Those elements belong to gold (Au) and platinum (Pt) cables used in this cell as the interconnectors, besides the Pt paste applied to enhance the electronic conductivity between the electrodes and the interconnectors. It is worth noting that only in the case of this sample, Au cable was used as the interconnector at the anode, due to decisions with supervisors in early experiments, based on distinguishing the electrodes in SEM. This may suggest that by using two different cable compositions can induce a potential difference to the cell over the already polarization applied, similarly as in thermocouples. However, the length of these two cables are approximately 20 mm, hence remaining in the region inside the tube furnace where the gradient of temperature between the end of the cables can be considered negligible. Therefore, it is valid to assume here that the results of the experiment should not be different as expected if only Pt cables were used. However, due to the more availability of Pt cable at that moment and overcoming the former issue (of differentiating the electrodes) by monitoring the polarity of electrodes during the fracturing process of the cells, only Pt cables were used in the subsequent experiments.

Moreover, the concentration of elements presents in the electrolyte; Sc, Y, Zr and O are practically constant within the limits of the electrolyte region, indicating that no significant change in terms of elemental composition gradient occurred after subjecting the sample at the mentioned operating conditions during 72 hours. The profile of Y is overlapped by the other elements not present in the electrolyte (Pt, Au, La, Sr and Mn) due to its very low concentration in comparison to Zr, Sc and O.

4.5.4 Statistics of void formation

The results of the void statistics experiments are shown in Figure 4.12. In the upper row of the figure; a) and b) the vertical axis, denoted as “Ratio of images”, represent the ratio of images containing void formation to the total number of images along the interface of the cell. During the SEM survey the images without voids were not recorded, therefore the total number of images is then estimated by the width of the cell and the width of the used images; 20.5 μm .

Moreover, as an alternative to extract more information related to the void formation statistics, the depth at which the voids were observed below the anode/electrolyte interface, was monitored. Bottom row in Figure 4.12, c) and d) shows the relation between the maximum depth of observed void formation for each cell, vertical axis, at different test durations and temperatures.

As a clarification, graphics in a) and c) correspond to the case of the cell with small grain size electrolyte, while b) and d) correspond to the cell with big grain size electrolyte.

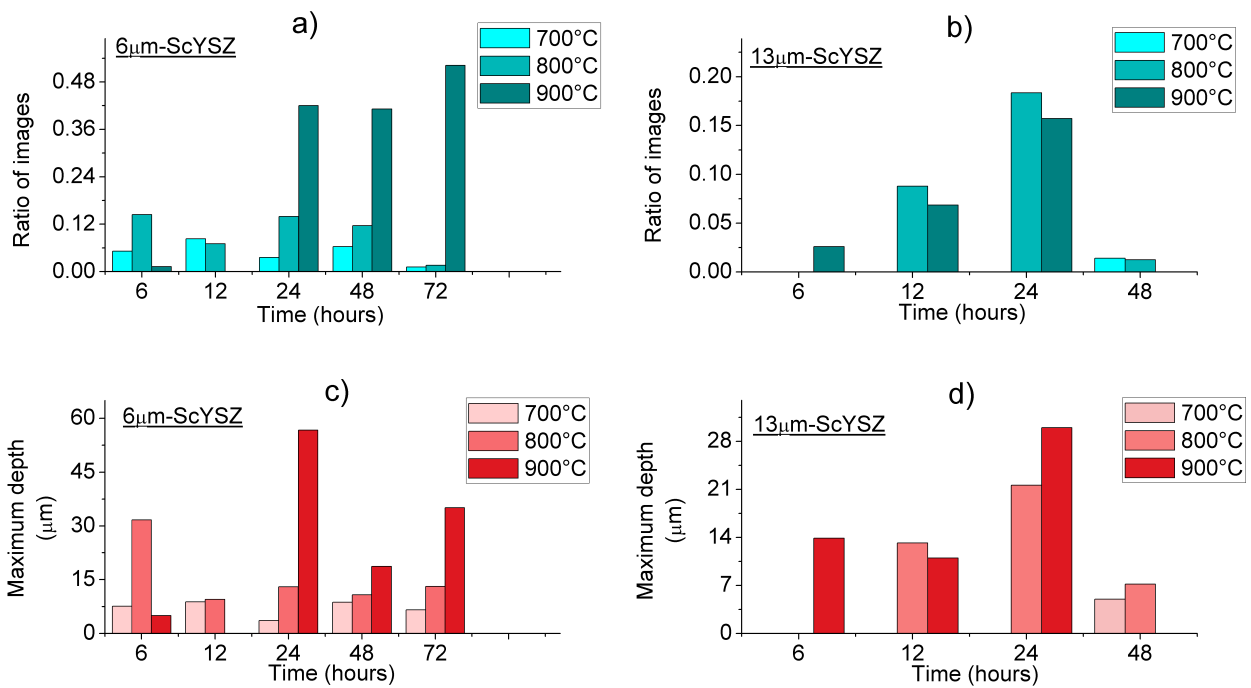


Figure 4.12. Statistics of void formation in ScYSZ. Column bars in a) and b) indicate the ratio of images where the void formation was observed for 6µm-ScYSZ and 13µm-ScYSZ respectively. Column bars in c) and d) indicate the maximum depth at which voids were found below the anode/electrolyte interface, for both grain size electrolytes.

Note that the cells were tested in the full range of temperatures and durations. Therefore, a missing bar indicates a tested cell where no images containing void formation were recorded.

As shown in Figure 4.12 a) for 6µm-ScYSZ void formation was observed after all tests and temperatures, with exceptions of 900 °C for 12 hours. In the cells subjected to an applied potential

for 24 to 72 hours the occurrences of void formation, in general, increases with the temperature at each operando time. Only at 72 hours, the number of images remains the same at 700 and 800 °C, but then increases at 900 °C to a value consistent to what is observed at 24 and 48 hours. No clear trend was observed in this case for different operando times at the same temperature. A different scenario is observed in the case of the 13 μ m-ScYSZ cells, in Figure 4.12 b) where it appears that the larger grain size delays the onset of void formation at the lowest temperature of 700 °C. From Figure 4.12, it can be seen that statistics derived from quantifying void formation under optimized imaging conditions is limited by the stochastic nature of fracture surfaces between samples.

In Figure 4.12 c) for 6 μ m-ScYSZ the maximum depth where voids were found shows an increase with temperature at each equivalent time: 24, 48 and 72 hours, while no clear relation is observed at 6 and 12 hours. In Figure 4.12 d) there is no observable correlation for 13 μ m-ScYSZ regarding time and maximum depth in the cells. The discussion about the observed poorer statistics of this case, in comparison to 6 μ m-ScYSZ is given in the discussion of this chapter.

It also should be noted that the detection of voids by SEM is dependent on the local fracture path during *post-mortem* sample preparation and the lack of detection is not necessarily an absolute verification of absence of cavities. Several inconsistencies in the trends of number of images and maximum observed depth can be observed in the Figure 4.12. We attribute this scatter to hidden variables. Although great care was taken in following the same protocol by the same person for testing and sample preparation (the author of this work), some variables such as slight differences in the fracturing method could have affected some of the observations. This means that the confidence level in reporting the presence of void formation is significantly higher than in reporting its absence. More work is necessary in order to improve statistics of void observation and thus determine more rigorously the presence/absence of void formation and more reliable incubation periods. An alternative method to quantify void formation is to examine the cross-section of samples after mechanical polishing. Measuring microstructural features on polished planar cross-sections provides stereologically correct quantification features (98), in our case void number density per cubic micrometer. However due to the scale of the voids it is our experience that mechanical polishing obscures the majority of voids due to mechanical damage.

It is also important to highlight that in the cases with most occurrences, 6 μ m-ScYSZ at 900 °C during 24, 48 and 72 hours, the ratio of images with voids is above 40%, therefore void formation should not be considered a rare event in general.

4.5.5 Evolution of R_s and R_p

The evolution of the series and polarization resistances, R_s and R_p , at the operating temperatures of 700, 800 and 900 °C are shown in Figure 4.13.

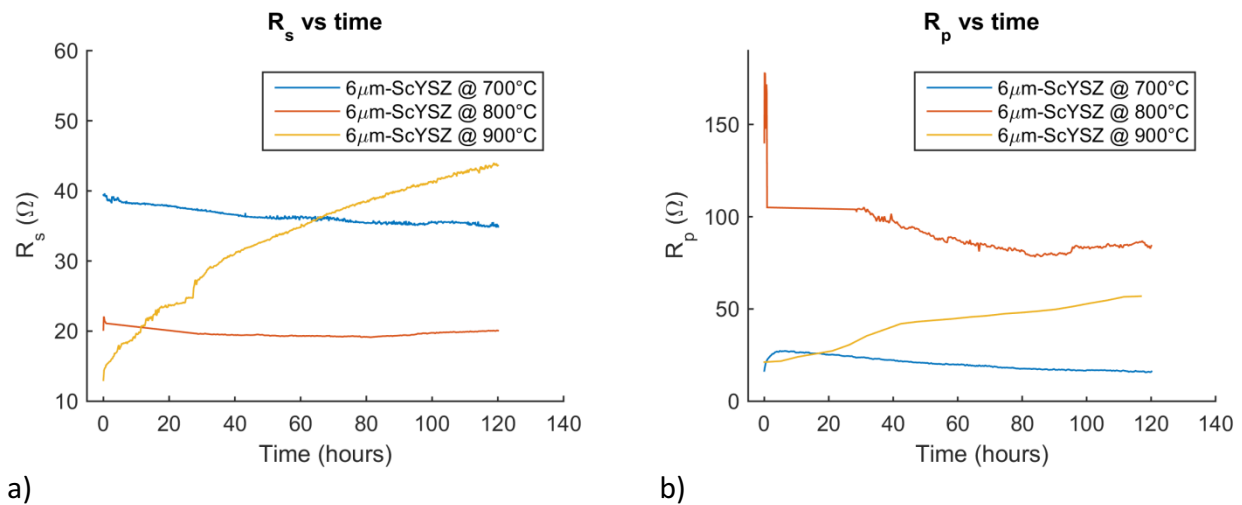


Figure 4.13. Evolution of a) R_s and b) R_p , at anode and cathode sides at different temperatures. the values of resistances in the plots are connected by a line with the corresponding color.

In Figure 4.13 it can be seen that the evolution of R_s and R_p of the cells at 700 and 800 °C are relatively similar, although their average values are different. In both cases the resistances show a very slightly continuous decrease. Only in the case of 800 °C the resistances appear to increase very slowly after 90 hours of operation, that could be associated to a slow degradation of the cell. The erratic behavior of R_p observed in the first 27 hours in the case of 800 °C can be explained by a failure in the measurement, as the EIS took longer than it was programmed. This is not visualized in the R_s plot due to its more stable behavior. In addition, the resistances show a complete stabilization after a maximum of 4-5 hours at operating conditions.

In the case at 900 °C, the behavior is completely different compared to the lower temperatures. It shows a continuous increase, where the final resistances are approximately three times the initial.

This indicates that the cell degrades since the beginning of the experiment, in contrast to the observed at 700 and 800 °C, thus suggesting that at higher temperatures the degradation occurs faster and larger than at lower temperatures at equivalent high polarization.

Moreover, from Figure 4.13 a) it is evident that at the beginning of the experiment (when no degradation has occurred yet) R_s decreases at higher temperatures. This is in good agreement with the reported in the literature, as the ionic conductivity of the electrolyte is directly proportional to the temperature (40) (57) (60). However, the fact that at higher temperatures the ionic conductivity is higher should not lead to the conclusion that the cell performs better over time, as a significant degradation was observed in terms of increasing resistances, including delamination of the anode/electrode interface.

In order to evaluate the initial resistance of the electrolyte used in our experiments, it was compared to the resistance estimated by the ionic conductivity of 10c1YSZ, given by Politova et al. (43) at different temperatures and taking into consideration the dimensions of our cells. The decision of taking the data from the cited author is based on the similarities of the electrolyte in terms of fabrication method and grain size, as presented in Table 2.1. The equation that correlates the resistance to the resistivity/ionic conductivity of the material and the dimensions of the cell is given by the following expression:

$$R = \rho \frac{L}{A} = \frac{1}{\sigma} \cdot \frac{L}{A} \quad (\text{Eq. 4.2})$$

Where R is the resistance, ρ is the resistivity; L is the length of the material in the direction of the current, that in this case is the thickness; A is the cross-section of the cell perpendicular to the current direction and σ is the ionic conductivity, which is the inverse of the resistivity.

The expected resistances of the electrolyte, denoted here as R_{exp} , and our experimental R_s determined by EIS at the stated temperatures are shown in Table 4.1. Only the experimental R_s at initial time were taken for each tested cell, as degradation is not expected to occur yet.

cell	Expected resistance R_{exp} (Ohm)	Experimental R_s (Ohm)
6 μ m-ScYSZ @700°C	11.9	39.4
6 μ m-ScYSZ @800°C	4.0	20.2
6 μ m-ScYSZ @900°C	2.3	13.0

Table 4.1. Expected and experimental values of R_s according to the temperatures.

As can be seen from Table 4.1 the experimental R_s are approximately 3 to 5 times higher than the expected electrolyte resistance at equivalent temperatures. Ideally, the R_s should be equivalent to the electrolyte resistance. However, the R_s estimated here is the total ohmic resistance of the system, with contributions not only from the electrolyte resistance, but also from the resistances of the materials present in the entire system and from our particular experimental setup and defects during assembly. Therefore, a discussion about some of the possible contributions to the overall resistance, apart from the electrolyte resistance, is given in the following list:

- Contact losses: mismatch of thermal expansion coefficient of the components of the cell when rising from room temperature to operating temperature, may cause cracks and delamination, mainly close to the electrode/electrolyte interfaces even before starting to operate as an electrochemical cell. This results in a decrease of contact region, thereby increasing the total resistance.
- Electronic sheet resistance: the resistance of every material is directly proportional to its length along the main direction of the current and inversely proportional to the cross-section of the conductor perpendicular to the direction of the current, as can be derived from Eq 4.2. In our case a significant part of the electrodes is not in direct contact with the metallic interconnectors. Thus, the electrons experience resistance when traveling across the region that is not directly connected to the Pt cables, resulting in a current distribution gradient along the direction of the electrode/electrolyte interface and its effects depend strongly on its size, porosity, tortuosity and percolation, with an increasing resistance when moving away from the current collectors. In our case this resistance should not be ignored, as the length of the electrodes without current collector is around 2 mm and its thickness is 5-10 μ m, as shown in Figure 4.14. This is supported by mathematical models proposed by

Bessette et al. (99), in which local current density was found to be around three times higher near the contacts than in the midway between contacts. Furthermore, in the work by Tanner and Virkar (100) they found an increase of the area specific resistance with increasing interconnect contact spacing for one and two-dimensional interconnect geometries. In addition, contacts between Pt paste, electrodes and Pt cables and the porosity of Pt paste may also contribute to a higher resistance of the cell, as they usually do not perfectly make contact on the entire surface.

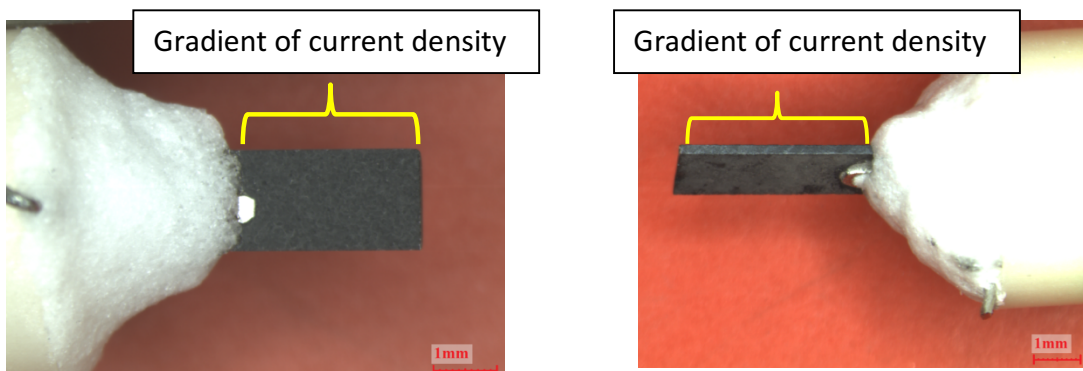


Figure 4.14. Exposed areas of the electrodes (without direct contact of current collector). The resistance of this section of the cell is expected to have higher resistance than the section in direct contact with the metallic contacts, with a gradient of the current density mainly in the direction from the metallic contact to the tip of the cell, according to the properties of the electrodes.

- Pinholes: pinholes found in the electrolyte (see §4.5.2), as well as porosity are very likely to remain from the fabrication process of the material due to, probably, an incomplete sintering process. Porous regions and/or pinholes result in a decrease of the ideal density, which is 100% for a non-porous electrolyte. A decrease of ionic conductivity, corresponding to an increase of resistivity/resistance, has been associated to a decrease of density due to porosity (including pinholes in our case) as ions can only move through the dense material and not through the pores (60).
- Defects of electrodes: inhomogeneity of the thickness of electrodes and distribution of materials can cause gradients of current distribution in the electrolyte, thus influencing the total ohmic resistance.

For a better comparison of the resistances in our experiments, it is recommended to find the ionic conductivity of 10Sc1YSZ sintered in the same conditions as in our work, with a resulting grain size in the order of 6 μm .

Furthermore, from the data in the Figure 4.13, the losses from contact area can be easier to discern by plotting the ratio of the resistances with reference to the initial resistances, as recommended by J. Hjelm (private communication, June 2018: Lecturer at DTU, Department of Energy Conversion and Storage). It consists specifically to plot $R_s/R_s(\text{initial})$ vs $R_p/R_p(\text{initial})$, so the losses by contact area correspond to slope close to 1, as the relative changes of resistances vary in the same rate (7). In Figure 4.15 this relation is illustrated, where A, B and C represent the time line from initial to final time. Here the segments from A to B and from B to C are called AB and BC respectively.

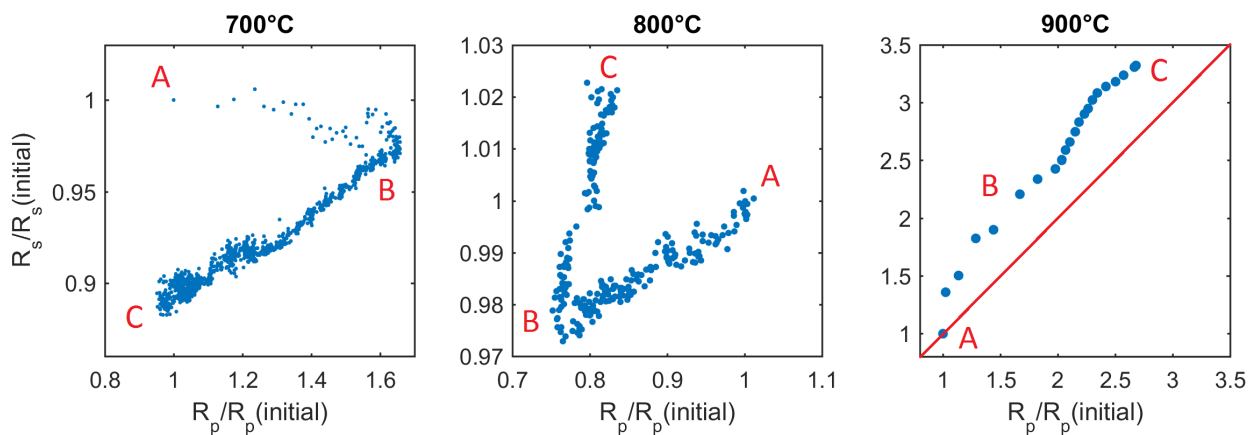


Figure 4.15. Relation between the evolution of resistances compared to their respective initial resistances.

In Figure 4.15, at 700 °C no evident losses related to contact area can be seen in AB, which is probably due to some instabilities of the cell during the first 5 hours (point at B). At BC there is a more clearly linear correlation; however, the slope of 0.2 does not indicate contact area losses.

At 800 °C the EIS scans at 0.9 hours took approximately 27 hours by accident during data acquisition, thus the first 11 scans were removed in the plot of Figure 4.15. Two linear behaviors can be observed, where B corresponds to a time near 83 hours. However, the slope of AB and BC

correspond to 0.1 and 0.4 respectively, showing no evident correlation to contact area losses, as similarly observed in the case at 700 °C.

At 900 °C the ratio of the resistances increases continuously from A to C, showing a more evident linear dependence. Excluding the first value due to stability issues, the estimated slope is 0.9, strongly suggesting that the changes of R_s and R_p are essentially due to contact area losses (7). This agrees well to the delamination observed in the sample with smaller grain size electrolyte at 900 °C and a polarization of 2V during 72 hours, see Figure 4.7 b).

4.5.6 Evolution of pO_2

In Figure 4.16 the evolution of the oxygen partial pressures at the anode and cathode is shown for the cells at temperatures of 700, 800 and 900 °C in air at a polarization of 2V during 120 hours of testing.

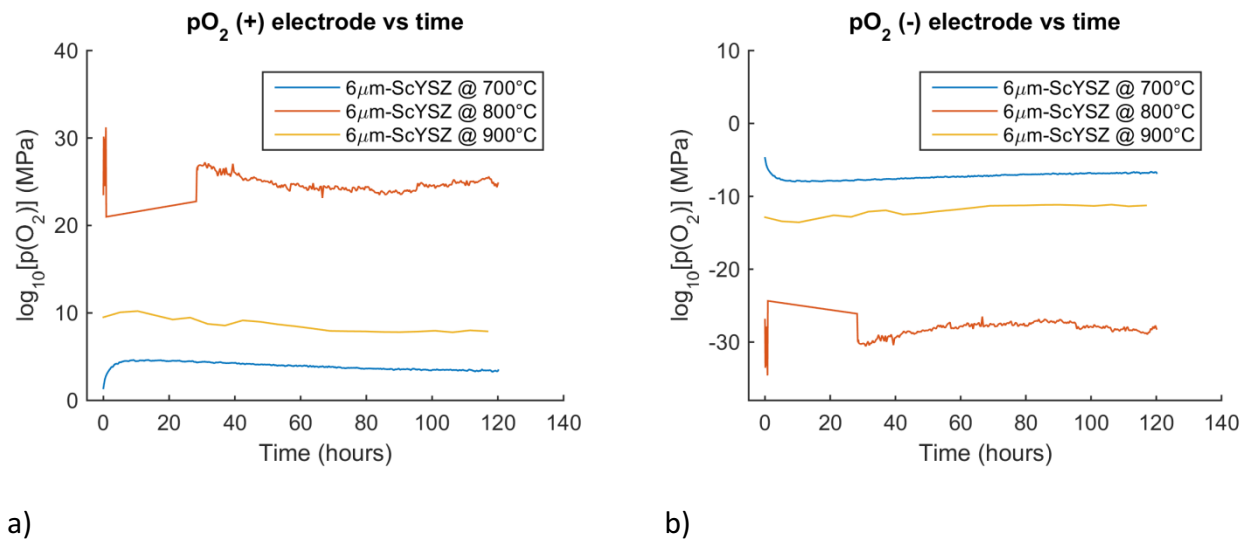


Figure 4.16. Evolution of pO_2 at a) the anode and b) the cathode, denoted here as (+) and (-) electrodes respectively.

As can be seen in Figure 4.16 the pO_2 at the anode is very large, mainly in the cases at temperatures of 800 and 900 °C; with a pO_2 above 10^8 MPa. In the case at 700 °C the pO_2 starts at a relatively low value, increasing continuously during the first 4-5 hours and reaching a pO_2 close

to 10^5 MPa, which can be ascribed to some stabilization of the cell. After that time, the pO_2 shows a more stable behavior with a very slow decreasing rate.

In contrast, the pO_2 at the cathode are extremely low in the cases at 800 and 900 °C, within a range between 10^{-27} – 10^{-32} MPa and 10^{-10} – 10^{-12} MPa respectively, whereas for 700 °C the pO_2 remains between 10^{-5} and 10^{-8} MPa.

Very low pO_2 have been associated to local electrolyte decomposition of YSZ into metal phases of Y and Zr, as reported by Virkar (31). In his work, an electrochemical model for degradation in solid oxide cell in electrolysis mode is used, based on thermodynamics equilibrium in which the author states that local electrolyte decomposition may occur if the pO_2 drops below a certain value. As an example given by the same author, at 800 °C the decomposition starts at pO_2 below 2.8×10^{-45} MPa. This is in good agreement with the pO_2 at which ZrO_2 starts to reduce under the same temperature, based on Ellingham diagram provided by Torben Jacobsen (see Figure 9.1 in the Appendix), in which the pO_2 is in the order of 10^{-45} MPa.

According to the Ellingham diagram the pO_2 at which ZrO_2 starts to reduce is, in general, much higher than that of Sc_2O_3 and Y_2O_3 , thus the stability of the former oxide is much lower than the latter.

Based on that diagram, table summarizes the pO_2 at 700, 800 and 900 °C at which reduction into Zr, Sc and Y can be observed.

Temperature (°C)	pO_2 (MPa) Zr	pO_2 (MPa) Y and Sc
700	10^{-49} (*)	10^{-59} (*)
800	10^{-45}	10^{-53} (*)
900	10^{-41}	10^{-47}

Table 4.2. Values of pO_2 at which reduction into Zr, Sc and Y starts to occur at the temperatures used in this work. (*) indicates values estimated by the extrapolation of the data in the Ellingham diagram. pO_2 of Y and Sc are shown together in the table as they are very similar.

4.5.7 *In-operando* study of grain-averaged electrolyte d-spacing change

Figure 4.17 the evolution of the average d-spacing is shown as a function of distance from the positive electrode, with reference to the cell at 700 °C and no applied voltage (black horizontal line at 0 relative d-spacing). The various lines represent the different combinations of applied voltage and electrochemical operation time. The location of the vertical dash-dotted lines delimit the anode and cathode / electrolyte interfaces as determined by the number of diffraction spots on the detector as the 17 μm FWHM line beam was scanned across the cell edge.

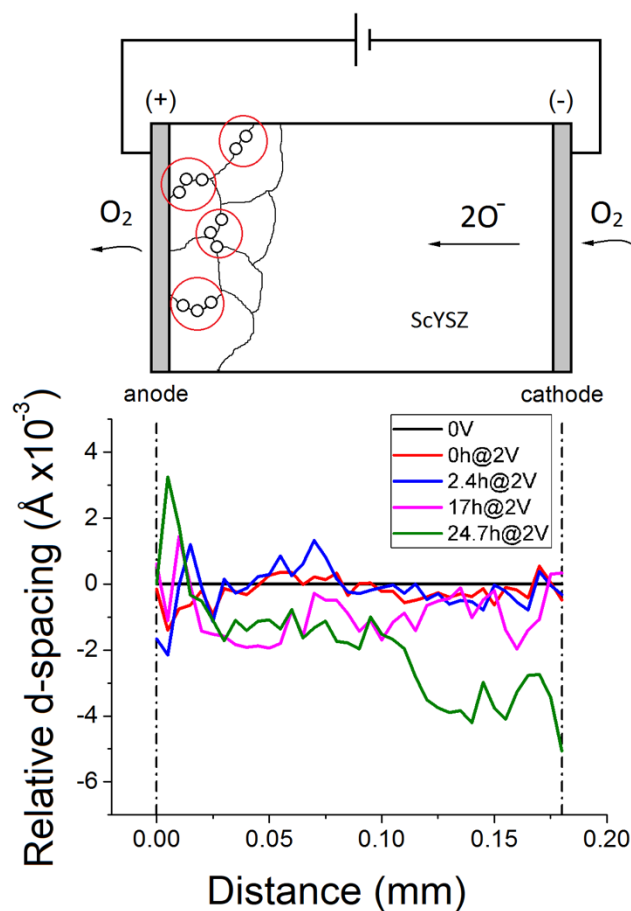


Figure 4.17. *In-operando* study. Above a schematic view of the electrochemical cell setup with the expected oxygen void formation close to the anode. Irregular black lines and small black circles are representations of grain boundaries and void formation, marked with red circles. Bottom: evolution of d-spacing as a function of distance from positive electrode with respect to the reference condition, at 700 °C and 0V (black horizontal line).

Within statistical uncertainty, there is no immediate change in d-spacing when applying the voltage, as evidenced by the black and red lines in Figure 4.17. The d-spacing did not change significantly during the first 2.4 hours either, see blue line. After 17 hours a decrease of d-spacing in the order of $1-2 \times 10^{-3} \text{ \AA}$, as compared to the previous stage, was observed in the region from the electrolyte/anode interface to the middle of the electrolyte. However, an even more distinct change in d-spacing was observed at 24 hours, see green line, with a strong decrease of d-spacing towards the cathode/electrolyte region in the order of $4 \times 10^{-3} \text{ \AA}$. The fluctuations within the first $15 \mu\text{m}$ of the electrolyte from both anode/electrolyte interfaces can be attributed to the geometry of the cell, the beam width and a relatively poor grain statistic. A more stable behavior was observed close to the cathode/electrolyte interface.

4.5.8 *In-operando* mapping of the strain evolution within a ScYSZ grain

To investigate the feasibility of mapping changes in the internal strain within a grain (type III stresses) during cell operating, one average sized grain was selected and subjected to dark field microscopy at regular intervals during the annealing. This grain was located within $25 \mu\text{m}$ from the anode/electrolyte interface. By combined translation/rotation of the objective and a translation of the detector we effectively scanned the scattering angle 2θ around its nominal position -14.186° and within a range of $\pm 0.05^\circ$. In this way maps of the axial strain is provided (28).

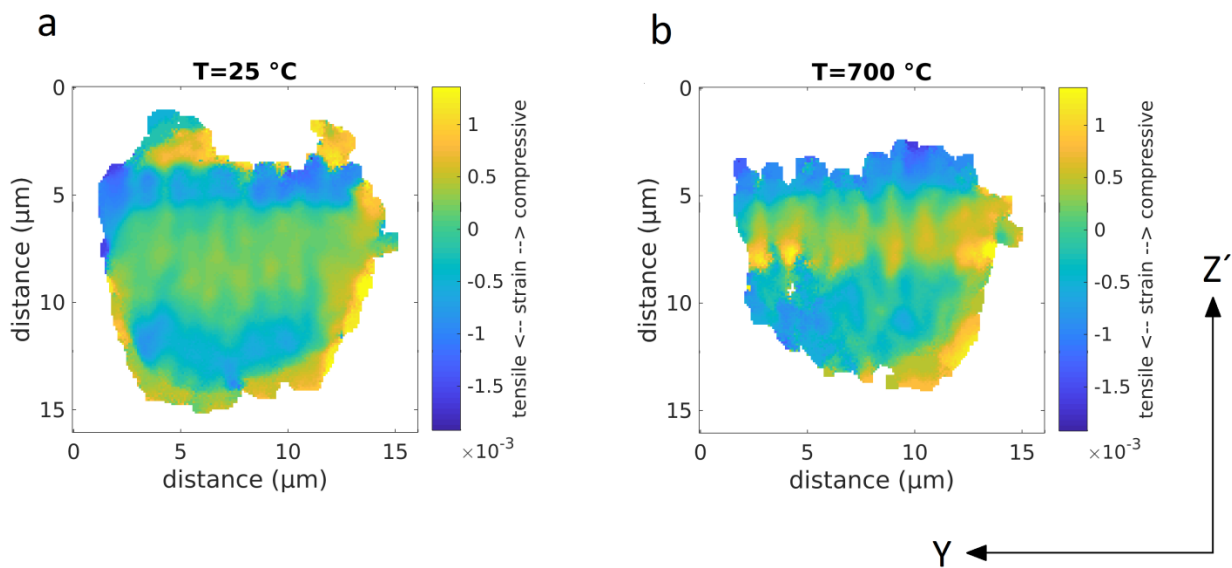


Figure 4.18. Strain maps of a grain close to the anode/electrolyte interface. Positive and negative values imply compressive and tensile strain respectively. a) Grain at room temperature and no applied voltage. b) The same grain at 700 °C under polarization after 10.5 hours at operating conditions. The anode/electrolyte interface is above the image. The “y” axis is defined in Fig 1 while the z' -axis represents the z axis depending on 2θ . The pixel size is 0.1 μm and the color bars have the same scale.

Notably these maps are 2D projections of the grain, as the beam height is larger than the grain size. Shown in Figure 4.18 are strain maps acquired initially – at room temperature – and after 10.5 hours of operation at 2V.

At initial conditions, regions with compressive strain in the order of 1×10^{-3} and larger are localized mostly close to the grain exterior. Regions with strain between 0.5×10^{-3} and -0.5×10^{-3} are distributed inside the grain. After 10.5 hours, an increase of local compressive strain in the central regions from approximately 0.7×10^{-3} to more than 1×10^{-3} is observed.

4.5.9 TEC measured by DFXRM

The result presented in this section was achieved from the *in-operando* experiment; however, it does not provide meaningful information that can be interconnected to the other results, as it is limited to the thermal expansion coefficient measurement of ScYSZ. Nonetheless, it is included here in order to show another capability of the X-ray microscope. Therefore, the methodology, values and relevant discussion are given within this section only.

In order to measure the TEC of this materials, the position of the grain found for strain mapping (see §4.5.8) was tracked from RT to 700 °C by means of the DFXRM setup. The Eq 3.3 was used as it correlates the change in dimension of the material to the temperature. Here it is valid to assume that the initial and final lengths, L_0 and L_f in Eq 3.3 correspond to the initial and final d-spacing of the (111) diffraction line of ScYSZ. To estimate the change of d-spacing, the angular position of the objective lens was taken at both temperatures, with the projection of the diffracting images kept as much as possible invariable in the Far Field detector.

The TEC given by this method is $10.3 \pm 0.8 \times 10^{-6}/^{\circ}\text{C}$. The error was estimated by error propagation of the uncertainty of the objective lens and the temperature. The uncertainty of the objective lens is defined by the optics mounted on the stage, by considering two pinholes with size equal to the small Be lenses at the two ends: diameter of 0.5mm and a distance between them of 150mm, which is the total length of the objective lens. With this consideration an overestimate error is given by C. Carsten (private communication, January 2018: ESRF, Beamline ID06). Better error value should be considered due to the parabolic shape of the lenses, which reduces the field of view of the transmitted beam. Here the error of the objective lens position is not taken into account as the precision of the 2θ angle given by the corresponding motor position is in the order of $3^{\circ} \times 10^{-5}$.

The uncertainty of the temperature was taken empirically as $\pm 10^{\circ}\text{C}$ as the maximum variation of temperature during calibration. After a long literature search, it was not possible to find the TEC for this material, however the TEC for the commonly used 8%YSZ is in the range between 10 and $11 \times 10^{-6}/^{\circ}\text{C}$ (46) (47) (101). We believe that the reported TEC of ScYSZ in our measurement is consistent to what should be expected, as this material is also used as electrolyte with common Ni/YSZ and LSM/YSZ electrodes. One has to be careful with this result of TEC using the described

method as in many cases the TEC of materials is given by dilatometry. Different methods could lead to different values of TEC. As opposed to other methods, like powder X-ray diffraction and dilatometry, the method presented cannot be considered as representative of the complete sample, since it is only for a single grain. Nevertheless, this method can be a powerful technique due to the high angular resolution of the beamline setup. The most important limitation in this particular setup is given by the uncertainty of the temperature, as it was measured by indirect method as described in §4.4. It is expected then that the accuracy/uncertainty of TEC can be improved by lowering the uncertainty of the temperature.

4.5.10 Characterization of grain boundary void formation after operation

A *post-mortem* analysis of the 13 μm -ScYSZ-op cell by SEM reveals the presence of void formation in the grain boundaries of the electrolyte close to the anode/electrolyte interface, as illustrated in Figure 4.19, confirming the expected from the results of the void statistics experiments. The voids observed in the 13 μm -ScYSZ-op appear at a maximum depth of approximately 10 μm into the electrolyte from the anode/electrolyte interface, comparable to the depth observed in the equivalent condition of the void statistics experiments, shown in Figure 4.12.

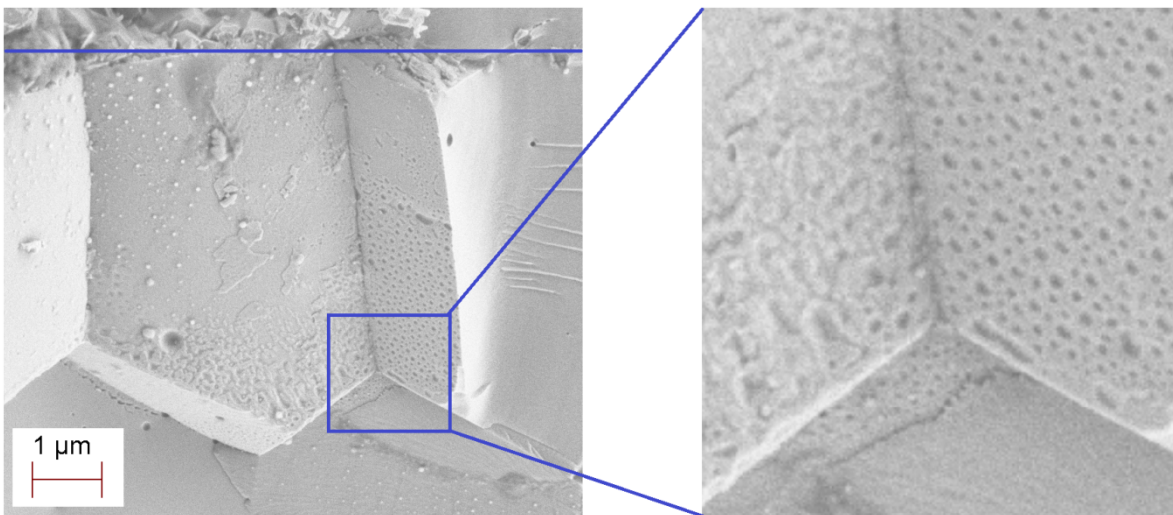


Figure 4.19. SEM micrographs of post-mortem fractured of 13 μm -ScYSZ-op revealing void formation in the electrolyte near the anode/electrolyte interface. The blue horizontal line marks the interface between electrolyte (below) and anode (above). To the right a 4.2X magnified image of the area indicated by the blue box.

4.6 Discussion

4.6.1 Conditions and factors influencing void formation

The present work, as illustrated in Figure 4.12 shows that under realistic operating conditions at high polarization, electrolyte grain boundary void formation onset commences within a few hours and is relatively independent of typical operation temperatures. In the case of 6 μm -ScYSZ the incubation period appears to be shorter than 6 hours at all three temperatures. The presence/absence of void formation for 13 μm -ScYSZ, suggests that the grain size has an effect on the incubation period, as there appears to be a great absence of voids at the lower temperatures. An analogous hypothesis of an incubation period is also supported by Graves et al. (7), in which a YSZ cell with Ni-YSZ and LSM/YSZ as fuel and oxygen electrodes respectively was reversibly tested at 800 °C, in cycles of electrolysis and fuel mode every 5 hours each under a current density of -1/+0.5 A/cm² respectively. This treatment limited the cell voltage to 1.33 V in electrolysis mode in comparison to a cell run at equivalent electrolysis conditions where the cell voltage climbed steadily to 1.73V in over 400 h. No significant degradation occurred in cycling mode, with no void observation after hundreds of hours of test. For the cell at constant current, void formation was observed under continual electrolysis operation after reaching high values of cell potential. This suggests that an incubation period exists in which the critical level of high internal oxygen pressure is not reached and oxygen pore formation can be avoided by maintaining a low cell voltage. Alternatively, if void formation occurs, it is hypothesized by Graves et al. (7) that in the fuel cell mode voids can be removed by pumping the oxygen, when the pO_2 is lowered. However, no microstructural evidence is provided, establishing that either void formation occurs continuously with increasing cell voltage or that a limiting cell voltage for void formation initiation exists. Furthermore, no evidence exists to our knowledge that once a void is formed for a given cell voltage that void can be removed again.

To our knowledge void formation has previously only been reported for YSZ (7) (8) (10). The present work reveals that void formation occurs under similar operating conditions and with a similar morphology in ScYSZ. Moreover, the incubation time is shown to be as short as 6 hours,

comparable to what observed by Graves et al. (7). Consistent void formation in both these materials thus suggests that the stabilizing dopant Y_2O_3 / Sc_2O_3 does not have a significant effect on void formation based on our available results. A systematic study exploring varying dopant ionic conductivity is therefore needed to establish dopant effects on the evolution of void formation.

The higher occurrence of void observations in $6\mu\text{m-ScYSZ}$ in comparison to $13\mu\text{m-ScYSZ}$ in the addressed temperature and time range may suggest a dependence of this effect on the grain size, and thus the grain boundary specific interface area. This, in addition to the observation of voids close to pinholes and cracks, may suggest that reducing and/or eliminating these defects and reducing the grain boundary interface area could be a mitigation mechanism to reduce the nano-sized void formation, thus increasing the lifetime of the cell.

As claimed by many authors, void formation is believed to be caused by a build-up of oxygen pressure due to the distribution of electrochemical potential inside the electrolyte (7) (8) (10) (31). Kim et al. (102) suggested that the detected presence of La, Sr and Mn impurities along the grain boundaries of YSZ by EDS could be considered as a sink to release electrons from the oxide ions, where oxygen gas builds up, thus resulting in high oxygen gas pressure at grain boundaries and intergranular fracture. However, diffusion of these elements into the ScYSZ was not detected in our case, based on the sensitivity of our EDS analyses.

The calculated high pO_2 at the anode/electrolyte interface, shown in Figure 4.16 a) is in good agreement with the stated by several authors concerning oxygen build-up in this region of the cell. Based on the analogy between the samples used in the EIS experiments and void statistics experiments at equivalent operating conditions, the presence of voids in the $6\mu\text{m-ScYSZ}$ at $700\text{ }^\circ\text{C}$ suggests that this phenomenon can arise at pO_2 in the range between $10 - 10^5$ MPa during 6 hours of operation at constant polarization; however, no accurate threshold of pO_2 within this range can be given based on our available data. Delamination observed in $6\mu\text{m-ScYSZ}$ at $900\text{ }^\circ\text{C}$ during 72 hours test is also in good agreement with the minimum value of pressure of 10 MPa, predicted by Virkar (31) to be sufficient to cause delamination of the anode. No delamination was observed at 700 nor $800\text{ }^\circ\text{C}$, with the latter having the highest pO_2 levels, suggesting that the delamination observed in the case at $900\text{ }^\circ\text{C}$ can be a contribution from the high pO_2 at the interface during

several hours and the mismatch of thermal expansion of the materials composing the anode and electrolyte.

Moreover, the occurrences of void formation at 700 and 800 °C do not show an evident correlation to R_s and R_p . We can only conclude that, apparently, voids can arise even with negligible degradation of the cell in terms of resistances. Only in the case of most extreme conditions, 900 °C at 2V, the R_s and R_p are consistent to the higher degradation observed, based on the presence of delamination and amount of voids, as shown in Figure 4.7 and Figure 4.12 respectively. This agrees well to the results reported by (18; 2), in which an evident increase of resistances was observed in a YSZ electrolyte based cell with LSM/YSZ electrodes in a symmetrical configuration at 800 °C in air and under a current density of 1.5 A/cm² in electrolysis mode. The high degradation rate observed in their experiments at 800 °C is probably due to the applied high current density, which can be analogous to the degradation at 900 °C in our experiment.

4.6.2 Microstructural changes close to the anode/electrolyte interface

As shown in Figure 4.19, the *in-operando* cell 13 μ m-ScYSZ-op, shows void formation after 32 hours. As we evidently have no similar *post-mortem* analysis at shorter times, we cannot prove the existence of void formation at earlier times. However, the decrease of d-spacing at 17h@V and 24.7h@V indicates an increase of compressive stress at the anode side. Assuming that all changes in d-spacing are stress induced, using a Young's Modulus of 158 GPa for 6mol%ScYSZ at 700 °C (103), the axial stress is close to 100 MPa within the first 100 μ m of the electrolyte for the 24.7 hour case. This value of stress is one order of magnitude larger than the 10 MPa predicted by Virkar (31) to be sufficient to cause delamination of the anode, although no void formation is mentioned in that study. In the present study both delamination and voids were observed only in the SEM images related to the most extreme case: 6 μ m-ScYSZ at 900 °C for 72 hours. Analogous delamination have been observed by Cheng and Jiang (104) in cells composed by LSM electrodes and YSZ electrolyte under current densities of 0.5 mA/cm² in electrolysis mode at 800 °C in air, with an increase of anodic polarization potential from 1.12 to 1.73 V, where a proposed mechanism of this effect is also described.

The unique X-ray microscopy results presented in Figure 4.18 demonstrate the feasibility of *in operando* mapping of the individual grains. The increase of local strain areas in Figure 4.18 b) is

consistent with an increase of the overall strain of the grains close to the anode/electrolyte interface as evidenced by Figure 4.17. We interpret the changes between the left and the right figure as indicative of strain localization at the grain boundaries: the pre-cursor of the pore formation. More specifically:

- The morphology of the grain projection is not the same in the two maps in Figure 6. In particular, some areas are missing in the outer parts of the treated grain where these locations no longer locally meet the Bragg condition. This indicates that these zones either experience: a) local crystal rotation greater than the $\pm 0.05^\circ$ rotation in rocking angle performed during each scan and/or b) extremely high axial strain corresponding to variations in the lattice parameter of $\Delta 2\theta > 0.05^\circ$, i.e. on the order of $\pm 35 \times 10^{-3}$ or larger. However, elastic axial strains at these extremes are unlikely as they correspond to stresses on the order of 5 GPa and would thus either result in fracture, or local lattice rotation consistent with a). In other words, regions at the grain boundaries are experiencing significant local deformation. Kim et al. (105) reported complete separation of grain regions as intergranular cracks in a YSZ electrolyte operated at 750 °C for 120 hours in air under high current density. It should be noted the outer shape of the grain and values of inner strain may be influenced by the chosen level of background intensity, which is selected visually by setting a suitable value to remove single and weak pixels without removing what appears to be the grain. However, in our case the same procedure is applied in both images.
- The horizontal band with nearly regularly spaced yellow vertical intensity ridges appearing in Figure 6b may indicate an array of hot spots appearing at the top or bottom surface of the grain investigated. Notably the local strain would be substantially larger than the 10^{-3} indicated, as the figure is a projection over the entire grain.

4.6.3 d-spacing decrease close to the cathode/electrolyte interface

The observed decrease in d-spacing near the cathode side of the electrolyte at 24.7 hours at operating conditions is an unexpected result and presently there are no definitive mechanisms available to explain this phenomenon. A rigorous investigation for sources of experimental artefacts that could replicate this observation was performed. The relevant sources of error are

associated with sample or detector drift during the course of the 24-hour scan. Investigation of potential drifts for each detector/sample coordinate axis however proved to be internally consistent. It was thus concluded, within the resolution limits, that the potential artefacts do not explain the magnitude of the observed change in d-spacing in Figure 4.17.

We speculate that the effect of d-spacing decreasing may be related to an increase in oxygen vacancy concentration close to the cathode region and/or the cathode itself. Studies by Ruh and Garet (106) have revealed a decrease in the unit cell volume of oxygen-deficient ZrO_2 when firing and quenching it at high temperature. It is suggested in their work that the decrease of lattice parameter is due to oxygen missing.

The causes for oxygen deficiency in our ScYSZ electrolyte could be potentially associated to the following mechanism: decrease of TPB due to coarsening of the LSM phase (107), oxygen depletion due to gas diffusion limitation in the LSM cathode (108) and partial delamination and/or microcracks at the cathode/electrolyte interface.

According to the results from the electrochemical impedance studies given in §4.5.6, in none of the cases at different temperatures the pO_2 is low enough to cause reduction of ZrO_2 into Zr. The reduction of the oxides Sc_2O_3 and Y_2O_3 into their metallic phases are not even considered here as they reduce in a much lower pO_2 than ZrO_2 . Therefore, it is valid to assume that the contraction of the lattice in the ScYSZ electrolyte is not attributed to a cation radius change due to reduction. As a result, the lattice decrease can be associated to electrostatic interactions due to oxygen vacancy formation/oxygen deficiency, as claimed by Marrocchelli et al. (67) in their chemical expansion studies, based on atomic scale computer simulations by molecular dynamics and density functional theory using ZrO_2 .

If the oxygen reduction rate at the cathode/electrolyte interface is limited, insufficient oxide ions will be supplied via the electrolyte to the anode. In this case, it is reasonable to assume that oxygen from the ScYSZ lattice can be extracted in order to maintain the electrochemical reaction, promoting an oxygen deficiency in the structure close to the cathode.

Therefore, the oxygen deficiency or increase in oxygen vacancy concentration in the electrolyte region close to the cathode at operating conditions could explain the observed decrease of d-spacing after 24.7 hours. In addition, the negligible d-spacing change at 17h@2V in comparison to

0h@2V close to the cathode/electrolyte interface region may indicate a threshold time in which oxygen vacancy concentration starts to increase, shown in the right side of the plot in Figure 4.17.

4.7 Conclusions

In this chapter, the degradation of ScYSZ electrolyte based solid oxide cells was studied in terms of void formation, electrochemical and microstructural parameters by means of *post-mortem* analysis and *in-operando* experiments. Furthermore, a novel method to fabricate the cells was presented in order to meet the limitations dictated by the synchrotron experimental setup.

To study the void formation, several in-house experiments were performed in symmetrical cells composed by ScYSZ electrolyte and LSM/YSZ electrodes in air at typical SOCs operating temperatures under strong polarization, during times from 6 to 72 hours. Extensive *post-mortem* SEM on fractured samples revealed, for the first time to the best of our knowledge, void formation in ScYSZ electrolyte grain boundaries close to the anode/electrolyte interface. The voids appeared at times as short as 6 hours and based on the occurrences, showing a dependency to the electrolyte grain size, suggesting that grain boundaries can act as nucleation sites, as well as pinholes and cracks. In the case of smaller grain size electrolyte, the occurrences show an evident relation to the operating temperatures in the interval between 24 and 72 hours. The overall high levels of pO_2 from EIS experiments are in good agreement to the stated by many authors that voids are caused by a build-up of oxygen pressure at the anode/electrolyte interface. In addition, voids could be formed within a range of pO_2 between $10 - 10^5$ MPa, although no exact value can be given from our available data. Also, degradation of the cell in terms of R_s and R_p seems not to be necessarily related to void formation at 700 and 800 °C. However, the higher degradation observed at 900 °C in terms of voids occurrences and delamination can be related to the increase of resistances.

XRD is presented to *in-operando* study a geometrically improved cell at 700 °C in air and a polarization of 2V. The evolution of lattice microstructure in terms of d-spacing of the (111)ScYSZ was assessed by classical XRD, showing a contraction of the lattice close to the anode/electrolyte interface after 17 hours of operation. This is possibly associated to the compressive effect of

oxygen gas build-up, as evidenced by the high pO_2 from EIS experiments. A decrease of electrolyte d-spacing close to the cathode interface was observed and is tentatively associated to an increase of oxygen vacancy concentration in this region due to oxygen deficiency caused by degradation factors occurring at the cathode. Within the grains, DFXRM showed an increase in local compressive strain inside the projection of the grain and rotated regions at the edges after 10.5 hours - both consistent with strain localization at the boundary of the grain.

5. *In-operando* experiment on YSZ electrolyte based cell with Ni/YSZ cathode under high polarizations

5.1 Introduction to the chapter

One of the most common materials used in fuel electrode of SOCs is Ni, which is commonly mixed with YSZ to form the Ni/YSZ cermet with improved properties. Due to the operating conditions Ni/YSZ electrode exhibits degradation. This has been extensively studied, in which coarsening of Ni particles, oxidation, segregation and formation of new phases and nanoparticles have been reported as common degradation mechanisms, having a negative impact on the lifetime and performance of the cell (13) (14) (27) (109) (110).

The present chapter is motivated mainly by one of the above cited works, i.e. Hansen et al. (13). In their work, they studied the effects on the microstructural changes of Ni-YSZ interface caused by strong cathodic polarization by means of EIS and SEM. The experiment consisted on a cell composed by pure Ni wire, bent in a U-shape and electro-polished and pressed against a polished surface of 8%mol YSZ disk, with a large Pt painted electrode on the opposite side. In all the tested samples the temperature was 900 °C in an atmosphere composed by 97% H₂ in 3% H₂O. A strong cathodic polarization in the range between -1.8 and -2.4V, relative to a standard oxygen electrode, was applied between the electrodes. *Post-mortem* SEM/EDS of the cross-section of Ni wire and YSZ electrolyte revealed complex microstructures and intermetallic phases, such as ZrO₂, Ni-Zr, Yttria nanoparticles and intermixed Ni-ZrO₂ up to 20 μm from both sides of the Ni - YSZ interface. A mechanism of the formation of nanoparticles is proposed by the authors.

As known, impedance spectroscopy and electron microscopy are two powerful tools used in materials science. However, in SOCs studies, while EIS provides valuable electrochemical information during operation of the system, the technique does not directly provide microstructural characterization, and electron microscopy is typically limited to *post-mortem* analyses. This leads to hypothesis and/or proposed mechanisms in an attempt to explain the microstructural changes, based on the information given by these techniques with the limitations

stated above. Hence, the use of alternative tools capable for *in-operando* studies can potentially complement and support the findings in this kind of investigations. As it was demonstrated in the previous chapter, XRD is a suitable technique for such purposes, and when combined with other tools capable of providing information during operando, it enables exceptional opportunities on the investigation of SOCs field.

Therefore, in this chapter XRD is simultaneously combined with EIS to *in-operando* study the microstructure during degradation of an electrochemical device, complemented by *post-mortem* SEM/EDS. The study aims to directly reveal similar phases as reported by (13), arising close to the interface of interest and also to correlate microstructural changes to electrochemical information during operando conditions. The experiment is carried out on a 8%mol YSZ electrolyte based cell with Ni/YSZ and Pt electrodes in a reducing atmosphere of wet 5% H₂ in N₂, under different polarizations up to -1.8V and a temperature of 650 °C during a total of 38 hours. To conduct this study, an improved sample setup is developed based on the experience gained previously (see Chapter **Error! Reference source not found.**). To overcome the challenge of providing gas environment at high temperature a novel method is described based on the use of quartz tubes. The high temperature is provided by a IR furnace, suitably modified by us for performing XRD. The polarization is applied by a potentiostat, capable to simultaneously perform electrochemical impedance measurements.

To the best of our knowledge, this is the first time to carry out such experiment; therefore, this is a major step forward in terms of sample preparation/setup and combined testing using two very powerful techniques for materials characterization in operando conditions. In the following sections, a complete description of the sample preparation, experimental setup, methodologies and results are presented.

5.2 Sample and sealing

In the following sub-sections, a description of the sample materials, fabrication, sintering processes and assembly of the components is given. This was successfully achieved based on our previous experience in the sample preparation described in Chapter 4. As in this experiment a

reducing gas environment needs to be provided at high temperature, the solution was found on the use of quartz tube. Consequently, a more challenging assembly procedure is developed here.

5.2.1 Sample materials

The electrolyte was made from a ceramic powder provided by Tosoh Corporation, Yamaguchi, Japan. The powder consists of 8%mol Yttria Stabilized Zirconia, $(Y_2O_3)_{0.08}(ZrO_2)_{0.92}$, and for simplicity is going to be called YSZ. The YSZ sheet was then fabricated by tape casting in Risø laboratories, with a final dimension of approximately $5 \times 5 \text{ cm}^2$. A portion of the sheet was taken for measuring the grain size, giving approximately $5.3 \pm 1.7 \text{ }\mu\text{m}$, by the same method as described in §4.2. The remaining portion of the sheet was taken for building the sample. At one side of the YSZ sheet, a layer of NiO/YSZ slurry was screen printed to make the electrode, using a DEK248 CERD screen printer. The slurry has a weight composition of 40.7% and 32.9% of Ni and YSZ respectively, while the rest of the components are solvent, binder, dispersant and additives. To dry the applied slurry, it was introduced in a Buch&Holm Memmert heating cabinet at $80 \text{ }^\circ\text{C}$ for 2 hours.

5.2.2 Sintering of electrodes and reducing NiO

After drying the printed slurry on the YSZ sheet, a layer of Pt paste was carefully applied by painting using a brush, until all the area was homogeneously covered. The sample was then left to dry in air for a few hours, followed by a sintering of the components using the program recommended by K. Brodersen (private communication, November 2017: Laboratory Coordinator at DTU, Department of Energy Conversion and Storage) and described below:

- $15 \text{ }^\circ\text{C}/\text{hour}$ from RT to $200 \text{ }^\circ\text{C}$ for 4 hours
- $15 \text{ }^\circ\text{C}/\text{hour}$ from $200 \text{ }^\circ\text{C}$ to $400 \text{ }^\circ\text{C}$ for 4 hours
- $15 \text{ }^\circ\text{C}/\text{hour}$ from $400 \text{ }^\circ\text{C}$ to $600 \text{ }^\circ\text{C}$ for 4 hours
- $60 \text{ }^\circ\text{C}/\text{hour}$ from $600 \text{ }^\circ\text{C}$ to $1300 \text{ }^\circ\text{C}$ for 4 hours
- Cooling down to RT at $100 \text{ }^\circ\text{C}/\text{hour}$

Once the components have been sintered, the next step is to reduce the NiO into Ni. The reduction was performed by heating the sample in a dry atmosphere composed by 5% H₂ in Argon for 2 hours at 850 °C. The reducing gas was supplied during all time, including heating and cooling.

5.2.3 Sample fabrication and mounting

The bulk sample was cut into smaller pieces using a diamond blade wheel (Minitom, Struers A/S). One piece with dimensions of approximately 4.75x0.23x0.25mm was selected, and Pt cables and Pt paste were applied as described in §4.2. The exposed length of the cell to the atmosphere is 2.25mm, from the edge of the alumina paste to the outer tip. The final cell was then mounted in an alumina rod having two separated holes drilled along the cylinder axis, allowing the Pt cables to run inside and ensuring required electrical insulation. The components of the cell and the different stages of the sample mounting in the alumina rod are illustrated in Figure 5.1.

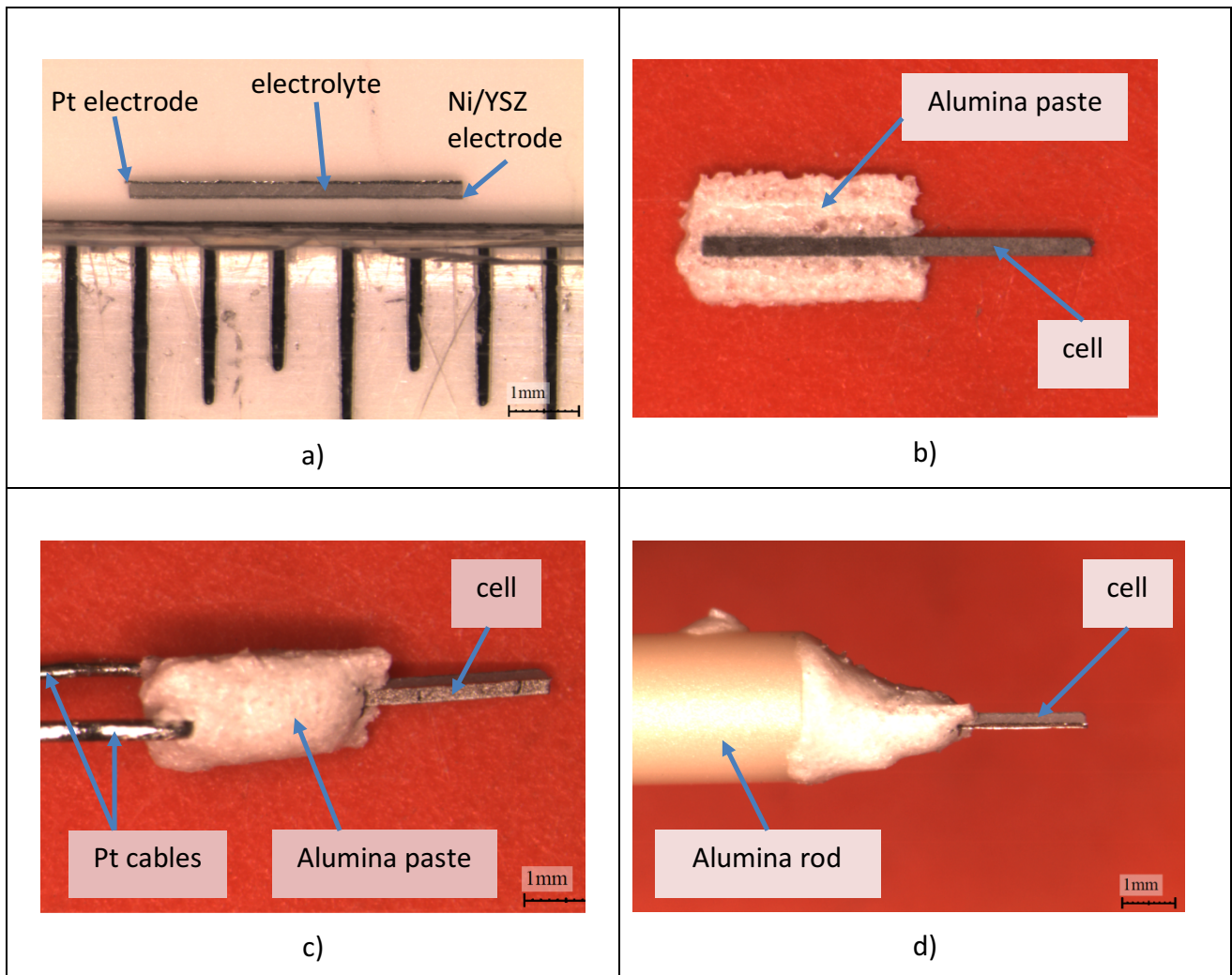


Figure 5.1. Stages of sample preparation. The cell is a YSZ electrolyte with Ni/YSZ and Pt electrodes. The elements of the cell and the interconnectors are glued together using alumina paste. a) electrodes and electrolyte, b) alumina paste applied to the sides of the cell to ensure proper electrical insulation when applying Pt paste. c) Pt cables mounted to the cell and glued with alumina paste d) final sample assembling on the alumina rod, before mounting the quartz tube.

5.2.4 Quartz tube

As in this experiment a gas environment needs to be provided at high temperature, quartz tube/capillary offers a good choice due to its outstanding properties. This is supported by the numerous *in-situ/in-operando* experiments carried out during many years involving X-rays, where some specific environmental conditions need to be controlled.

In our particular case, the quartz tube has to fulfil some properties, crucial for the achievement of the study. For example; the quartz tube needs to be as dense as possible to ensure gas tightness and simultaneously be relatively transparent to X-rays, especially at energies close to 17 keV (which is the order of energy used in this experiment). Moreover, it has to withstand typical SOCs operating temperatures (600 and 900 °C) and be resistant to reducing atmosphere, that in this case is 5%H₂ in N₂. Also, the thermal expansion has to be comparable to alumina paste, as both components are going to be glued together, although the glued sections are not expected to be at temperatures above 300 °C.

To comply with the geometry and setup in our experiment, closed end round quartz tubes with a total length of 50 mm, inner diameter of 5 mm and a wall thickness of 1 mm were provided by Lianyungang Liaison Quartz Co., Ltd. A sample tube was tested in-house at 1000 °C in a similar geometry as used later in the experiment. The absence of structural damage demonstrated its suitability.

The quartz tube was then chemically etched to reduce the wall thickness, in order to increase the transparency to X-rays. At energies close to 17 keV and a 1 mm wall thickness the X-ray attenuation is around 83.2%. The etching was carried out by submerging the tube in hydrofluoric acid, which is a suitable etchant to attack quartz at significant high etch rate (111) (112) (113) (114). The total attenuation of the quartz tube after the chemical etching was estimated to be around 37%, which is considerably better for improving the X-ray data. The attenuation was obtained by an X-ray attenuation/absorption calculator website (115).

5.2.5 Assembling the components

The sample and the quartz tube were then introduced separately in a glovebox made of nylon, provided by Sigma-Aldrich, and filled with wet 5%H₂ in N₂ gas environment taken directly from the Risø laboratory gas stream. To provide the wet environment, a bubbler between the gas supply and the glovebox was used. Then the quartz tube was glued to the base of the alumina rod using the alumina paste and dried at RT for a few hours inside the glovebox with the same gas environment. The final cell covered with the quartz tube in the alumina rod is shown in Figure 5.2.

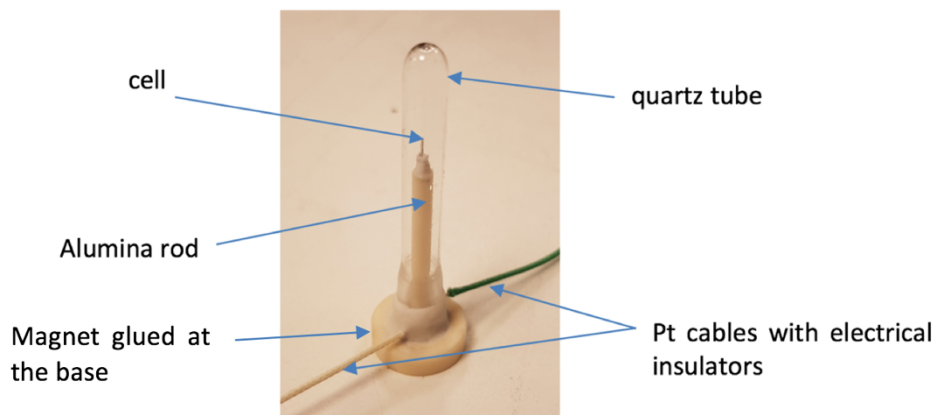


Figure 5.2. Assembly of the cell, quartz tube and alumina support. The cell is made by YSZ electrolyte and Ni/YSZ and Pt electrodes. The gas inside the chamber is a wet 5% H_2 in N_2 . A magnet was glued at the bottom; its purpose is explained later. Pt cables coming out the sample to the potentiostat, electrically insulated and color coded for polarization.

Standard *post-mortem* tomography was performed to the cell, using a Lab microCT Xradia Versa 420 (Carl Zeiss Inc), to reveal the different components of the cell and to confirm proper cable mounting, as shown in Figure 5.3. The energy of X-ray was 140 keV, with an exposure time of 1 second in 1601 projections and a pixel size of 16.84 μm , giving a field of view of 16.84 mm.

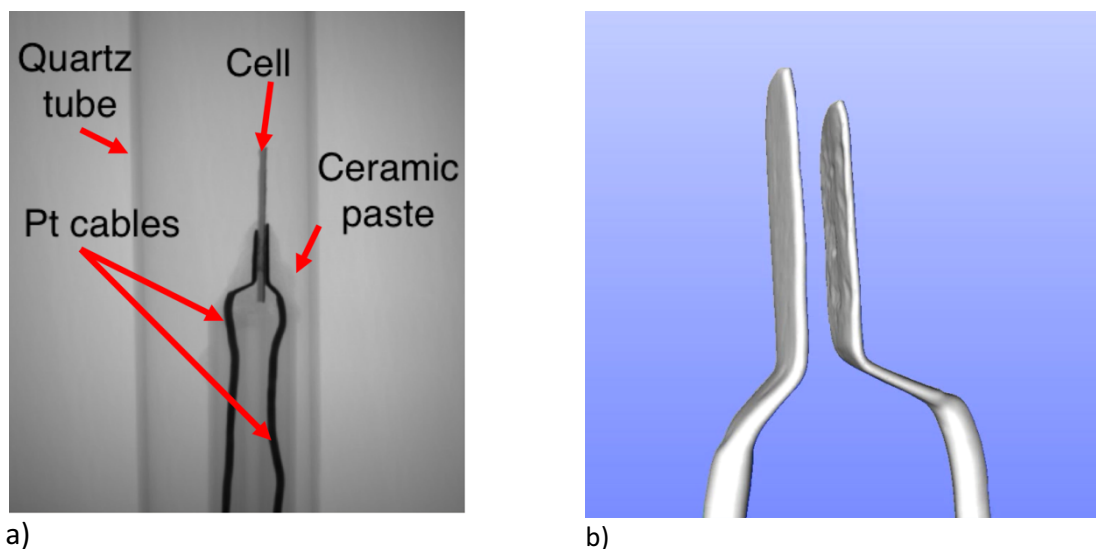


Figure 5.3. Monitoring the assembly of cell components. a) X-ray projection of the components of the sample, taken by a Lab microCT Xradia Versa 420 (Carl Zeiss Inc) with an energy of 140 keV. b) tomographic reconstruction, using AVIZO, of the area comprising the Pt cables on the electrodes. The image has been thresholded to visualize the correct mounting of Pt contacts.

5.3 Experimental setup

5.3.1 Sample stage

Before starting the experiment in a beamline, alignment of the sample is an essential step for proper data acquisition. In our experimental setup, the goniometer allows preliminary alignment; however, the final alignment of the sample with respect to the beam must be provided by other means. Normally, in many of the experiments in our beamline the sample is aligned by a special device, already available. Nevertheless, due to geometrical aspects of our sample, a new sample stage was necessary to be designed, capable of providing the required final alignment.

As the sample needs to be aligned by the new sample stage, our design was based on relative movements between these two parts. For that, a Neodymium nickel plated magnet, provided by Supermagnete, was fitted into an alumina ring and then glued at the bottom of the alumina rod (see Figure 5.2) of the sample holder. The purpose of the magnet is to provide enough grip of the sample holder against the vertical surface of the sample stage, without falling down, and

simultaneously allows the sample holder to slide smoothly on this surface. The layout of the sample stage designed for this experiment is shown in Figure 9.2.

As illustrated in Figure 5.4, the sample can be moved by 4 pairs of screws, one pair at each side of a square aluminium piece in a vertical position, directly attached to the goniometer. This system is analogous to a conventional XY stage, but the advantage of our design lies on the thinner dimensions between the goniometer and the base of the sample, which makes it more suitable. After an extensive search, no suitable conventional XY stage was found due to its thickness. The limitation of our design is that the translation by the pairs of screws is not as accurate as in a conventional XY stage, making the alignment process longer than the expected. A view of the sample stage, including the cell and alumina rod, is shown in Figure 5.4.

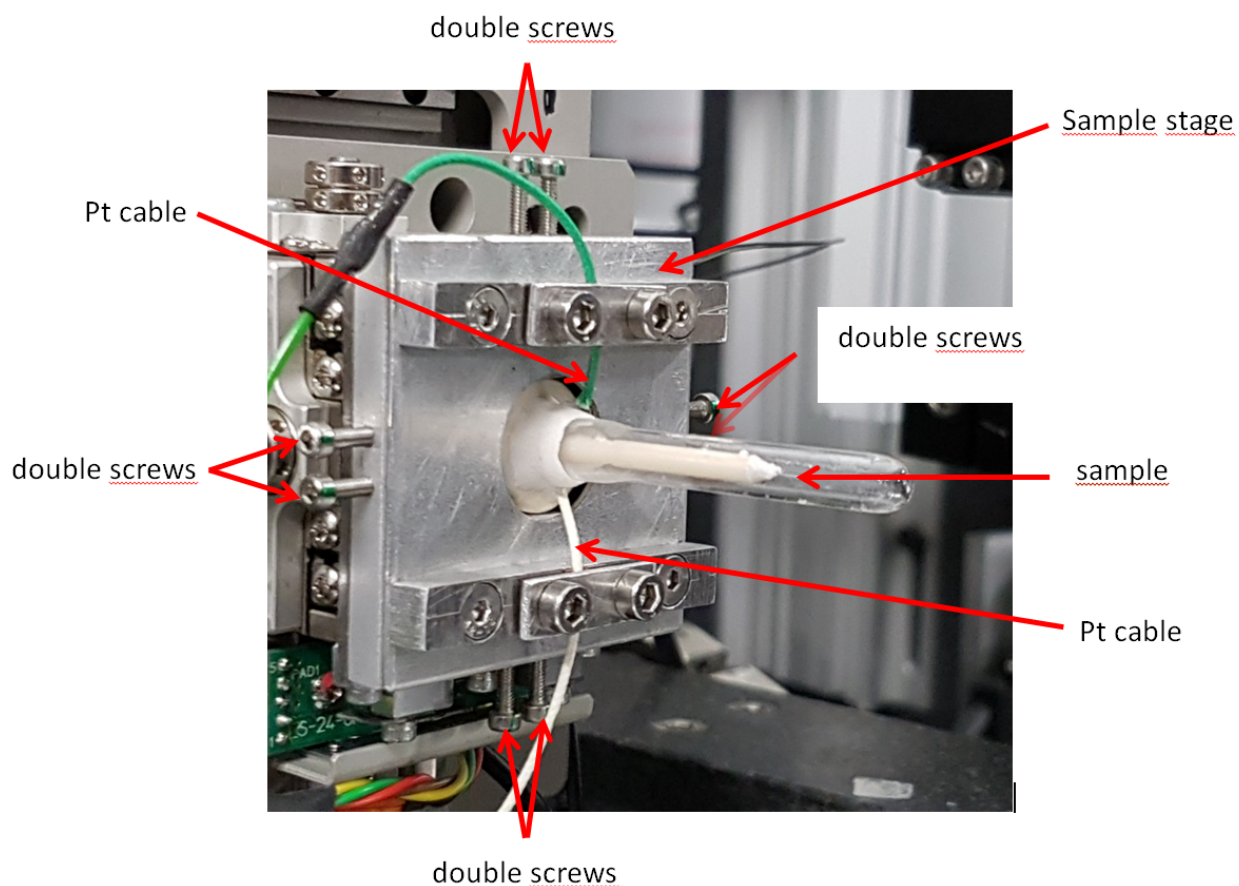


Figure 5.4. Image of the sample stage, sample holder, and cell mounted in the goniometer, just before experiment. The components are indicated by red arrows. The axis of rotation of the goniometer is horizontal. Moving the double screws at each side, the sample can be moved in the vertical plane of the sample stage, for proper alignment with the beam.

5.3.2 IR furnace

To provide high temperature a SpotIR model 4085 infrared heater was used, supplied from RESEARCH Inc. The heater is composed basically by a lamp (containing a tungsten filament), a reflector and an air cooling system. Its working principle is based on reflecting and focusing the infrared radiation emitted by the tungsten filament. To ensure maximum performance, the radiation is reflected by the aluminium wall, shaped internally as an ellipsoid. Hence, localized heat focuses only on the desired area without heating the rest of the product, where the filament is located in one of the the focal points of the ellipsoid and the target is placed in the other focal point.

The furnace contains a 750 Watt lamp with suitable stability, thus repeatable results can be achieved for consistent process outputs. Due to the energy dissipation while operating the furnace at relatively high temperatures, the lamp and the aluminium shielding are cooled by an air intake included in the furnace. The cooling air was taken from the air supply available in the beamline, allowing extended working periods with improved stability of several hours.

According to factory specifications, the maximum heated spot at the focal point is approximately 6 mm in diameter, which is large enough for heating homogeneously our cell. As the focal point where the sample is expected to be is inside the furnace, and this was not specifically designed for X-ray diffraction purposes, the necessity for a modification was required in order to allow the incoming beam impinging the sample and the diffracted beam pass through the furnace towards the detector. For that, two holes were drilled in the Al wall of the furnace at opposite sides, along the beam-sample-diffraction axis. The smaller hole allows the incoming beam illuminating the cell and the bigger hole allows the diffracted beam to reach the detectors. The diameter of the smaller hole was approximately 5 mm, enough for the full incoming beam, while the diameter of the bigger hole was estimated on the diameter of the expected ring patterns of the sample and the sample-detector distance. The two holes were then covered by a thin aluminium foil to prevent heat escaping outside the chamber. By factory design, the furnace has a hole of approximately 16

mm in diameter as the entry of the sample. The size of the entry hole is suitable for the quartz tube, allowing alignment and optimization of the sample position to maximize the temperature.

During the experiment the lamp was controlled by an external power supply, available in the beamline. The maximum temperature achieved in early testing was near 1000 °C, demonstrating the capabilities of this furnace for SOCs experiments.

Since the temperature of the sample cannot be measured at the sample position during in-operando experiment due to limitations by the setup, the temperature was measured indirectly by calibration as follows: before placing the sample in the goniometer, a thermocouple with a diameter of 1 mm and a working temperature range up to 1000 °C was aligned with respect to the incoming beam. In order to align the focal point of the IR furnace to the sample and the beam, the IR furnace was moved in all directions and was fixed at the position where the temperature is maximum for a given power delivery of the furnace. A calibration curve was made based on the temperature readings by the thermocouple and the power delivery.

5.3.3 Beamline configuration

An image of the beamline configuration closest to the sample is illustrated in Figure 5.5. In this view, the incoming beam comes from left to right, passing through the aluminium foil covering the hole of the furnace, hits the sample and the diffracting beam passes through the bigger hole, in a conical shape towards the detectors. The photo was taken during operando conditions, as the sample can be seen glowing inside the heating chamber. The surroundings of the goniometer were air cooled to prevent misalignment by thermal expansion, as this is the most sensitive device close to the sample.

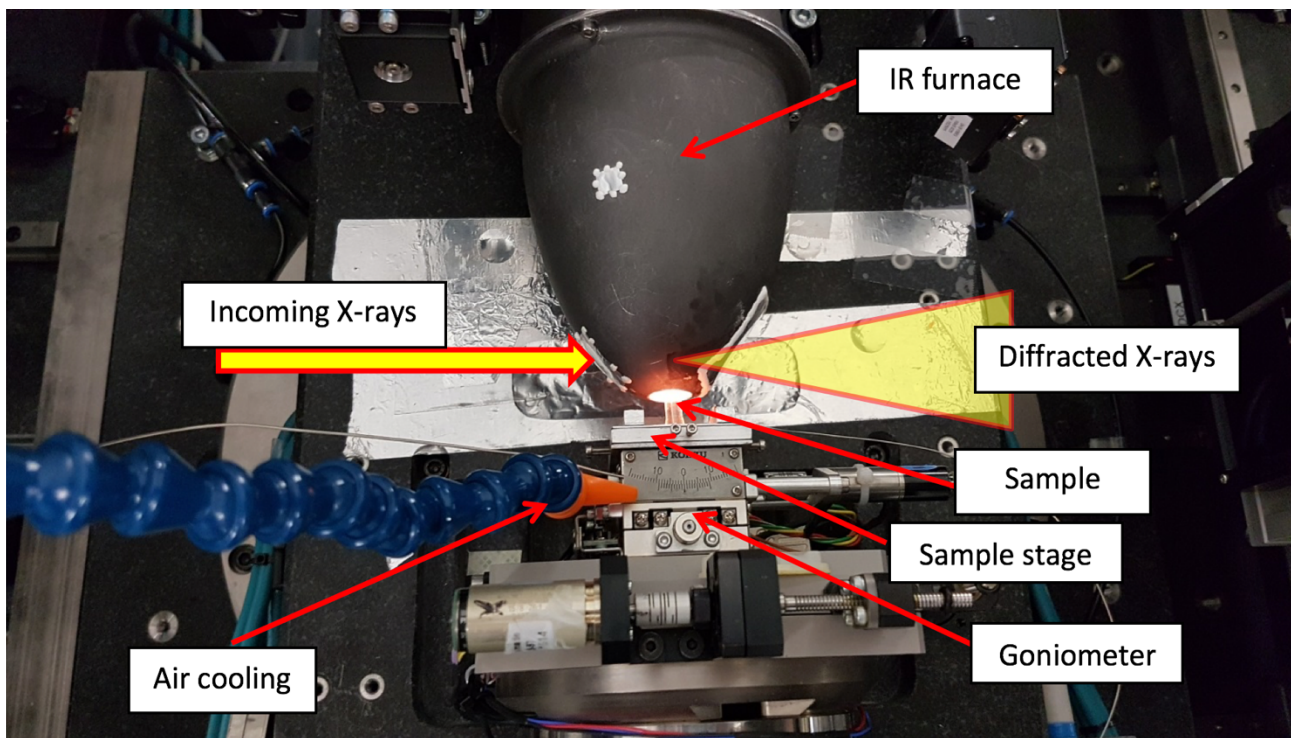


Figure 5.5. Top view of the beamline setup close to the cell during experiment. The Near Field, DC and Far Field detectors are not shown. The cell is at few millimeters inside the IR furnace and at high temperature. The left hole drilled in the aluminium shield of the furnace allows the entrance of the beam (from the left) and the right hole allows the diffraction cones coming out towards the detectors.

In this experiment a diffraction camera detector, referred here as DC, was used to capture the diffracted rings from the cell. The DC is basically a FreLon camera with a scintillator screen coupled to a CCD chip, with a pixel size of $47.5 \mu\text{m}$ and a screen resolution of 2048×2048 pixels, hence a field of view of approximately $100 \times 100 \text{ mm}^2$. The DC was positioned at a distance of 137 mm from the sample, resulting in an angular resolution of 0.02° in the beam axis. The setup for performing X-ray microscopy (strain and mosaicity mapping) remains the same as described in Chapter 4.

The energy of the incoming synchrotron beam was 16.8 keV. This energy provides a suitable balance between amount of diffracting rings and high flux, as the latter is maximized close to this energy. Moreover, the X-ray absorption K edges of Y and Zr are 17.04 keV and 17.99 keV respectively; therefore, at 16.8 keV no X-ray absorption is expected, improving thus the diffraction

image quality at equivalent exposure time. The incoming beam was narrowed by a set of silicon lenses placed before the sample, with a resulting FWHM of 11.7 μm in “z” direction (see Figure 3.5) to allow scanning as a function of the position across the cell, as described in more detail later.

5.4 Experimental procedure

After temperature calibration, the sample was mounted as observed in Figure 5.5, including electrical connections to apply the polarization. The temperature was raised to 650 $^{\circ}\text{C}$ relatively slowly to avoid thermal expansion issues. The sample was positioned such as the planes of the electrodes were in parallel to the direction of the beam. By scanning the line beam at 19 different positions across the cell close to the region where the interconnectors are, full ring X-ray diffraction patterns were collected from the Ni/YSZ electrode to the middle of the YSZ electrolyte (the position across the cell is also called “layer” and as “scan number”). The first 10 scans, starting from the Ni/YSZ electrode, have a step size of 4.5 μm , the next scan has 10 μm and the rest of the scans have 12.85 μm , comprising a total distance of 145 μm . This is shown in the Figure 5.6.

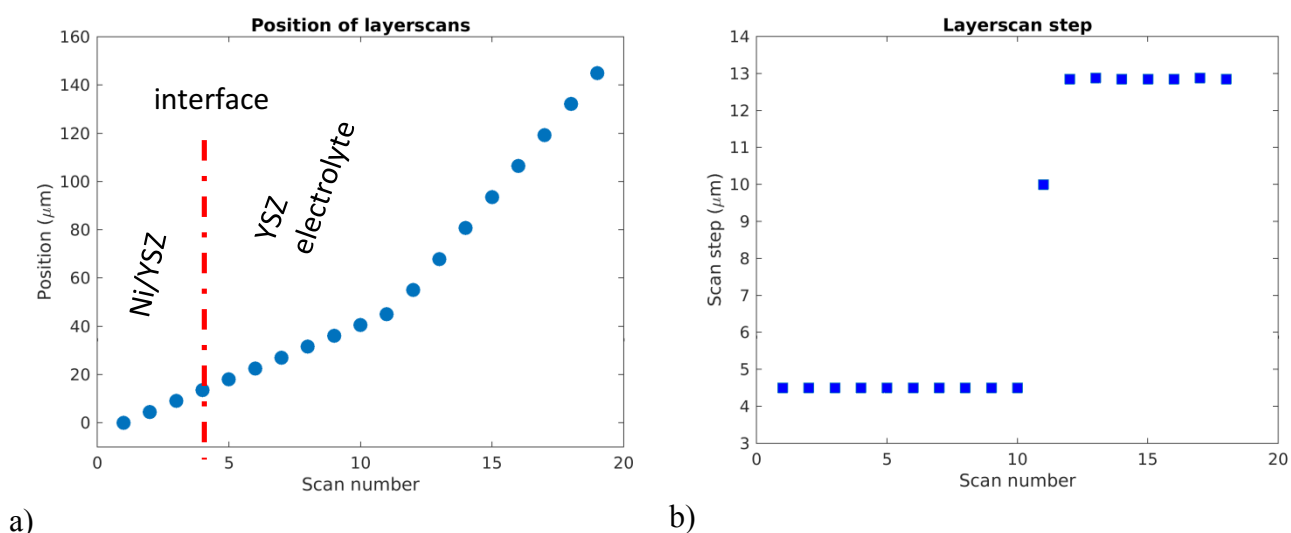


Figure 5.6. a) Position of the scan number (layer) relative to the real position (in μm) across the cell. The first position is at the Ni/YSZ electrode, where layer 1 corresponds to zero position. The red dot-dashed line indicates the estimated interface position. b) Relation between the scan step (in μm) to the scan number (layer).

The DC camera was placed such that the direct beam is not centered respect to the image. Using this off-center configuration allows detecting more diffraction lines at one side of the detector, although on the other side less rings are visible. However, this is coherent to our goals on detecting new phases, by detecting as many rings as possible. Each diffraction pattern is taken from a single shot of the beam. Exposure time was selected experimentally to avoid saturation of peaks coming from the biggest diffracting grains. Saturated peaks can result in wrong estimation of peaks position when integrating the diffraction lines; therefore, no saturated peaks are desirable.

As a part of the capabilities using the objective lens, a mosaicity map was performed alternately on a YSZ(111) grain found in the electrolyte, close to the electrode/electrolyte interface. Mosaicity scan consists of rocking angles in ω and in χ (see Figure 3.5) of the sample while keeping the Far Field detector fixed. The angle ω was tilted 0.06° in 13 steps and χ was tilted 0.4° in 11 steps. Since ω is directly related to 2θ , we report here the mosaicity in 2θ and χ ; this is a 2D mosaicity.

Electrochemical impedance spectroscopy was performed during the experiment, once the operating temperature was reached. Since in our case it is uncertain at what polarization a significant degradation occurs, the polarization was applied from 0 to -1.8V in steps of 0.2V during suitable time at each step so that the electrochemical parameters and XRD information can be monitored during the experiment. The negative sign corresponds to the negative potential applied to the Ni/YSZ electrode, while positive potential was applied to the Pt electrode. The range of scanned frequencies was from 1MHz to 0.02 Hz, with 12 points per decade in logarithmic spacing scale. Each point of the plot was averaged a maximum of 4 times with an applied voltage for EIS (over the DC applied voltage) was 15 mV. The cables were connected as recommended by K. K. Hansen (private communication, December 2017: Senior Researcher at DTU, Department of Energy Conversion and Storage) and P. Norby (private communication, December 2017: Professor at DTU, Department of Energy Conversion and Storage). Here is necessary to clarified that the above described parameters used in EIS were chosen by an agreement from experienced scientist in this topic in our department, K. V. Hansen (private communication, November 2018: Project Coordinator at DTU, Department of Energy Conversion and Storage) and T. Jacobsen (private communication, November 2018: Lecturer at DTU, Chemistry Department) in combination with

the electrochemical evolution of the cell during the experiment. Thus, by varying the minimum frequency and the number of average point, time for each measurement change and in this case lies between 11 to 23 minutes in a total of 158 cycles during approximately 35 hours of EIS measurement. EIS measurements started approximately 2 hours after the first full ring X-ray diffraction scan, thus the reference time for all the measurements shown in later sections is the initial time of the full ring X-ray diffraction.

Notably, a delamination/breaking of the Ni/YSZ electrode was observed after several hours at operating conditions. Consequently, the temperature was decreased slowly to room temperature and the polarization was released after the complete cooling.

In Figure 5.7 the plot of the times corresponding to each EIS is shown:

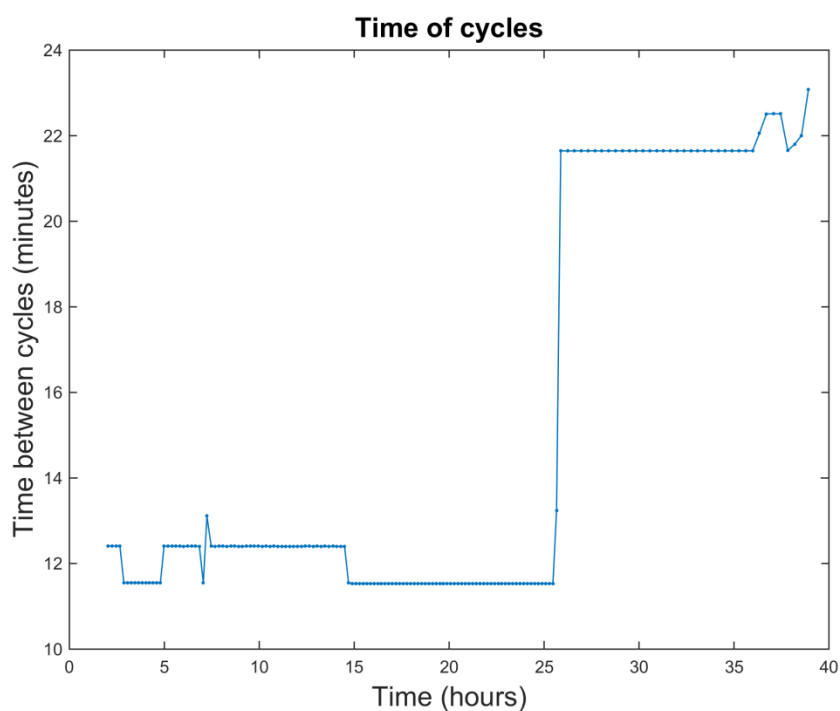


Figure 5.7. Time corresponding to the EIS cycles. A total of 158 EIS cycles during 37 hours was measured. The onset of 2 hours between the initial EIS spectrum and the first full ring X-ray diffraction scan is shown at the left side of the plot as the blank region.

Finally, a *post-mortem* SEM/EDS was carried out in the Zeiss Merlin (FEGSEM) electron microscope coupled to a Bruker Quantax spectrometer. The energy of the electron beam for standard SEM was 15 keV and for EDS was 10 keV.

5.4.1 Data analysis

To analyze the full ring XRD data, MatLAB and FIT2D were used. The latter software has been developed at the ESRF and is useful to perform preliminary X-ray diffraction data processing, which includes an internal database of common standards (116). A LaB_6 standard was used as a reference to determine the center of the diffraction rings and to calibrate the sample-detector distance. The image was also cropped to remove pixels at the edges due to distortion correction, which cannot be computed in X-ray analysis. The center position coordinates, sample-detector distance and crop parameters were applied equally to the diffraction data of the investigated cell. In Figure 5.8 an example of LaB_6 diffraction image is shown. The image has been corrected for distortion correction and cropped.

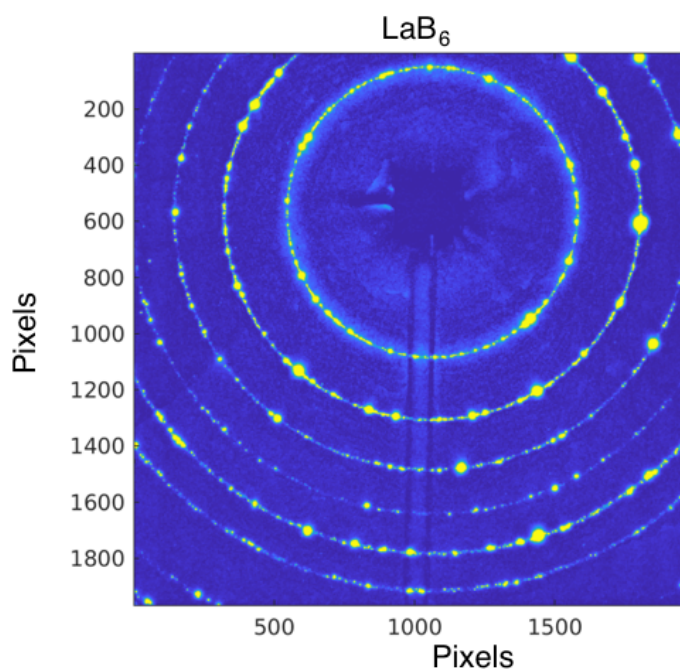


Figure 5.8. Diffraction pattern of LaB_6 after correcting for distortion and cropping. The X-ray energy is 16.8 keV, the sample-detector distance is 137 mm and the image resolution is 2048x2048 pixels with a pixel size of 47.5 μm . The off-centered position of the DC camera allows comprising more diffraction lines, as seen from the sections of rings at the bottom corners of the image. Yellow and blue colors indicate high and low intensities respectively.

The procedure performed to the LaB₆ image was applied to the diffraction images of the cell. The integration of the intensities in azimuthal angle was done considering the pixel intensity, pixel size and sample-detector distance, to finally the diffraction profile: Integrated intensity vs 2θ . The phases corresponding to the expected materials used to fabricate the cell were identified by using the well-known Inorganic Crystal Structure Database (ICSD) (117). The centers of the peak positions were estimated taking into account the thermal expansion coefficient for each phase (46) (118) and compared to the experimental position of the peaks. The width in 2θ of the peaks corresponding to the different phases: YSZ, Ni and NiO were selected visually, considering a negligible intensity at the base of the peaks.

In order to obtain the 2D mosaicity image, each pixel represent the integrated intensity of the complete image were the grain is (or not, depending on the ω and χ). For a specific χ the grain is tilted in a range of ω , giving a line in the mosaicity image with the integrated intensity of those images recorded from tilting in ω . Thus, an MxN image means that there are M and N steps of ω and χ . The range and steps of ω and χ is chosen experimentally, since it depends on the microstructural characteristics of the material. Normally, the images at the lowest and higher values of ω and χ do not contain the grain as it is not illuminated in Bragg condition, and the center values contain approximately the largest value of the intensity of the grain, which is approximately in the middle range of the Bragg condition.

To analyze the EIS data, a software called Elcheamea Analytical, which has been developed by S. Koch, C. Graves and K. V. Hansen, was used. This software allows loading the EIS data and to define the desired equivalent circuit model to fit the data. As the original EIS output data is in a format compatible only to the software provided by the EIS potentiostat, the data was changed to the compatible format for Elcheamea Analytical using MatLab. In addition, due to the length and shape of the cables from the cell to the EIS potentiostat, some previous filtering was applied in order to remove noise and more importantly frequency instabilities from induction effects of the cables. Thus, high frequencies in the range from 1 MHz to 10 kHz were removed, according to T. Jacobsen (private communication, January 2018) and K. V. Hansen (private communication, November 2018: Project Coordinator at DTU, Department of Energy Conversion and Storage).

According to the characteristics of the EIS spectra, they were fitted to single and double RQ circuit connected in series to an inductor L and a resistance R.

5.5 Results and discussion

5.5.1 *Post-mortem* EDS

A *post-mortem* SEM micrograph of the polished cross-section of the cell is shown in Figure 5.9. The components of the cell are marked in red arrows. During the polishing, the exposed region of the sample was completely removed by accident. This frustrates the attempt to get morphological information and elemental composition at this side of the cell. The red ellipse indicates the region where the remaining part of the cell was expected to be.

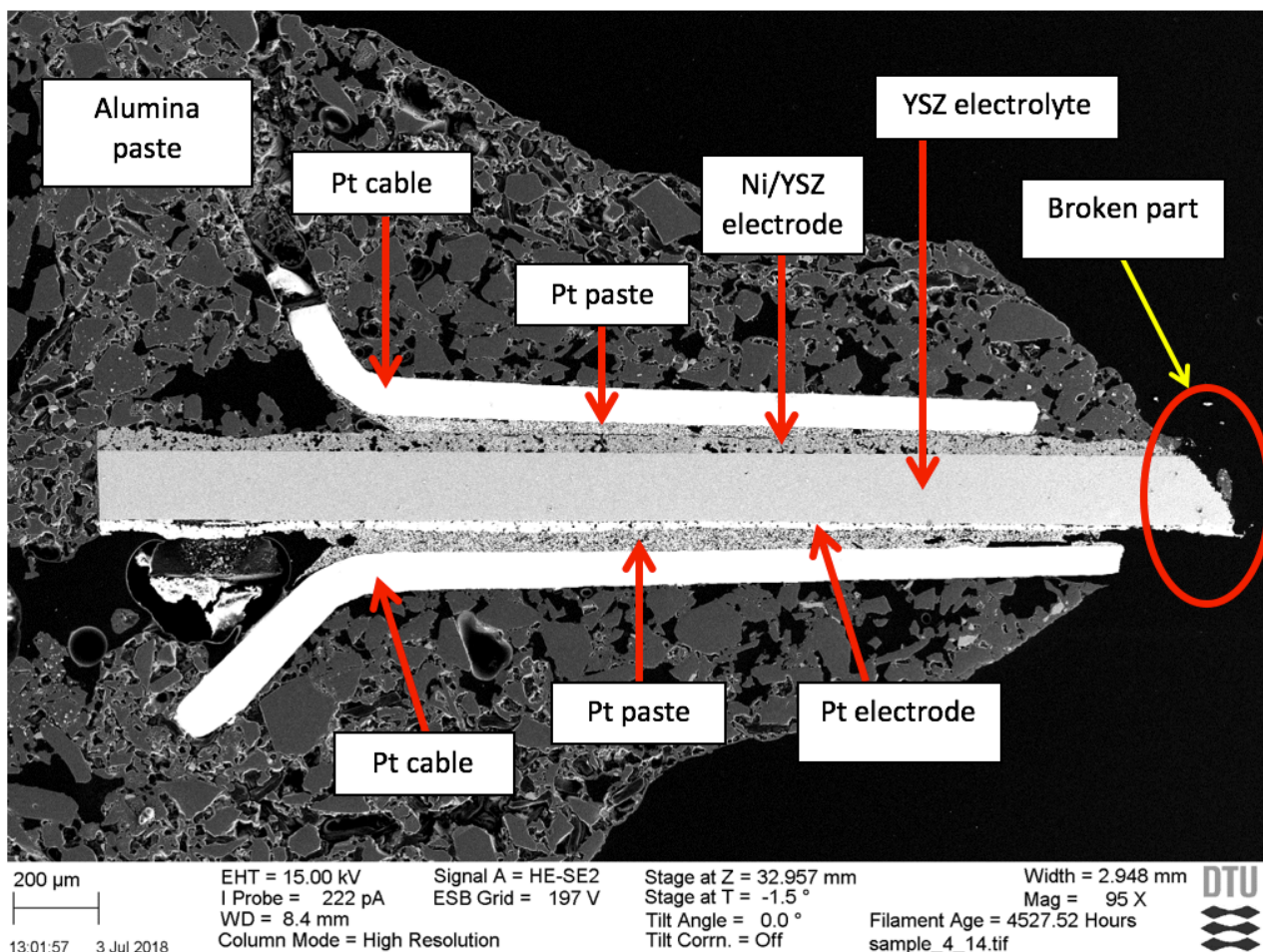
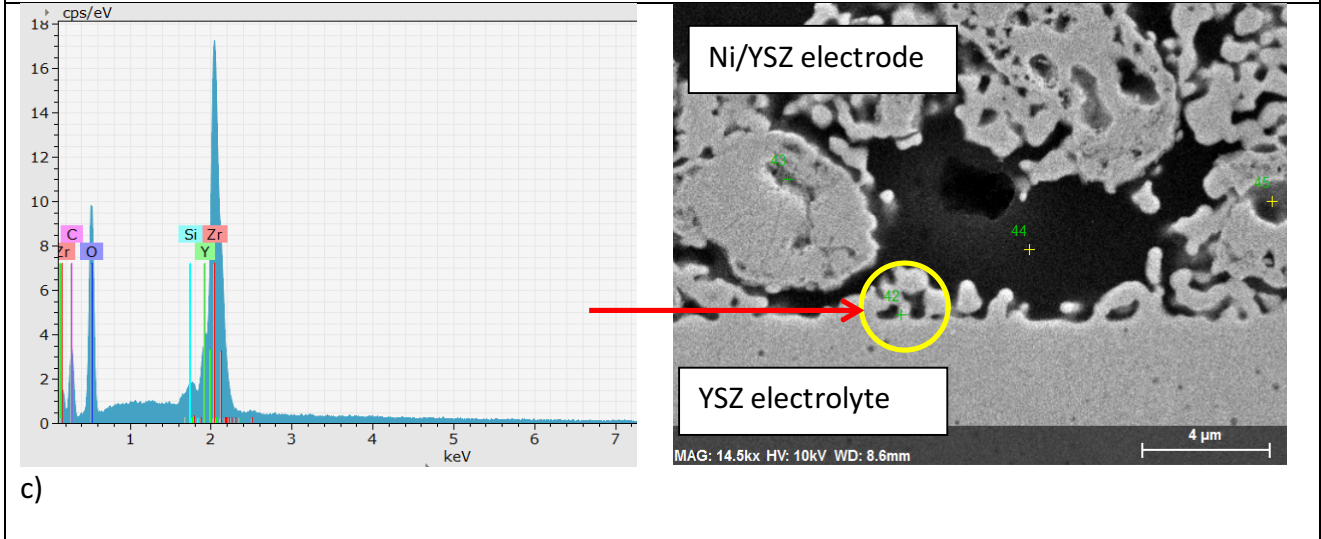
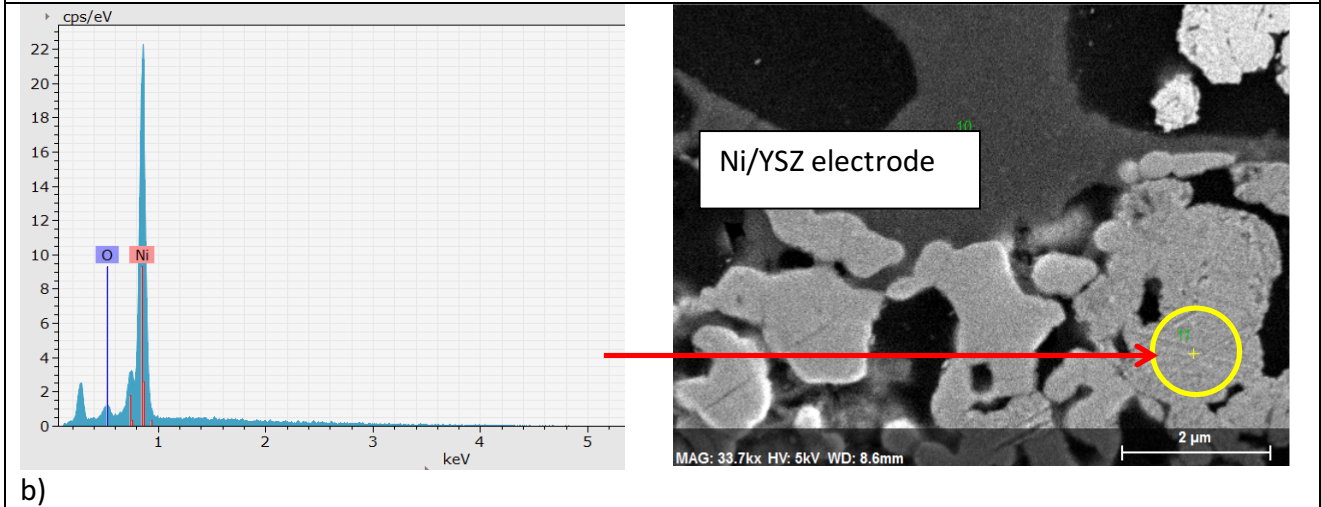
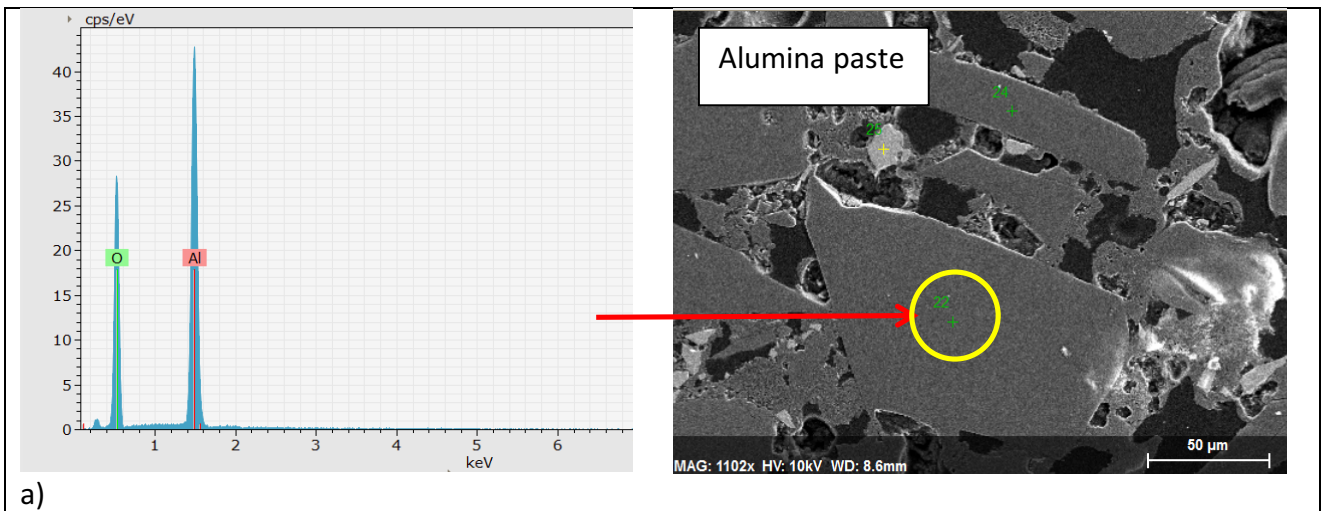


Figure 5.9. *Post-mortem* SEM micrograph of the cross-section of the cell. The image was taken with an electron beam energy of 15 keV and the horizontal width of the image is 2.948 mm. The components of the cell, with the interconnectors and alumina paste are indicated by red arrows. The broken part of the cell (due to polishing) is indicated by the red ellipse.

The EDS was carried out on selected areas close to the Ni/YSZ - YSZ electrolyte interface, the Pt paste/cables and alumina paste. The results of the elemental composition (left) with their corresponding regions (right) are illustrated in Figure 5.10.



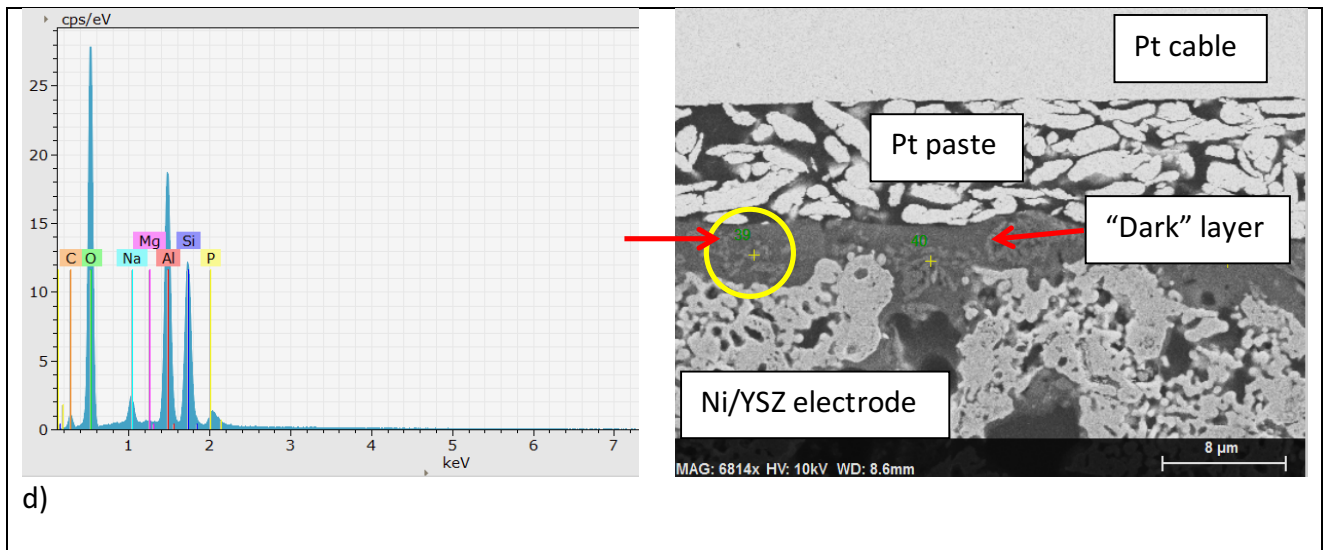


Figure 5.10. *Post-mortem* EDS at an energy of 10 keV in selected regions; a) alumina paste, b) Ni grain of the Ni/YSZ electrode, c) Ni/YSZ – electrolyte interface and d) “dark” layer between the Ni/YSZ electrode and Pt paste. The centers of the yellow circles indicate the point EDS. The sample was carbon coated to prevent drifting of the images. The energy scale is shorter than 10 keV for a better visualization of the images.

In Figure 5.10 a) the EDS was performed in a big alumina grain belonging to the alumina paste, where the presence of aluminium and oxygen forming the Al_2O_3 is confirmed, with no evidence of other elements. In b) a Ni particle was found, with a very little presence of oxygen.

In c) the EDS was done close to the Ni/YSZ – YSZ electrolyte interface. The characteristic lines of Zr and Y are shown, although they are almost overlapped. Also, a small amount of Si was found. Silicon is commonly present as an impurity in YSZ providers and Silica have been reported to segregate at this interface during electrolysis testing (109) (110). However, the presence of this impurity in the electrode is more likely to come from the alumina paste rather than the small amounts reported by the ceramic providers.

In d) the EDS was performed in an unexpected “dark” layer between the Pt paste and the Ni/YSZ electrode. Other elements were also found in this region, such as Na, Mg, Si, P and Al. The relatively high peak of the Al suggests that Na, Mg, Si and P may be coming from the aluminium paste as impurities remaining after the drying process. Moreover, the relative higher peak of O,

when compared to the O and Al counts in the alumina grain shown in a), may indicate that some of the observed impurities (Na, Mg, Si and P) could be in the form of oxides.

5.5.2 Evolution of current

The total impedance spectra acquired during the experiment was 158. However, in further sections the spectra and related parameters were plotted in the first 154 cycles, as the last 4 cycles the points in the spectra were extremely dispersed, so the resistances were not possible to be obtained.

The evolution of the current and the corresponding voltage during the experiment are illustrated in Figure 5.11.

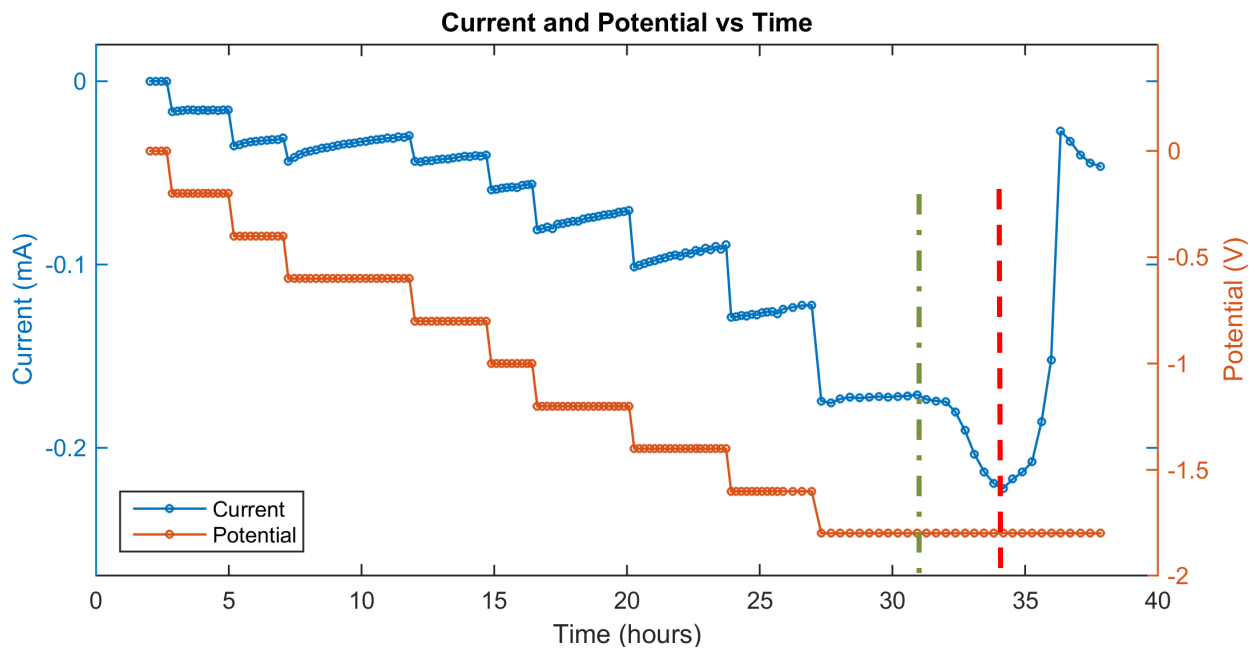


Figure 5.11. Evolution of current at different polarizations. The current and polarizations are plotted in blue and red line-dots respectively. The scales of the current and polarization are at left and right respectively. The polarization was applied up to -1.8V in steps of 0.2V. The dashed-dot green line represents the time when the anomalous behavior started (unexpected increase of current) and the dashed red line represents the time at which the delamination between the Ni/YSZ and the electrolyte is supposed to occur.

From Figure 5.11 it can be seen that the current changes correspondingly to the voltage step. The highest current density occurs in the case at the highest polarization, being approximately 0.016 A/cm^2 during the first 4-5 hours at -1.8V . Also, within the same voltage, the current decreases slightly with negligible changes at -0.2 and in the first 4 hours at -1.8V . After 4 hours at -1.8V an inconsistent and significant increase of the current was observed, reaching a maximum of -0.22 mA at 34 hours. Due to this unexpected behavior, it was decided to look the exposed region of the cell by a direct image. After examination of the cell, a partial delamination/breaking between the Ni/YSZ and the electrolyte was found close to the tip. Therefore, a basic tomography was performed at the region of interest, and it is shown in Figure 5.12.

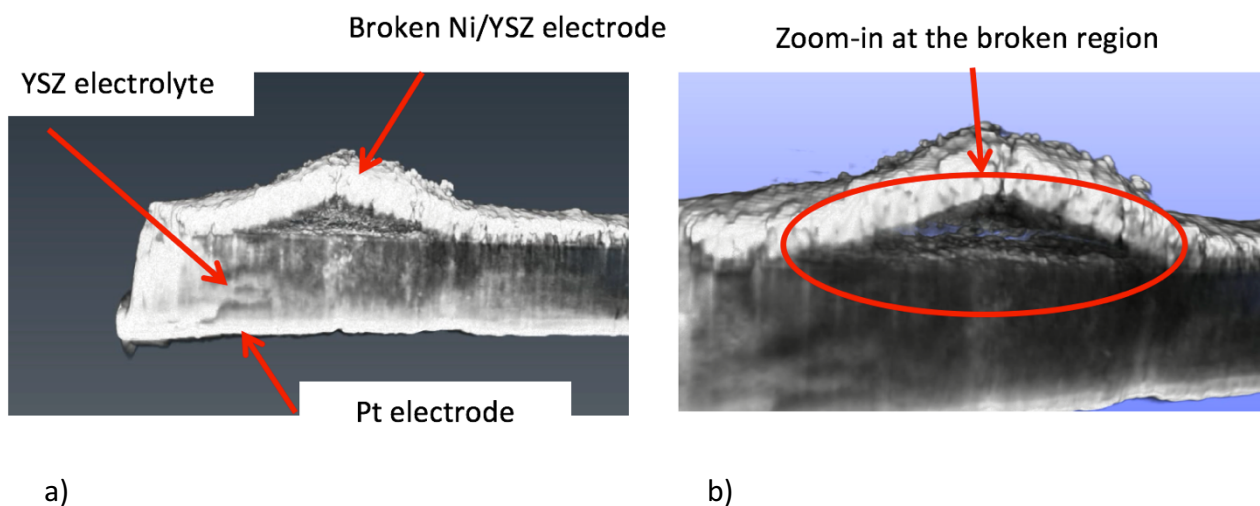


Figure 5.12. a) 3D reconstruction of tomography performed during experiment, close to the tip of the cell (exposed region). The tomography comprises the Ni/YSZ electrode, YSZ electrolyte and the Pt electrode. b) Zoom-in at the broken region.

In Figure 5.11, no current change is expected to occur at 0V , and no significant change is observed at -0.2V . From -0.4V to -1.6V a more pronounced change of the current is observed. In order to represent this change, the current starting in the fourth EIS cycle to the end at each voltage of EIS cycle were taken and linearly fitted. The slopes of the fitting are shown in Figure 5.13, in which the width of the bars correspond to the time interval at each voltage. At -1.8V , the current was taken from the 4th to the 11th EIS cycle, as after that cycle the current shows the unexpected behavior

described previously. The first three EIS cycles at each voltage were discarded due to instabilities of the current.

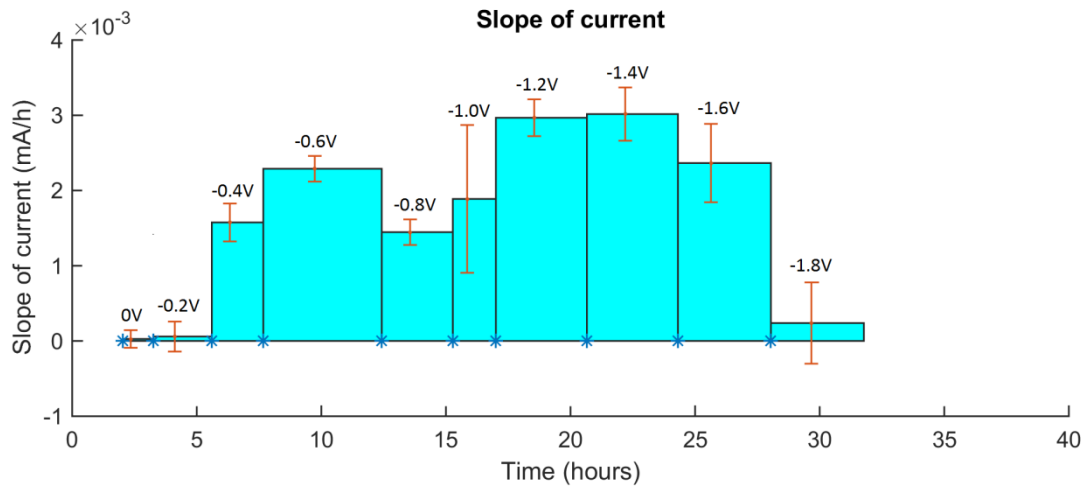


Figure 5.13. Slope of the current at each voltage step. The slope is obtained by linear fitting of the currents during the fixed polarization, from the plot in Figure 5.11 with sign inverted. The error bar is given by the fitting parameters in MatLAB. The values of polarization are at the top of the slope values.

In Figure 5.13 a significant increase of the degradation, in terms of the current, is observed for polarization between -0.4 and -1.6V, while very small degradation are seen for 0V, -0.2 and -1.8V. It is expected that for higher polarization, the current degradation increases; however, this is observed in the intervals from -0.2 to -0.6V and from -0.8 to -1.4V, while unexpected behaviors were observed from -0.6 to -0.8V and from -1.4 to -1.8V. The smaller degradation at -1.8V does not explain the rapid increase of the current after 32 hours.

5.5.3 Evolution of R_s and R_p

In Figure 5.14, EIS spectra corresponding to the last EIS cycle for each polarization are shown.

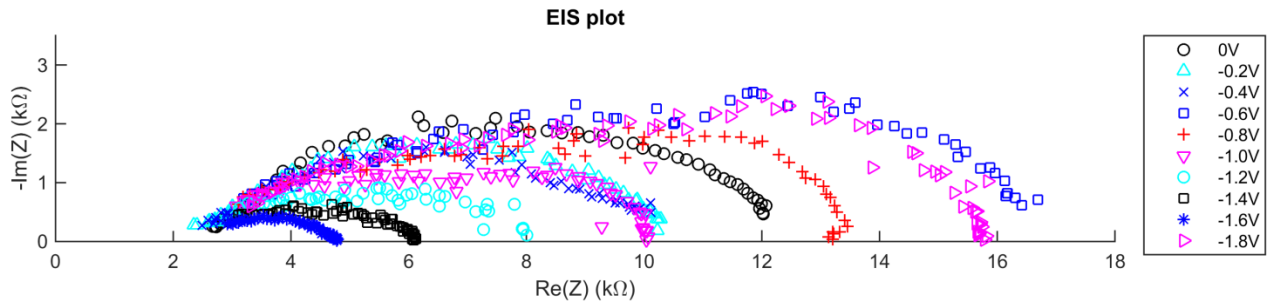


Figure 5.14. Impedance spectra corresponding to the last measurement at each polarization. The impedance spectra were obtained by a Biologic SP-200. The high frequency of the spectra has been thresholded to 10 kHz to remove inductance effects from cabling; the minimum frequency is 0.02 Hz. Note that the dominant changes are from the R_p , while variation of R_s are significantly smaller. The aspect ratio between the $-\text{Im}(Z)$ and $\text{Re}(Z)$ is 1:1. The legend at the right indicates the colors corresponding to the polarizations.

After removing the high frequencies due to inductance effects of the cabling, as described in §5.4.1, it was necessary to filter again the profiles in order to remove remaining scattered points. The R_p and R_s were obtained from the fitting and their evolution for each cycle are shown in Figure 5.15.

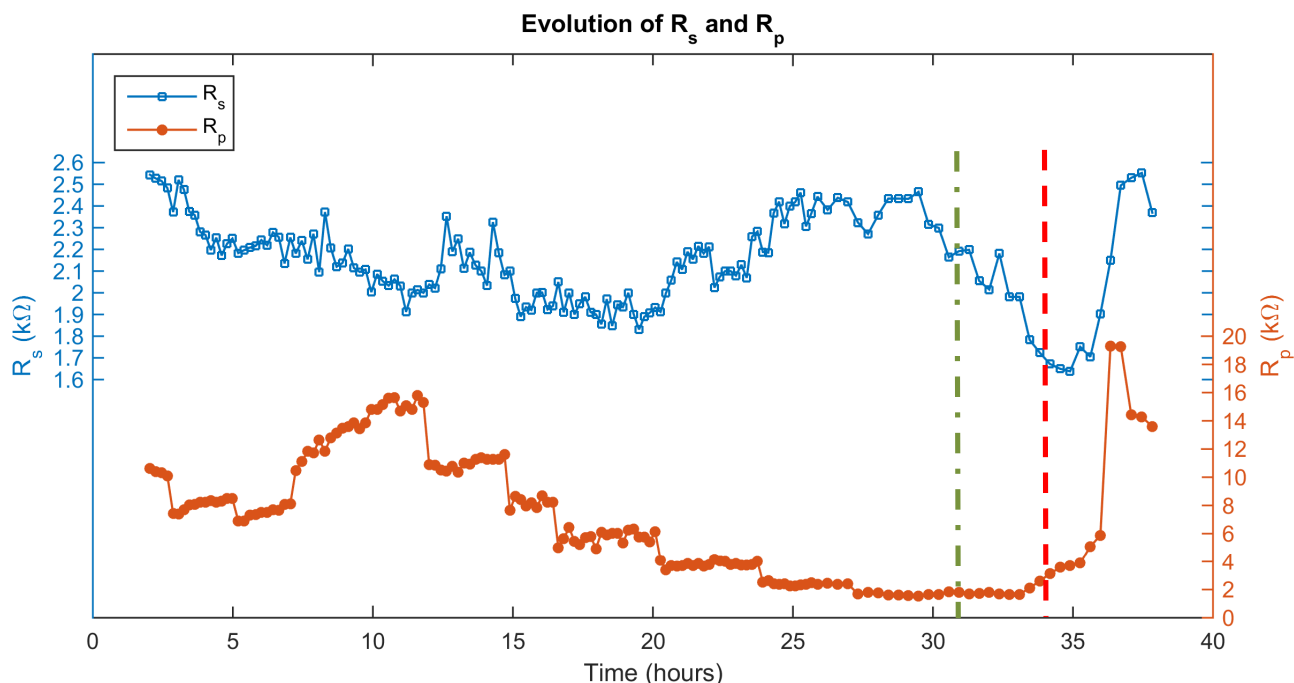


Figure 5.15. Evolution of R_s (blue square-line) and R_p (red circle-line) obtained from the impedance spectra. Vertical dashed-dot green line and the dash red line represent the same times as described in Figure 5.11. Scale of R_s and R_p are at the left and right respectively.

As can be seen in Figure 5.15, the R_s fluctuates in the range between 2000 and 2600 Ω , representing $\pm 13\%$ during the first 29 hours. Moreover, the evolution of R_s (plotted as the blue squares connected by blue line) does not show a clear relation to the current.

From 29 to 35 hours, R_s shows a slightly more pronounced decrease of around 0.34 times in a shorter time interval than previous changes. At 35 hours the R_s increases continuously much faster than before until the end of the EIS cycles.

The evolution of R_p shows a different behavior than R_s . In Figure 5.15 it is clearly seen the steps in R_p corresponding to the steps in the applied voltage, with also an expected inverse relation between R_p and the current. Moreover, taken into consideration the characteristics of the EIS spectra, the relations observed for the applied voltage, the current and the R_p are indicators that the cell worked properly as an electrochemical device. This constitutes a great step forward towards the development of new cell designs with the aim of studying these systems in synchrotron facilities. Differences in scaling of R_s and R_p of the cell used in this experiment

compared to resistances in standard cells can be attributed to the geometry, characteristics of the materials and fabrication process.

5.5.4 Interface position

Before introducing the next results, it is necessary to clarify that the times of EIS cycles are not equal to the times of the cycles related to the diffraction measurements, Therefore, the term “diffraction cycle” is used from now on, referring to the cycles corresponding to the diffraction measurement.

In order to know the position of the interface as a function of the layer number, the integrated intensity of the two Ni peaks (111) and (200) averaged over the cycles (time) were plotted, as illustrated in Figure 5.16.

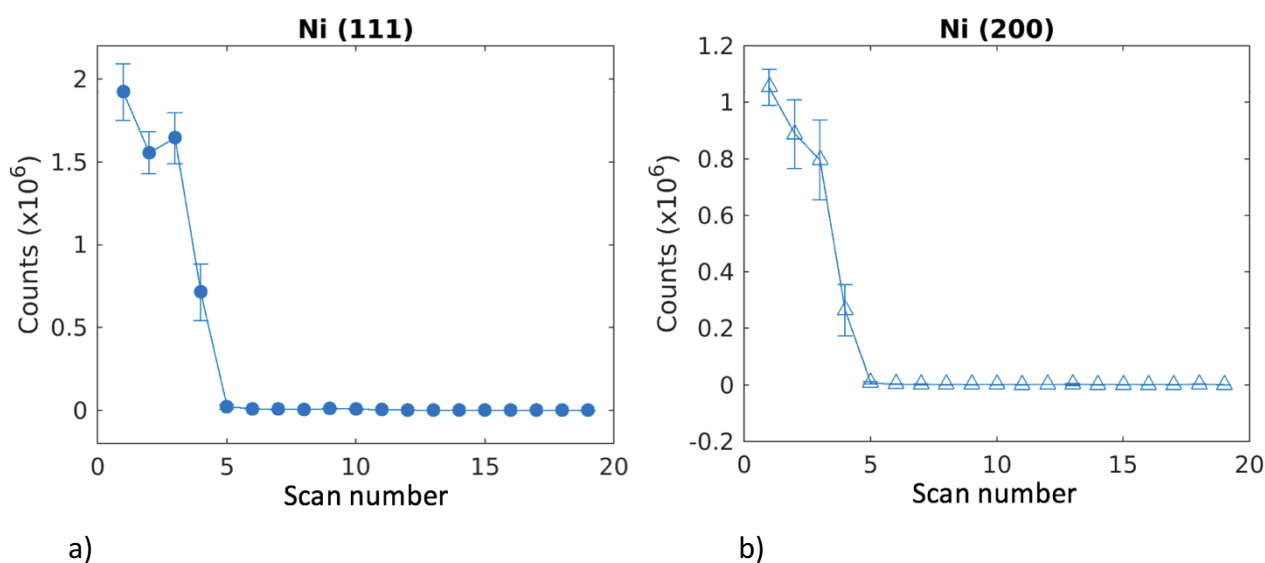


Figure 5.16. Integrated intensities of the Ni peaks, a) Ni(111) and b) Ni(200), corresponding to the position of the layers (scan number). The integrated intensities were averaged over the diffraction cycles and the error bars are from the standard deviation of the averaging. The plots show that the Ni/YSZ – electrolyte interface is somewhere between layer 3 and 5, i.e. close to layer 4.

As can be seen in Figure 5.16, the three first layers for both Ni peaks are the most intense in comparison to the others, indicating that at these positions the beam was illuminating only the Ni/YSZ electrode. In the next scan, at layer 4 the average integrated intensity decreased by approximately the half, indicating that the beam was illuminating approximately equally both sides of the electrode/electrolyte interface, with the center of the beam located very close to the interface plane. Thus, is valid to assume that from layer 1 to 3 the beam is located completely in the Ni/YSZ electrode and at layer 5 the beam is entirely in the YSZ electrolyte, as practically no Ni phase was detected at this layer. Irregularities of average integrated intensities for the first three layers in both Ni peaks cases can be attributed to statistical fluctuations of the intensities from different diffracting peaks due to the different positions of the layer.

In order to evaluate the stability of the sample with respect to the beam during the experiment, a reference artifact of the sample was monitored. The feature of the sample appears as a shadow in the DC image, which was found to be moving accordingly to the position of the sample at each scan number. Therefore, its position was defined by the inflection point between the integrated intensities from the bright and dark regions around the shadow. This is shown in Figure 5.17. The image to the left is the original DC image, the center image is a cropped section from the original image, comprising the “edge” of the shadow (horizontal red line) and the right image shows the inflection point, which is then considered for stability. From the center image, the intensity is integrated in “X” direction and the profile is fitted to a 3rd degree polynomial, where the inflection point is taken as the position of the “edge” of the shadow. This procedure was done for all DC cycles at all scan numbers.

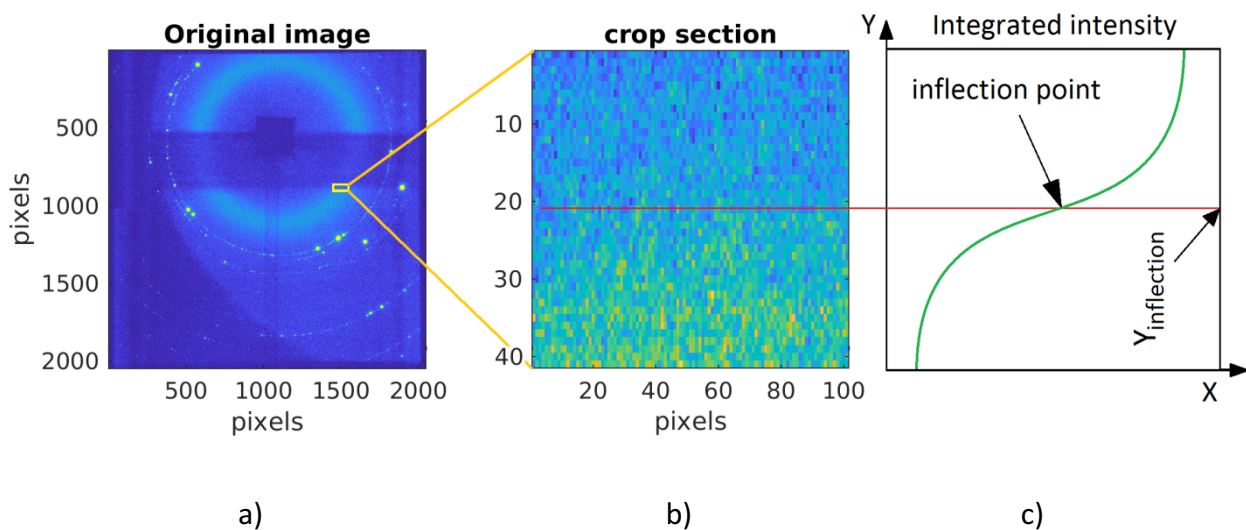


Figure 5.17. Evaluation of the stability of the sample with respect to the beam, by monitoring the position of a shadow projected into the DC from the sample. The shadow was moving according to the movement of the sample. a) Original DC image and selected region with the shadow, b) zoom-in of the region with the shadow and c) schematic of the polynomial fitting (3rd order) of the integrated intensity of the shadow in the specified direction.

The position of these “edges” were averaged for each cycle and normalized with reference to the first scan number. The Figure 5.18 shows the plot of the positions of the “edges” to the scan number. This plot is very similar to the plot in Figure 5.6 a), as expected. The correlation between the pixels and the real distance in the image is approximately 1.7 pixel = 1 μm .

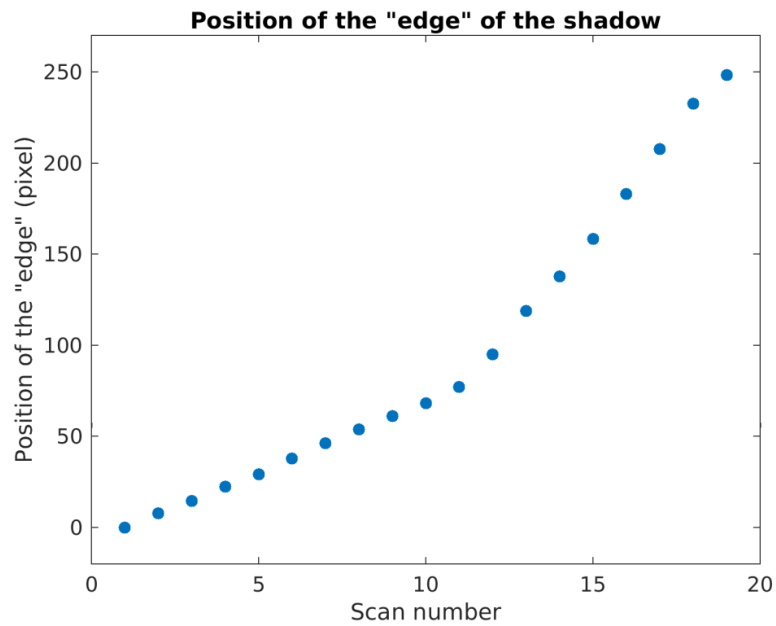
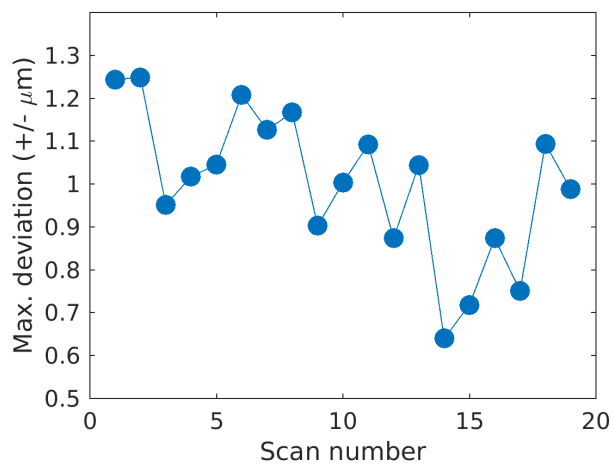
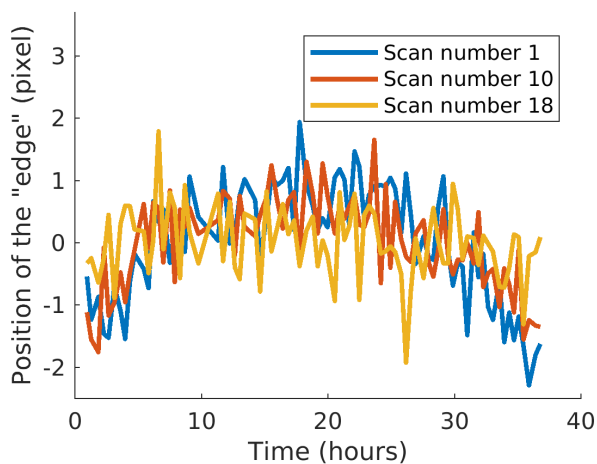


Figure 5.18. Correspondence between the position of the “edge” of the shadow (in pixels) to the scan number. The position of the shadow is calculated by a 3rd order polynomial fitting from the integrated intensities of the bright and dark regions of the shadow (see Figure 5.17).

An example of the evolution of the “edge” position in selected scan numbers (1, 10 and 18) is shown in Figure 5.19 a). In Figure 5.19 b) the difference between the maximum and the minimum position of the “edge”, over time, for each scan number is plotted.



a)

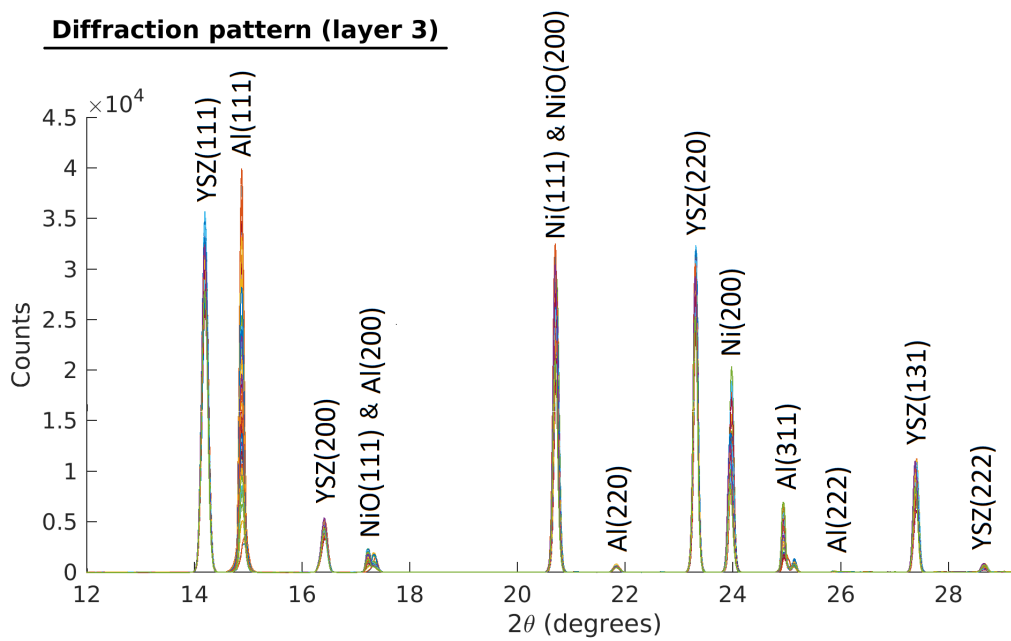
b)

Figure 5.19. a) Position of the “edge” of the shadow (in pixels) as a function of time during experiment, for selected scan numbers: 1, 10 and 18, and b) the maximum deviation (in $\pm \mu\text{m}$) of the position of the “edge” for each scan number. The latter shows that the position of the sample with respect to the beam remains relatively stable, within a margin of $\pm 1.25 \mu\text{m}$.

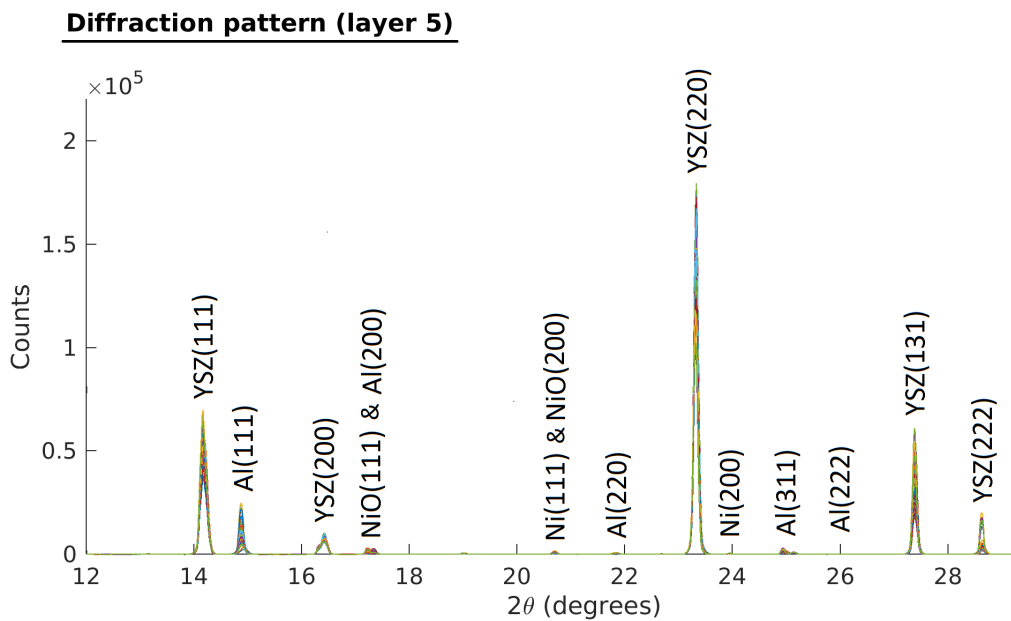
As an example, in Figure 5.19 a) the position of the “edge” for the first scan number (blue line) fluctuates in a range of approximately ± 2 pixels. This corresponds to a fluctuation in real distance of $\pm 1.25 \mu\text{m}$, which is shown in b), corresponding to the first scan number. Notably, the maximum deviation of the sample during the experiment is in the order of $\pm 1.25 \mu\text{m}$, suggesting a stability of the sample position suitable for our experiment.

5.5.5 Phases in XRD

In Figure 5.20 the diffraction patterns for the scan numbers at each side (layer 3 and 5) of the electrode/electrolyte interface, with the corresponding Miller index for each known phase are shown.



a)



b)

Figure 5.20. Diffraction patterns collected at the closest scan numbers of each side of the Ni/YSZ – electrolyte interface. i.e. a) scan number 3 and b) scan number 5. The diffraction patterns were obtained by azimuthal integration of the DC images. The different colors in the profiles are due to the overlapping of all the diffraction patterns as a function of time. The Miller indexes are shown on top of the corresponding phases.

As can be seen in Figure 5.20 a) and b) Al phase was found. The presence of Al can be explained by the Al foil placed in the holes of the IR lamp. The positions of the peaks of the Al, shown in Figure 5.20, do not correspond to the real positions they should have in a standard diffractogram if the distance to the DC is the same as the sample; however, these peaks match when correcting for the position of the Al foil in the hole opened for diffraction respect to the DC detector. According to our estimation, the Al foil is approximately 25 mm from the sample. i.e. 112 mm from the DC. The estimation was based on the measurements of lengths from a top view of the IR furnace, as shown in Figure 9.4, in the Appendix. No peaks were detected when correcting for the position of the front Al foil, probably due to the blocking effect of the quartz tube covering the sample and the diameter of the back hole. Differences of relative intensities of Al found in the experiment in comparison to that found in the ICSD database can be explained by the possible high texture of the Al foil during its fabrication process in addition to the statistics of the illuminated Al grain at only one single 2θ angle, as the IR furnace was never moved during the experiment.

In order to corroborate the validity of the peak indexing, new peak positions of YSZ, Ni and NiO corrected for thermal expansion were calculated for comparison to the experimental peak positions. The new theoretical positions were estimated considering their lattice structure and lattice parameter at 650 °C or TEC in the range from RT to 650 °C. Table 5.1 shows the lattice parameters and TEC at RT and at 650 °C, and their respective TEC of the known phases present in our cell.

Phase	Lattice parameter (nm) T = room temperature	Lattice parameter (nm) T = 650 °C	TEC (from RT to 650 °C) ($\times 10^{-6} \text{ k}^{-1}$)
YSZ ⁽¹⁾	0.5143	0.5175	10.0
Ni ⁽²⁾	0.3524	0.3558	15.4
NiO ⁽³⁾	0.41767	0.42125	13.7

- (1) – Lattice parameter of YSZ at RT was taken from Lamas et al. (56). Lattice parameter at 650 °C was estimated based on TEC given by Hayashi et al. (46).
- (2) – Lattice parameter of Ni at 650 °C was estimated by a second order polynomial fitting of data from Suh et al. (118). TEC was calculated from the lattice parameter variation.
- (3) – Lattice parameter of NiO at 650 °C was estimated by a second order polynomial fitting of data from a report found in ICSD database (119). TEC was calculated from the lattice parameter variation and corroborated by Mori et al. (47).

Table 5.1. Lattice parameters and TEC of YSZ, Ni and NiO at RT and T = 650 °C.

The calculated theoretical positions were then compared to the peak positions of our diffraction profiles corresponding to layer 3, as this layer contains the three main phases present in the studied region of the cell. Table 5.2 shows the difference between the theoretical position of each peak of YSZ, Ni and NiO and the experimental peak positions obtained by XRD. The experimental peak positions were obtained by averaging the center position of the peaks estimated by Gaussian fitting before applying polarization.

Phase	Miller index	Difference between theoretical and experimental peak positions ($\times 10^{-3}$ degree)
YSZ	(111)	9.3
	(200)	15.4
	(220)	40.9
	(131)	47.4
	(222)	67.3
Ni	(111)	22.9
	(200)	26.3
NiO	(111)	129.6
	(200)	539.9

Table 5.2. Difference between the expected peak positions (estimated after correcting for the thermal expansion) and the experimental position from XRD for YSZ, Ni and NiO at layer 3.

In general, the peaks of YSZ and Ni phases can be considered as acceptable with the expected positions when correcting for the thermal expansion in layer 3.

The differences between the theoretical and experimental peak positions of YSZ and Ni can be attributed to the following factors:

- small discrepancy of TEC and/or lattice parameter reported in the literature (47) (120).
- effect of porosity on the TEC (121) (122) (123) (124).
- Asymmetry of the peaks: in our experiment the peaks do not have necessarily a perfect symmetrical profile, as it depends on the distribution of intensities from individual spots. As in our case the XRD images were collected with the sample fixed at a single 2θ , the distribution does not necessarily have a symmetrical shape.

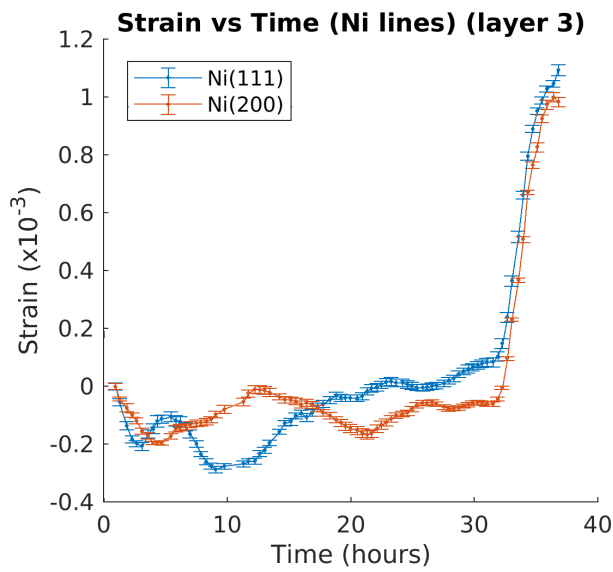
In the case of NiO(111) and NiO(200), the higher difference in comparison to that on YSZ and Ni, can be attributed to overlapping peaks. Coincidentally, the NiO(111) and NiO(200) are overlapped by Al(200) and Ni(111) at approximately 17.3° and 20.7° respectively, as seen in Figure 5.20.

No other phases, in addition to those already known, were detected by XRD. Here we propose the following alternatives to justify the non-detection of expected phases:

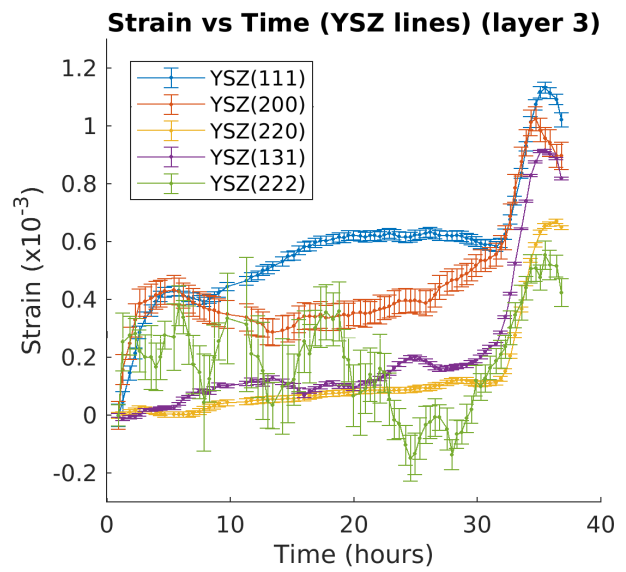
- actually no phases were formed during experiment.
- concentrations of phases are not high enough to be detectable.
- inspected region: phases could form in areas outside the area examined experimentally.
- image processing: background and noise removal performed in the image processing can influence the final diffraction profile, potentially hiding the phases.
- DC field of view: phases cannot be detected if their diffraction lines are outside the field of view defined by the DC setup.

5.5.6 Strain in Ni and YSZ close to the electrode/electrolyte interface

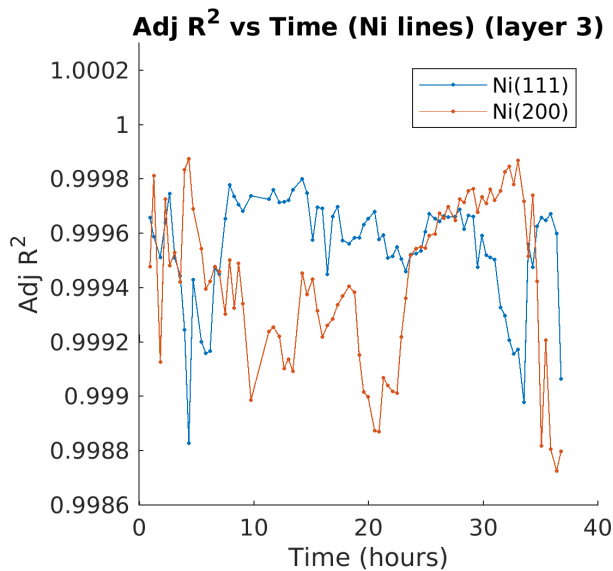
In Figure 5.21, the strain evolution of the Ni and YSZ phases at layer 3 are illustrated. The strain was calculated as the difference between the d-spacing of each peak at the selected time and the corresponding initial d-spacing. The peaks were fitted to a Gaussian curve and their corresponding Adj. R² are plotted below the corresponding strain evolution. The error bars in the strain plotting were obtained by the error propagation of the strain equation, based on the error given by the peak position. The latter and the Adj. R² were obtained during fitting in MatLAB. Notably, negative and positive strain indicates contraction and expansion of the lattice, respectively.



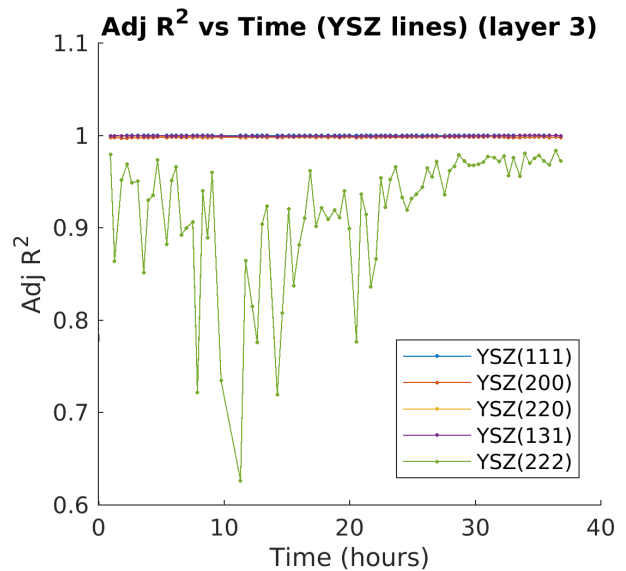
a)



b)



c)



d)

Figure 5.21. Strain evolution, from the shift of the center of the indexed Ni and YSZ peaks, at scan number 3 (Ni/YSZ electrode) of a) Ni peaks and b) YSZ peaks. c) and d) are the corresponding Adj. R² of Ni and YSZ peaks respectively. Note the increase of tensile strain in Ni and YSZ after 32 hours.

As can be seen in Figure 5.21 at scan number 3, the strain for the Ni phases behaves considerably stable in the first 32 hours, with fluctuations in the range between 0.1 and -0.3x10⁻³ and 0 and -0.2x10⁻³ for Ni(111) and Ni(200) respectively. After 32 hours at operating conditions, there is a significant expansion of the lattice, indicated by the large increase of strain in the positive region,

reaching maximum strain close to 1×10^{-3} at 37 hours. This level of strain is usually considered as relatively high.

In Figure 5.21 b) there is a more complex behavior of the strains for each YSZ line. The strain in YSZ(220) and YSZ(131) show a very stable behavior up to 32 hours, with a slight increase of the tensile range up to 0.2×10^{-3} within this time. The strain in YSZ(111) and (200) show a larger increase in tensile strain up to 0.4×10^{-3} in the first 5 hours and up to 0.6×10^{-3} at 32 hours. In the case of the YSZ(222), the erratic behavior is probably due to the relatively low intensity of the peaks, which results in a poor fitting, as shown in Figure 5.21 d).

In Figure 5.22 the strain evolution of the peaks of YSZ phase in layer 5 is shown, with the corresponding Adj. R^2 of the fitting.

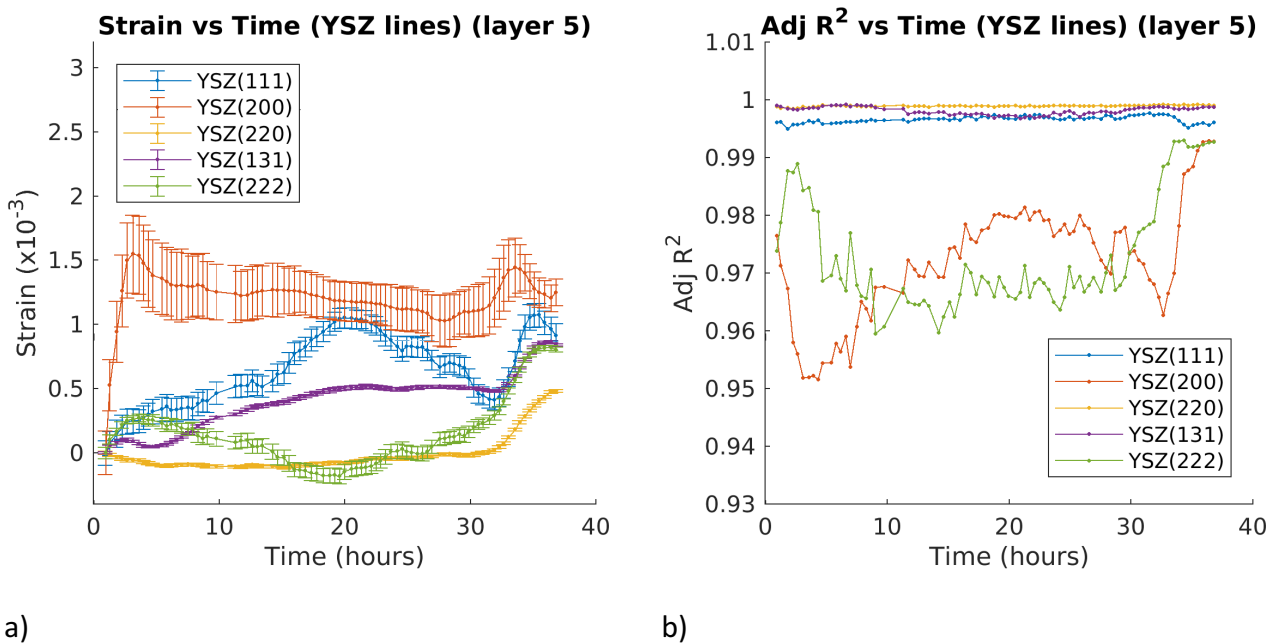


Figure 5.22. a) Strain evolution, from the shift of the center of the YSZ electrolyte indexed peaks, at scan number 5 of YSZ and b) the corresponding Adj. R^2 .

As can be seen in Figure 5.22, there is no consistent behavior of the strains in the YSZ. The strain of YSZ(200) increases rapidly up to 1.5×10^{-3} in the first 2-3 hours, stabilizing during the next 30 hours. In the case of YSZ(111) the tensile strain increases during the first 20 hours, followed by a decrease up to 32 hours. An opposite behavior is observed for YSZ(222). The behavior of the strain

in YSZ(220) and YSZ(131) are more consistent between them, although a slight increase can be seen in the latter.

In all cases, there is a significant increase of the strain after 32 hours, which appears to be related to the delamination observed at the Ni/YSZ – electrolyte interface. Moreover, the estimation of the center of the peaks, from which the strain is calculated, can be improved by tilting the sample in a small 2θ , improving the statistics of diffracting spots, thus the diffraction profile. Tilting the sample could be analogous to collect a more crystalline diffraction pattern.

5.5.7 Mosaicity

In Figure 5.23 two examples of a 2D mosaicity image are shown at approximately 3 and 37 hours at operating conditions. Here, ω is analogous to 2θ , as it defines the Bragg position. Therefore, the mosaicity image is given in 2θ vs χ in degrees.

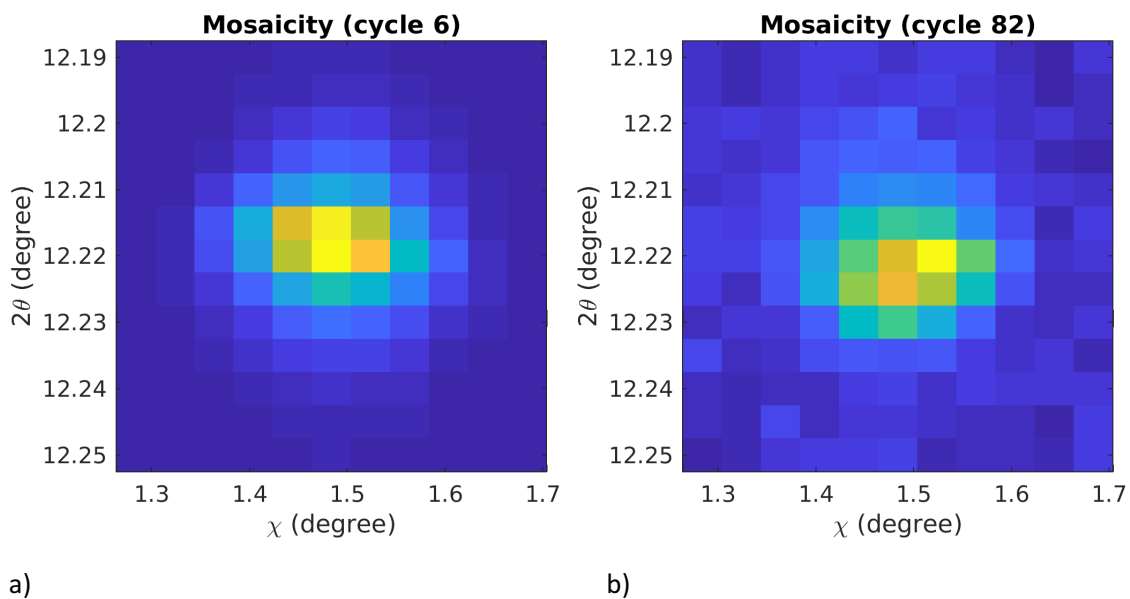


Figure 5.23. Example of 2D mosaicity maps at a) diffraction cycle 6 and b) diffraction cycle 82, corresponding to times at 3 and 37 hours respectively. Each pixel in the mosaicity map corresponds to the integrated intensity of the X-ray microscopy image at the specific 2θ and χ position. Yellow and blue colors indicate high and low intensity respectively.

To quantify for all the images at different times, each image is integrated in horizontal and vertical axis, giving an approximate Gaussian curve for 2θ and χ , in which the FWHM can be calculated. The FWHM evolutions of 2θ and χ , are shown in Figure 5.24.

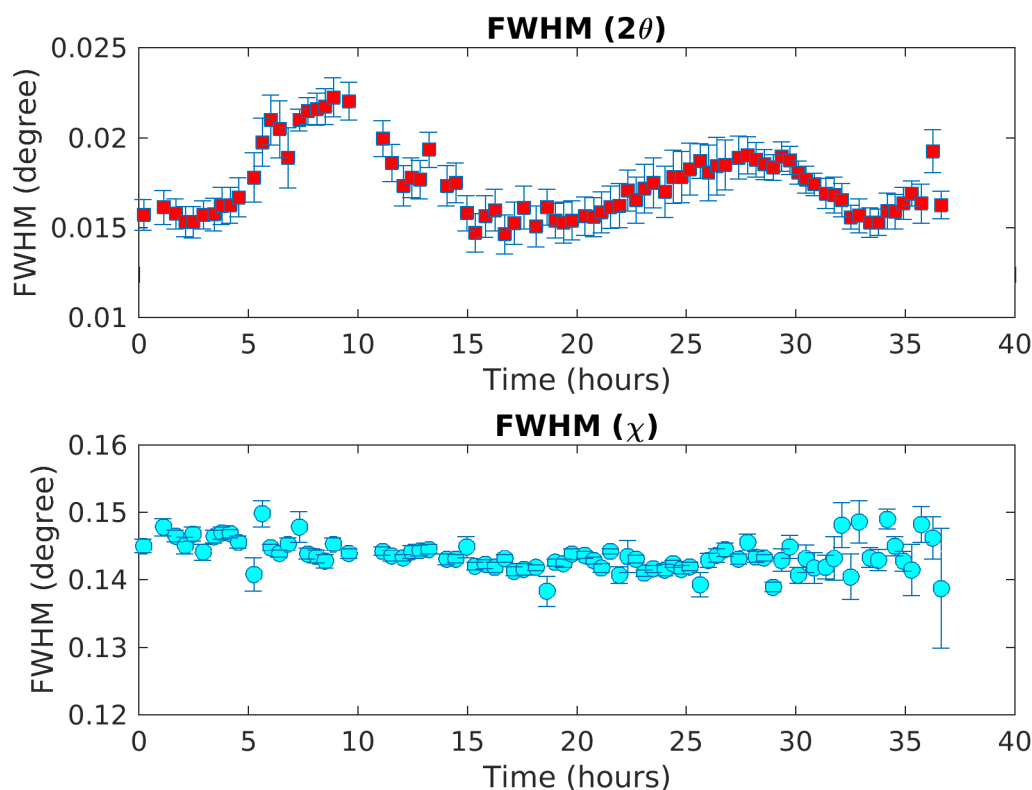


Figure 5.24. Evolution of the FWHM of the mosaicity in 2θ and χ during the experiment. The error bars are given by the Gaussian fit parameter error (provided by MatLab).

As can be seen in Figure 5.24, the FWHM of 2θ fluctuates in a range of $\pm 0.004^\circ$ with no apparent correlation with the phenomena described up to this moment. In the case of the FWHM of χ , the behavior is more stable during the first 32 hours, with exception of a few points, where they seem to be a slightly more scattered with respect to the surrounding points. However, the fluctuation during the experiment is within $\pm 0.005^\circ$, very close to fluctuation in 2θ , with very different average values due to a different impact of the projection when rocking in 2θ and χ . Furthermore, there is a more consistent apparent larger fluctuation in FWHM of χ after 32 hours, which could be related to the increase of tensile strain of the YSZ peaks, described in previous section. In addition to this, the integrated intensity of the grain decreased by a factor of more than 5 in comparison to the

intensities in the first 15 hours, as shown in Figure 5.25. After 15 hours, the integrated intensity of the grain was consistently decreasing up to 31 hours. During the experiment, we were not able to find an explanation of this decrease of the intensity, other than a drift of the position of the grain with respect to the beam. The 2θ and χ central positions were optimized, without changing its range neither the number of steps, in every cycle in order to reduce as much as possible the effect of relevant changes in the integrated intensity due to small rotations of the grain (or the sample); however, this seemed not to be sufficient. Drift of the grain could be due to a drift of the sample, where its position with respect to the beam was estimated to fluctuate in a maximum range of $\pm 1.25 \mu\text{m}$. This uncertainty could cause the grain moving away from the illumination field of the beam, where part of the grain is not being fully illuminated anymore, thus decreasing the total intensity. However, there is no a strong correlation between the decreasing intensity in Figure 5.25 with the position of the “edge” in Figure 5.19 a).

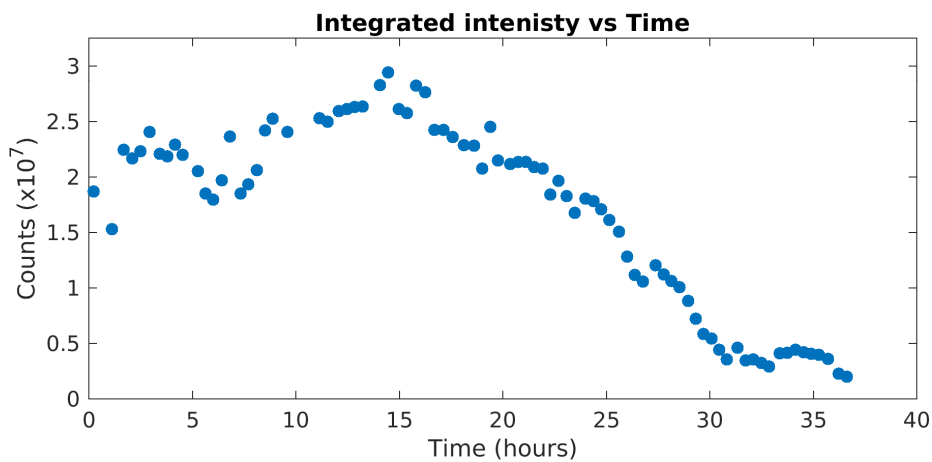


Figure 5.25. Integrated intensity of the grain (found for X-ray microscopy) as a function of time. Unexpectedly, the intensity of the grain decrease continuously after 15 hours of experiment. Notably, the intensities after 31 hours are around 5 times less in comparison to the average intensities in the first 15 hours.

The large decrease of the integrated intensity of the grain results in a reduction of the peak-to-noise ratio in the mosaicity image in Figure 5.23, which increases the uncertainty of the estimation of FWHM of χ and its fluctuation in the last few hours. The large fluctuations of FWHM of 2θ

observed between 6 and 11 hours (Figure 5.24 top) can also be related to a slight decrease of the integrated intensities of the grain between 6 and 10 hours.

Normally, mosaic spread studies involves annealing, or other thermal treatments in which the grain growth and/or reorganization of subgrain structures play an important role in the properties of the final material. Thus, the short variation of FWHM in both cases could indicate a high stability in terms of mosaic spread of YSZ structure under operating conditions.

5.6 Discussion

In this study, the objectives were not fully met, since arising phases from the degradation of the cell were not detected. Therefore, it is difficult to provide a complete picture about the degradation mechanisms in the experiment. Instead, we give a discussion focused on the major problems and findings of the experiment.

5.6.1 Partial reduction of NiO

The presence of oxygen in a Ni grain identified by EDS could indicate the following: a) NiO of the slurry was not fully reduced into Ni, and b) oxidation of Ni in the electrode due to electrochemical reaction and/or due to the combined effect of high temperature and oxygen inside the gas chamber. Regarding the latter, external oxygen can penetrate through the sealing between the quartz tube, alumina tube and the alumina paste due to defects of the materials and/or assembly; however, no testing was done previous nor *post-mortem* in order to discard this.

However, Figure 5.10 b) shows that the oxygen was found close to the center of the grain. If that grain was a full Ni grain during experiment and then it was partially oxidized, it is valid to assume that the oxygen would be present close to the exterior of the grain and not in the interior. Here we assume that no full oxidation occurred, as Ni phase was found by XRD until the end of the experiment. Therefore, the oxygen in the interior of the Ni grain suggests that NiO of the electrode was not fully reduced at the reducing conditions described in 5.2.2, prior the experiment. This is also supported by the detection of NiO phase before applying the polarization, as shown in Figure 9.3 in Appendix, of a diffraction pattern approximately in the middle of the Ni/YSZ electrode.

5.6.2 “Dark” layers between Ni/YSZ electrode and Pt paste

The impurities found in the “dark” region between the Ni/YSZ electrode and the Pt paste is believed to come from the binder of the alumina paste. This implies that the curing process, in addition to annealing at 650 °C during 38 hours are not sufficient to completely remove the impurities, at least when the alumina paste is covered by Pt paste and Pt cable. The presence of this “dark” layer can be attributed to our method of sample preparation, where some of the most liquid part of the alumina paste can remain on the surface of the electrode due to inappropriate application of the paste. Moreover, the alumina paste can also filter through the gaps between the electrode and the Pt paste when applying it, once the Pt cables has been positioned on top of the electrode. Although these “dark” areas were only found in some regions and not on the entire Pt paste / electrode interface, they must be eliminated. “Dark” regions can as electrical insulator, resulting in a decrease of electrical conductivity between the electrode and the Pt cables, reducing thus the performance of the cell. However, no better solution has been found at this moment in order to bond the components of the cell and eliminating the contamination from the alumina pate. Therefore, more effort needs to be made in order to overcome this problem.

5.6.3 R_s and R_p

In Figure 5.15, no clear correlation between R_s and R_p is observed during the first 34-35 hours of operation, which agrees with the findings by Knibbe et al. (8). The evident further increase of both resistances, after 34-35 hours, could be potentially associated to the delamination, as observed in Figure 5.12. This indicates that the exposed region of the cell contributes significantly to the electrochemical reaction, also supported by the large decrease of the current after 34 hours, see Figure 5.11, as no evident changes were observed in the region inside the alumina paste, regarding the morphology and elemental composition. The degradation of the resistances after 34-35 hours explain better the delamination than the degradation at -1.8V in terms of the slope of the current, as shown in Figure 5.13. Degradation in terms of the current (slope) are not consistent for increasing polarization. This remains an open question that needs to be studied by other methods.

Changes of R_s observed during the first 30 hours could be associated to instabilities of the temperature; however, in previous calibrations with the thermocouple, the temperature of the IR furnace appeared to be stable during several hours of testing, within a range of ± 5 °C. Moreover, the decrease of R_s after 27 hours at the highest polarization, hence highest current density, could be attributed to resistive heating of the cell and/or introduction of electronic conductivity in the YSZ electrolyte. Small decrease of R_s has also been reported by Knibbe et al. (8), in impedance studies under cathodic polarization of a YSZ electrolyte based cell. Introduction of electronic conductivity could be caused by a change in the morphology of the electrode/electrolyte interface when applying large cathodic polarizations, as reported by Karin et al.; however, the lack of morphological information in the exposed region of the cell (due to removal during polishing) makes it difficult to confirm the statement, although no significant changes were observed in the Ni/YSZ – YSZ electrolyte interface inside the region of the cell covered by the alumina paste.

5.6.4 Similar findings to another report

Here a summary of the comparison between our results and the findings reported by Balasubramanian (125) is given. The purpose of this comparison is to support the assumption that our cell operated as an electrochemical device. In his work, chronoamperometry and EIS were performed to a cell with similar configuration as described in Hansen et al. (13) at polarizations between -0.1 and -1.6 in voltage step of 0.1V during 5 minutes each at 650 °C in wet 3% H_2 . The current was found to be directly proportional to the polarization, as found in our work; however during each step in voltage the current increased, as opposed to the current decrease observed in our case, shown in Figure 5.11. At -0.7V they detected a small, but noticeable increase in the current, being much more evident at polarizations lower than -1.0V. Their R_s shows similar values than that found in our case, close to $2000 \pm 180 \Omega$, but at polarizations lower than -1.0V the R_s decreased significantly to values around 700Ω , although they reported that the range of polarization there is a higher uncertainty in the estimation of this resistance due to the lack of high frequency values close to the interception point, where $-\text{Im}(Z) = 0$. The similarities in terms of the R_s values found here, do not necessarily indicate that the resistance of the electrolyte behaves equally in both cases despite the cell configuration, as it is known that this resistance is correlated not just only to the temperature, but also to the thickness of the electrolyte.

The behavior of R_p in the report by Balasubramanian (125) is similar to R_p in our case after an applied polarization. In their case a decrease of R_p is seen at polarizations below -0.5V and in our case below -0.6V, however, the interpretation of the polarization in their report is not very clear in terms of the absolute value given by the power supply or in terms of the reference electrode. In addition, values of R_p in their case are approximately 2 orders of magnitude higher than in our case. In their case the contact area between the Ni electrode and the YSZ electrolyte is reported as approximately 0.05 mm², which is around 22 times less than the estimated in our sample, which is 1.1 mm². If these contacting areas are normalized, then the R_p in their report is still being 5 times higher. This could be explained by the difference in real contact area, as for the Ni wire the TPB is defined by the perimeter delimited by the Ni/YSZ contact and not by the complete area as reported, and in our case the TPB is dependent on the porosity of the electrode, which by geometrical factor is much higher at equivalent total contact area.

5.6.5 Strain mapping

In this experiment strain mapping was also performed during the mosaicity map, as described in §4.5.8. However, it is important to say that due to the large decrease of the intensity of the grain during the experiment, as shown in Figure 5.25, and the relatively small size of the grain compared to other experiments at that beamline, which usually involves larger grain size (28) (29) (30), the strain map obtained was not suitable due to its poor quality. Therefore, we do not present this result. Notably, strain mapping is more sensitive than mosaicity mapping, as the former depends strongly on factors related to the grain and the experimental setup, like grain size, proper sample-objective-detector alignment and projection intensity; whereas in mosaicity maps, only the integrated intensities of the images are required. For future experiments, it is then highly recommended searching for better grains in order to obtain good quality strain mapping.

5.7 Conclusions

EIS and XRD were performed simultaneously on *in-operando* YSZ electrolyte based cell, with Ni/YSZ and Pt as cathode and anode respectively, at 650 °C under cathodic polarization in wet 5%H₂ – N₂ atmosphere during approximately 37 hours. Increasing cathodic polarizations were

applied from 0 to -1.8V in 0.2V steps according to the progress of the experiment. Full ring XRD images were collected at different layers across the Ni/YSZ – YSZ electrolyte interface to assess the changes in the microstructure in terms of new phases and strain, as a function of time while increasing polarization. Although the cell appeared to work as an electrochemical device, no new phases were detected close to the cathode/electrolyte interface. The detection of new phases, in case that occurred, could be influenced by factors related to the image processing, concentration of the new phases, region inspected and geometrical setup of the DC detector.

The current shows a direct proportionality to the polarization at initial times of its application. The degradation, in terms of the current at constant polarization, show no consistent correlation to the polarization. The large decrease of the current at highest polarization and the rapid increase of R_s and R_p after 35 hours can be strongly associated to the delamination observed at the Ni/YSZ electrode by tomographic reconstruction.

The strain evolution observed in Ni phase of the Ni/YSZ electrode close to the interface seems to be relatively stable up to 32 hours, while for the YSZ present in the same electrode shows differences in strain according to the diffraction lines. The strain evolution of the YSZ electrolyte grains close to the interface shows a more undefined behavior. This may be attributed to factors related to statistics of diffracting grains, resulting in asymmetry of the peaks, as diffraction images were collected at fixed 2θ . Therefore, it is recommended that in order to improve the quality of the diffraction profile, the sample should be tilted in a small 2θ , thus collecting more diffracting spots like in a more crystalline sample. The increase of tensile strain in Ni and YSZ after 32 hours can be associated to the delamination, as expansion of the lattice of Ni and YSZ of the electrode at the cathode - electrolyte interface may result in cracks, weakening the structure in that region. However, with our available data we cannot establish a direct relation between strain and delamination, as strain was collected close to the interconnectors, while the delamination occurred close to the tip. The removal of the exposed region of the cell during polishing for preparation to SEM, frustrated the attempt of studying the changes in the morphology of the cathode and electrolyte at this region.

Mosaicity map performed by X-ray microscopy to one YSZ electrolyte grain revealed no significant changes in the subgrain structures, confirming its high structural stability of this material under realistic operating conditions. Strain mapping was not possible to achieve properly due to the

combined factors of small grain size and the unexpected and inevitable decrease of the intensity of the grain in the images.

Oxygen detected by EDS in the interior of a Ni grain and the NiO phase detection by XRD before applying polarization suggests a partial reduction of NiO during the reduction process prior to experiment. However, it is not totally clear if additional oxidation occurred at operando conditions due to gas leakage through the gaps of the sealing of the sample and/or oxidation due to electrochemical reaction with the oxygen present in the humidified gas. Moreover, contamination observed at some regions between the Ni/YSZ electrode and the Pt paste can be attributed to the binder of the alumina paste, and that the observed impurities remain after curing (as recommended by the provider and) and long annealing at 650 °C when covered by a layer of Pt paste and Pt cable. The method of application of alumina paste must be improved in order to allow a proper removal of the binder during the curing process, eliminating the “dark” layers, as they can act as electrical insulator, resulting in a decrease of the performance of the cell.

6. Summary and Outlook

6.1 Summary and conclusions

The objective of this work was to study *in-operando* degradation mechanisms on zirconia based solid oxide cells under oxidizing and reducing atmospheres at high polarizations and high operating temperatures. A new method to fabricate the samples was developed, according to the limitations dictated by the experimental setup. In addition, challenging sample setup was designed, demonstrating its functionality for future experiments. To conduct the study, common characterization techniques in solid oxide cell field, such as EIS and SEM/EDS, were used in combination to synchrotron X-rays. Here we present Dark Field X-ray Microscopy, a novel technique for investigations of deeply embedded grains in the material. To the best of our knowledge, the experiments carried out by synchrotron X-rays are unique of its kind.

This work can be divided into two main parts according to the electrolyte composition: ScYSZ and YSZ.

Regarding the first part, symmetrical cells made of ScYSZ electrolyte and LSM/YSZ electrodes were fabricated and tested in the range of temperature between 700 and 900 °C in air at a polarization of 2V during times up to 72 hours. For the first time, void formation was reported to appear in this kind of electrolyte and as short as 6 hours. Statistical results on several individual experiments showed that occurrences of void formation can be correlated to operating temperature and grain size. EIS showed no direct correlation between void formation and degradation of R_s and R_p at temperatures of 700 and 800 °C, but the high degradation of resistances at 900 °C can be associated to higher occurrences of voids, in addition to delamination observed at the anode/electrolyte interface. Microstructural studies by classical XRD showed a contraction of the lattice close to the anode/electrolyte interface, which is expected to be caused by the local effect of voids arising in the grain boundaries. Additionally, high pO_2 at this side confirms that voids can be caused by the high oxygen pressure build-up. The larger contraction of the electrolyte lattice close to the cathode interface can be attributed to an oxygen deficiency or increase of oxygen

vacancy concentration in the electrolyte. Within the grains, DFXRM showed an increase in local compressive strain inside the projection of the grain and rotated regions at the edges after 10.5 hours, that are consistent with strain localization at the boundary of the grain.

The second study was carried out on a YSZ electrolyte based cell, with Ni/YSZ and Pt electrodes in a reducing gas environment at 650 °C, where the polarizations were applied increasingly according to the progress of the experiment. The experiment involved simultaneous XRD and EIS to evaluate the degradation expected in terms of electrochemical parameters and microstructural changes. The results from XRD and *post-mortem* SEM/EDS did not show formation of new phases; however, after approximately 34-35 of operation, a large delamination of the Ni/YSZ electrode was observed in the exposed region of the cell. The large increase of R_s and R_p are consistent to this phenomenon, and possibly associated to the large increase of tensile strain of Ni and YSZ phases of the electrode. Also, EDS revealed impurities blocking the interface between the Ni/YSZ electrode and the Pt paste. The contamination is believed to come from the alumina paste, even after carefully following the curing process recommended by the provider and after several hours at high temperature. Further efforts are necessary in order avoid this unwanted event. X-ray microscopy was not completely achieved, as the unexpected decrease of the diffraction intensities did not allow to perform proper strain mapping. However, mosaicity map confirmed the high structural stability of the YSZ electrolyte under working conditions.

6.2 Outlook

The presented results show the work conducted during three years of investigations, however, issues related to sample design and preparation and experimental part may be improved for future research. Understanding these problems is crucial for aiming better experiments and consequently better results. The following summarizes the suggestions for further improvements that may overcome the issues:

- Contamination of alumina paste: alumina paste demonstrated to have suitable structural stability and electrical insulating properties under high temperatures; however, the impurities in this material, believed to come from the binder substances, may have a negative impact on the electrodes. After gaining experience in previous in-house tests, the methodology for assembling the components of the cell was optimized. One of the steps consists in applying a thin layer of alumina paste on the sides of the cell in order to avoid short circuit when applying later the Pt paste. The method used here to apply the layer of alumina paste is prone to result in penetration of alumina paste in the electrode pores, leading to undesirable effects and making the system more complex during analysis of the results. A way to avoid contamination could be by applying a sufficiently small amount of Pt paste to the metallic contacts to prevent excess of it, avoiding short circuit before or during experiment. In this way the necessity for applying alumina paste is not required. Another way could be by eliminating completely the use of the alumina paste, with the metallic contacts pressed against the electrodes (with or without Pt paste) by other components designed for this purpose, however, the limitations of the instrument (at the beamline) and the sample condition in terms of dimensions, temperature, polarization and gas environment makes this extremely difficult to achieve.
- Gas sealing: in previous tests, it was found that alumina paste performs well as gas sealing, however at pressures around 5 bars its performance starts to decrease significantly, compromising the concentration of the reducing gas atmosphere by contamination of oxygen from open air. The search of other materials suitable for this purpose is required in

order to avoid failures by sealing. Other way could be to apply more layers of alumina paste to increase significantly the sealing properties.

- Statistics of void formation: the statistics results presented in Chapter 4 regarding *post-mortem* experiments were carried out with one cell at the specified temperature and time. If unexpected failure of cells occur either by wrong assembly or during experiments, these results may not be correct. More testing at same conditions should reveal more reliable void formation statistics. In addition, fracturing the cells at more places should also contribute to a better statistics, however this is difficult due to the small sizes of the cells when manipulating with hands.
- Estimation of strain/stress of void formation in the structure: an estimation of the effect of voids in the structure in terms of strain/stress could confirm the results of d-spacing evolution. The estimation would involve the void size distribution and the density of voids as a function of the distance from the interface. A way to find these parameters could be the use of very high resolution tomography capable to detect nanometer size voids, or by using FIB/SEM methods to survey a 3D volume. However, these methods are still limited by a very small volume of the sample.
- Statistics of DFXRM: results presented by DFXRM are from single grains in the studied structures. This is a powerful technique to look the structures inside the grains; however one grain does not offer a complete picture of all the grains of the material. Periodically finding and relocating more grains is time consuming, which is not convenient in a beamtime period of few days. Many efforts are being taken to speed up this technique at the beamline.
- Estimation of overpotential: in Chapter 4, the oxygen partial pressure was estimated based in the corresponding parameters given in the equation, in which the overpotential of the electrodes were estimated by assuming the same behavior, thus dividing by two the obtained polarization resistance. As the electrochemical reactions at both electrodes are different, a more accurate way to estimate the contribution of polarization resistance should be taken into consideration. As the performance of the electrodes are related to porosity, tortuosity, percolation, gas environment, temperature, polarization, etc, a

mathematical model based on these parameters can be developed, giving the overpotential with a higher accuracy.

- Reduction of Ni: results in Chapter 5 show that NiO was present even before applying polarization. The presence of this phase can be attributed to an incomplete Ni reduction. More analysis should be made in order to evaluate the effectiveness of the method used and to further confirm a full Ni reduction.
- Background removal: the background removal of the DC images in Chapter 5 was performed in such a way to remove as little information as possible with regards to the rings and peaks. However, due to the complexity of the background, small features belonging to real information from the sample could have been eliminated, resulting in a non-detection of new phases. The background removal can be improved by more advanced imaging tools.
- Formation of new intermetallic phases: the results in Chapter 5 show that no intermetallic phases were detected. This is not in good agreement with what was expected from the literature. However, not finding new phases by EDS nor XRD does not necessarily mean that there was no phase formation during operando conditions. This can be solved by performing more experiments in similar conditions and setup, to verify if new phases arise.

7. Bibliography

1. *Fuel Cell Systems Explained*. **Larminie, J.** 2003, John Wiley & Sons Ltd.
2. *Effect of Anode off-gas Recycling on Reforming of Natural Gas for Solid Oxide Fuel Cell Systems*. **Halinen, M., Thomann, O. and Kiviaho, J.** 2012, Fuel Cells, pp. 754-760.
3. *Materials for fuel-cell technologies*. **Steele, B. C. H. and Heinzel, A.** 2001, Nature, Vol. 414, pp. 345–352.
4. *Atomic structure and composition of the yttria-stabilized zirconia (111) surface*. **Vonk, V., et al.** 2013, Surface Science, Vol. 612, pp. 69-76.
5. *Challenges in the development of reversible solid oxide cell*. **Jiang, S. P.** 2016, Chemical Engineering, Vol. 11, pp. 386-391.
6. *Solid Oxide Electrolysis Cells: Performance and Durability*. **Hauch, A.** 2007, Ph.D Thesis. Technical University of Denmark. Fuel Cells and Solid State Chemistry Department.
7. *Eliminating degradation in solid oxide electrochemical cells by reversible operation*. **Graves, C., et al.** 2014, Nature Materials, pp. 239-244.
8. *Solid Oxide Electrolysis Cells: Degradation at High Current Densities*. **Knibbe, R., et al.** 2010, Journal of The Electrochemical Society, pp. 1209-1217.
9. *Electrolyte degradation in anode supported microtubular yttria stabilized zirconia-based solid oxide steam electrolysis cells at high voltages of operation*. **Laguna-Bercero, M. A., et al.** 2011, Journal of Power Sources, pp. 8942-8947.
10. *Degradation phenomena in a solid oxide electrolysis cell after 9000 h of operation*. **Tietz, F., et al.** 2013, Journal of Power Sources, pp. 129-135.
11. *Degradation of Anode Supported SOFCs as a Function of Temperature and Current Load*. **Hagen, A., et al.** 2006, Journal of The Electrochemical Society, Vol. 153, pp. A1165-A1171 .
12. *Understanding degradation of solid oxide electrolysis cells through modeling of electrochemical potential profiles*. **Chatzichristodoulou, C., et al.** 2016, Electrochimica Acta, pp. 265–282.
13. *Effects of Strong Cathodic Polarization of the Ni-YSZ Interface*. **Hansen, K. V., et al.** 10, 2016, Journal of The Electrochemical Society, Vol. 163, pp. F1217-F1227.
14. *Three dimensional characterization of nickel coarsening in solid oxide cells via ex-situ ptychographic nano-tomography*. **Angelis, S. De, et al.** 2018, Journal of Power Sources, Vol. 383, pp. 72-79.
15. *A Detailed Post Mortem Analysis of Solid Oxide Electrolyzer Cells after Long-Term Stack Operation*. **Frey, C. E., et al.** 5, 2018, Journal of The Electrochemical Society, Vol. 165, pp. F357-F364.

16. *Performance of a glass-ceramic sealant in a SOFC short stack.* **Smeacetto, F., et al.** 2013, International Journal of Hydrogen Energy, Vol. 38, pp. 588-596.
17. *Quantitative Data Analysis Methods for 3D Microstructure Characterization of Solid Oxide Cells.* **Jørgensen, P. S.** 2010, Ph.D Thesis. Technical University of Denmark.
18. *Life testing of LSM–YSZ composite electrodes under reversing-current operation.* **Hughes, G. A., Yakal-Kremski, K. and Barnett, S. A.** 2013, Phys. Chem. Chem. Phys, Vol. 15, pp. 17257-17262.
19. *High temperature solid oxide H₂O/CO₂ co-electrolysis for syngas production.* **Wang, Y., et al.** 2017, Fuel Processing Technology, Vol. 161, pp. 248-258.
20. **Singhal, S. C. and Kendall, K.** *High Temperature Solid Oxide Cells, Fundamental, Design and Applications.* Oxford : Elsevier Advanced Technology, 2003.
21. *NiO/YSZ Reduction for SOFC/SOEC studied in situ by Environmental Transmission Electron Microscopy.* **Simonsen, S. B., et al.** 2, 2014, ECS Transactions, Vol. 64, pp. 73-80.
22. *YSZ-Based Oxygen Sensors and the Use of Nanomaterials: A Review from Classical Models to Current Trends.* **López-Gándara, C., Ramos, F. M. and Cirera, A.** 2009, Journal of Sensors, p. 15.
23. *Degradation in Solid Oxide Cells During High Temperature Electrolysis.* **Sohal, M. S.** 2009, Idaho National Laboratory. <https://inldigitallibrary.inl.gov/sites/sti/sti/4247164.pdf>.
24. *Durability of Solid Oxide Electrolysis Cell and Interconnects for Steam Electrolysis.* **Sun, X., et al.** 1, 2013, The Electrochemical Society, Vol. 57, pp. 3229-3238.
25. *The Course of Oxygen Partial Pressure and Electric Potentials across an Oxide Electrolyte Cell.* **Jacobsen, T. and Mogensen, M.** 2008, ECS Transactions, pp. 259-273.
26. *3D phase mapping of solid oxide fuel cell YSZ/Ni cermet at the nanoscale by holographic X-ray nanotomography.* **Villanova, J., et al.** 2013, Journal of Power Sources, Vol. 243, pp. 841-849.
27. *Ex-situ tracking solid oxide cell electrode microstructural evolution in a redox cycle by high resolution Ptychographic nanotomography.* **Angelis, S. De, et al.** 2017, Journal of Power Sources, Vol. 360, pp. 520-527.
28. *Dark field X-ray microscopy for studies of recrystallization.* **Ahl, S. R., et al.** 2015, Materials Science and Engineering, Vol. 89.
29. *Multiscale 3D characterization with dark-field x-ray microscopy.* **Simons, H., et al.** 2016, MRS Bulletin, Vol. 4, pp. 454-459.
30. *Dark-field X-ray microscopy for multiscale structural characterization.* **Simons, H., et al.** 2015, Nature Communications, pp. 1-6.
31. *Mechanism of oxygen electrode delamination in solid oxide electrolyzer cells.* **Virkar, A. V.** s.l. : Elsevier Ltd, 2010, International Journal of Hydrogen Energy, Vol. 35, pp. 9527-9543.

32. *Electrolyte Materials for Solid Oxide Fuel Cell*. **Biswas, M. and Sadanala, K. C.** 4, 2013, Journal of Powder Metallurgy & Mining, Vol. 2, pp. 1-6.
33. *Conduction in Bi₂O₃-based oxide ion conductors under low oxygen pressure. I. Current blackening of the Bi₂O₃- Y₂O₃ electrolyte*. **Takahashi, T., Esaka, T. and Iwahara, H.** 1976, Journal of Applied Electrochemistry, Vol. 7, pp. 299-302.
34. *High oxygen ion conduction in sintered oxides of the Bi₂O₃---Ln₂O₃ system*. **Verkerk, M. J. and Burggraaf, A. J.** 4, 1981, Solid State Ionics, Vol. 3, pp. 463-467.
35. *Transport properties of solid oxide electrolyte ceramics: a brief review*. **Kharton, V. V., Marques, F. M. B. and Atkinson, A.** 2004, Solid State Ionics, Vol. 174, pp. 135 – 149.
36. *Physical, chemical and electrochemical properties of pure and doped ceria*. **Mogensen, M., Sammes, N. M. and Tompsett, G. A.** 2000, Solid State Ionics, Vol. 129, pp. 63-94.
37. *Microstructural properties of multi-nano-layered YSZ thin films*. **Amézaga, P., et al.** 2010, Journal of Alloys and Compounds, Vol. 495, pp. 629-633.
38. *Preparation of Yttria-Stabilized Zirconia by the Reverse Microemulsion Method and the Effect of Sc and Ce Doping on Microstructure and Ionic Conductivity for Solid Oxide Fuel Cell Applications*. **Oksuzomer, F., et al.** 2011, International Journal of Applied Ceramic Technology, pp. 42-48.
39. *Characterization of Nanocrystalline Yttria-Stabilized Zirconia: An In Situ HTXRD Study*. **Biswas, M., Chandrashekhar, C. S. and Gowtam, D. S.** 2011, ISRN Nanotechnology, p. 4.
40. *Analysis of Electric Properties of ZrO₂-Y₂O₃ Single Crystals Using Terahertz IR and Impedance Spectroscopy Techniques*. **Artemov, V. G., et al.** 7, 2014, Russian Journal of Electrochemistry,, Vol. 50, pp. 690-693.
41. *Optical and mechanical properties of amorphous and crystalline yttria-stabilized zirconia thin films prepared by pulsed laser deposition*. **Heiroth, S., et al.** 2011, Acta Materialia, Vol. 59, pp. 2330–2340.
42. *Co-doping of scandia–zirconia electrolytes for SOFCs*. **Irvine, J. T. S., et al.** 2006, The Royal Society of Chemistry, Vol. 134, pp. 41-49.
43. *Investigation of scandia–yttria–zirconia system as an electrolyte material for intermediate temperature fuel cells - influence of yttria content in system (Y₂O₃)_x(Sc₂O₃)_(11-x)(ZrO₂)₈₉*. **Politova, T. I. and Irvine, J. T. S.** 2004, Solid State Ionics, pp. 153-165.
44. *A Review of RedOx Cycling of Solid Oxide Fuel Cells Anode*. **Faes, A., et al.** 2012, Membranes, Vol. 2, pp. 585-664.
45. *Compilation of mechanical properties for the structural analysis of solid oxide fuel cell stacks. Constitutive materials of anode-supported cells*. **Nakajo, A., et al.** 2012, Ceramics International, Vol. 38, pp. 3907–3927.

46. *Thermal expansion coefficient of yttria stabilized zirconia for various yttria contents.* **Hayashi, H., et al.** 2005, Solid State Ionics, pp. 613-619.
47. *Thermal Expansion of Nickel-Zirconia Anodes in Solid Oxide Fuel Cells during Fabrication and Operation.* **Mori, M., et al.** 4, 1998, Journal of Electrochemical Society, Vol. 145, pp. 1374-1381.
48. *High Temperature Electrolysis in Alkaline Cells, Solid Proton Conducting Cells, and Solid Oxide Cells.* **Ebbesen, S. D., et al.** 2014, American Chemical Society, pp. 10697-10734.
49. **Li, N.** The Interaction of LSM-YSZ Composite and Improvement of the Solid Oxide Cell Durability by Mn-modified YSZ. s.l. : UCONN Library, 2014.
50. *Computational Modelling Study of Yttria-stabilized Zirconia.* **Xia, X.** 2010, PhD Thesis. Department of Chemistry, University College London.
51. *Absorption and emission spectra of Yttria-Stabilized Zirconia and magnesium oxide.* **Kunz, M., et al.** [ed.] Journal of Luminescence. 1987, Vol. 37, pp. 123-131.
52. *Defect configuration and phase stability of cubic versus tetragonal yttria-stabilized zirconia.* **Ding, H., Virkar, A. V. and Liu, F.** 2012, Solid State Ionics, Vol. 215, pp. 16-23.
53. *Molecular dynamics simulations of oxygen ion diffusion in yttria-stabilized zirconia.* **Perumal, T. Pramananda, et al.** 2002, Physica A, Vol. 309, pp. 35-44.
54. **Stortelder, J. K.** Ionic Conductivity in Yttria-Stabilized Zirconia Thin Films grown by Pulsed Laser Deposition. 2005.
55. *Formation of metastable forms by quenching of the $HfO_2RO_{1.5}$ melts ($R = Gd, Y$ and Yb).* **Yashima, M., et al.** 3, 1996, Journal of Physics and Chemistry of Solids, Vol. 57, pp. 289-295.
56. *X-ray diffraction study of compositionally homogeneous, nanocrystalline yttria-doped zirconia powders.* **Lamas, D. G. and Reza, N. E. Walsöe De.** 2000, Journal of Materials Science, Vol. 35, pp. 5563-5567.
57. *Revisiting the Temperature Dependent Ionic Conductivity of Yttria Stabilized Zirconia (YSZ).* **Ahamer, C., et al.** 7, 2017, Journal of The Electrochemical Society, Vol. 164, pp. F790-F803.
58. *Ionic Conductivity in Yttria-Stabilized Zirconia Thin Films grown by Pulsed Laser Deposition.* **Stortelder, J. K.** 2005, Master Thesis. University of Twente, Faculty of Science and Technology. The Netherlands.
59. *Molecular dynamics simulations of yttria-stabilized zirconia.* **Brinkman, H. W., Briels, W. J. and Verweij, H.** 1995, Chemical Physics Letters, Vol. 247, pp. 386-390.
60. *Influence of microstructure on the ionic conductivity of yttria-stabilized zirconia electrolyte.* **Chen, X. J., et al.** 2002, Materials Science and Engineering, Vol. A335, pp. 246–252.
61. *Molecular dynamics analysis of ionic conduction mechanism in yttria-stabilized zirconia.* **Yamamura, Y., Kawasaki, S. and Sakai, H.** 1999, Solid State Ionics, Vol. 126, pp. 181-189.

62. *Zirconia-based solid electrolytes: microstructure, stability and ionic conductivity*. **Badwal, S. P. S.** 1992, *Solid State Ionics*, Vol. 52, pp. 23-32.
63. *Revised Effective Ionic Radii and Systematic Studies of Interatomic Distances in Halides and Chalcogenides*. **Shannon, R. D.** 1976, *Acta Crystallographica*, pp. 751-767.
64. *Ionic conductivity and its temperature dependence of atmospheric plasma-sprayed yttria stabilized zirconia electrolyte*. **Zhang, Ch., et al.** 2007, *Materials Science and Engineering*, Vol. 137, pp. 24-30.
65. *Structure and conductivity of yttria and scandia-doped zirconia crystals grown by skull melting*. **Borik, M. A., et al.** 2017, *Journal of American Ceramic Society*, Vol. 100, pp. 5536-5547.
66. *Fracture process of nonstoichiometric oxide based solid oxide fuel cell under oxidizing/reducing gradient conditions*. **Sato, K., et al.** 2010, *Journal of Power Sources*, Vol. 195, pp. 5481–5486.
67. *Understanding Chemical Expansion in Non-Stoichiometric Oxides: Ceria and Zirconia Case Studies*. **Marrocchelli, D., et al.** 2012, *Advanced Functional Materials*, Vol. 22, pp. 1958-1965.
68. *Chemical Expansion: Implications for Electrochemical Energy Storage and Conversion Devices*. **Bishop, S. R., et al.** 2014, *Annual Review Materials Research*, Vol. 44, pp. 205-239.
69. *Scanning Electron Microscopy and X-ray Microanalysis*. **Goldstein, J. I., et al.** s.l. : Third edition, 2003, Kluwer Academic/Plenum Publishers.
70. *Transmission Electron Microscopy*. **Williams, D. B. and Carter, C. B.** s.l. : Second Edition, 2009, Springer.
71. *Electrochemical impedance spectroscopy: an overview of bioanalytical applications*. **Randviir, E. P. and Banks, C. E.** 2013, *Analytical Methods*, Vol. 5, pp. 1098-1115.
72. *Impedance Spectroscopy, Theory, Experiment, and Applications*. **Barsoukov, E. and Macdonald, R.** 2005, John Wiley & Sons, p. 26.
73. *Electrochemical Impedance Spectroscopy*. **Orazem, M. E. and Tribollet, B.** s.l. : The electrochemical Society. Second Edition, 2017, John Wiley & Sons.
74. *Impedance Spectroscopy: Applications to Electrochemical and Dielectric Phenomena*. **Lvovich, V. F.** 2012, John Wiley & Sons.
75. *Spectroelectrochemical cell for in situ studies of solid oxide fuel cells*. **Hagen, A., et al.** 2012, *Journal of Synchrotron Radiation*, Vol. 19, pp. 400-407.
76. *Characterization of Yttria-Stabilized Zirconia Thin Films Prepared by Radio Frequency Magnetron Sputtering for a Combustion Control Oxygen Sensor*. **Bae, J. W., et al.** 6, 2000, *Journal of The Electrochemical Society*, Vol. 147, pp. 2380-2384.
77. *Elements of x-ray Diffraction*. **Cullity, B. D.** s.l. : Secod Edition, 1978, Addison-Wesley.
78. *X-Ray Diffraction Crystallography*. **Waseda, Y., Matsubara, E. and Shinoda, K.** 2011, Springer.

79. *Effect of thickness-dependent crystal mosaicity and chemical defect on electric properties in yttrium-stabilized epitaxial HfO₂ thin films.* **Liu, W., et al.** 2017, APPLIED PHYSICS LETTERS, Vol. 110, p. 122904.
80. *Elements of a Method for Multiscale Characterization of Recrystallization in Deformed Metals.* **Ahl, S. R.** 2018, PhD Thesis.
81. *Focusing properties of mosaic crystals.* **Río, M. Sánchez del, et al.** San Diego, CA, United States : PROCEEDINGS OF SPIE, 1998. PROCEEDINGS OF SPIE.
82. *Extinction in mosaic crystals.* **Werner, S. A.** 8, 1974, Journal of Applied Physics, Vol. 45, pp. 3246-3254.
83. *Change of Young's Modulus with Increasing Applied Tensile Strain in Open Cell Nickel and Copper Foams.* **Ochiai, S., et al.** 5, 2010, Materials Transactions, Vol. 51, pp. 925-932.
84. *Representative Stress-Strain Curve by Spherical Indentation on Elastic-Plastic Materials.* **Chang, C., et al.** s.l. : Hindawi, 2018, Advances in Materials Science and Engineering, Vol. 2018, pp. 1-9.
85. *Simulating and optimizing compound refractive lens-based X-ray microscopes.* **Simons, H., et al.** 2017, Journal of Synchrotron Radiation, Vol. 24, pp. 392-401.
86. *Using Variable Temperature Powder X-ray Diffraction To Determine the Thermal Expansion Coefficient of Solid MgO.* **Corsepius, N. C., et al.** 5, 2007, Journal of Chemical Education, Vol. 84, pp. 818-821.
87. *Anisotropic Thermal Expansion Characteristics of Some Crystal Structures.* **Cartz, L.** 1967. Proceedings of an International Symposium on Anisotropy in Single-Crystal Refractory Compounds. pp. 383-389.
88. *Linear thermal expansion coefficient determination using in situ curvature and temperature dependent X-ray diffraction measurements applied to metalorganic vapor phase epitaxy-grown AlGaAs.* **Maaßdorf, A., et al.** 2013, JOURNAL OF APPLIED PHYSICS, Vol. 114, pp. 033501-1 - 033501-7.
89. *Densification and properties of zirconia prepared by three different sintering techniques.* **Dahl, P., et al.** 2007, Ceramics International, Vol. 33, pp. 1603-1610.
90. *Average Grain Size in Polycrystalline Ceramics.* **Mendelson, M. I.** 1969, Journal of the American Ceramic Society, pp. 443-446.
91. *Sintering of 4YSZ (ZrO₂ + 4 mol% Y₂O₃) nanoceramics for solid oxide fuel cells (SOFCs), their structure and ionic conductivity.* **Mæland, D., et al.** 2009, Journal of the European Ceramic Society, Vol. 29, pp. 2537-2547.
92. *Formation of La₂Zr₂O₇ or SrZrO₃ on cathode-supported solid oxide fuel cells.* **Yang, K., et al.** 2006, Journal of Power Sources, Vol. 159, pp. 63-67.
93. *Development of Lanthanum Strontium Manganite Perovskite Cathode Materials of Solid Oxide Fuel Cells: A Review.* **Jiang, S. P.** 2008, Journal of Materials Science, Vol. 43, pp. 6799–6833.
94. *Influence of oxygen partial pressure on surface tension of molten silver.* **Ozawa, S., et al.** 2010, Journal of Applied Physics, Vol. 107, pp. 014910-1 - 014910-7.

95. **Poulsen, H. F.** *Three-Dimensional X-Ray Diffraction Microscopy - Mapping Polycrystals and their Dynamics*. s.l. : Springer, 2004. Vol. 205.
96. *Tutorial and source code of ImageD11.* **Wright, J.** s.l.: Sourceforge, <https://github.com/jonwright/ImageD11>. Documentation and download scripts available.
97. *X-ray diffraction microscopy based on refractive optics.* **Poulsen, H. F., et al.** 2017, *Journal of Applied Crystallography*, Vol. 50, pp. 1441-1456.
98. *Quantitative Stereology.* **Underwood, E. E.** 1970, Addison-Wesley.
99. *A Mathematical Model of a Solid Oxide Fuel Cell.* **Bessette, N. F., Wepfer, W. J. and Winnick, J.** 11, 1995, *Journal of Electrochemical Society*, Vol. 142, pp. 3792-3800.
100. *A simple model for interconnect design of planar solid oxide fuel cells.* **Tanner, C. W. and Virkar, A.** 2003, *Journal of Power Sources*, Vol. 113, pp. 44-56.
101. *Morphology and thermal conductivity of yttria-stabilized zirconia coatings.* **Zhao, H., et al.** 2006, *Acta Materialia*, Vol. 54, pp. 5195-5207.
102. *Degradation mechanism of electrolyte and air electrode in solid oxide electrolysis cells operating at high polarization.* **Kim, J., et al.** 2013, *International Journal of Hydrogen Energy*, pp. 1225-1235.
103. *High temperature mechanical properties of zirconia tapes used for electrolyte supported solid oxide fuel cells.* **Fleischhauer, F., et al.** 2015, *Journal of Power Sources*, Vol. 273, pp. 237-243.
104. *Failure mechanism of (La Sr) MnO₃ oxygen electrodes of solid oxide electrolysis cells.* **Chen, K. and Jiang, S. P.** 36, 2011, *International Journal of Hydrogen Energy*, pp. 10541-10549.
105. *Degradation mechanism of electrolyte and air electrode in.* **Kim, J., et al.** 2013, *International Journal of Hydrogen Energy*, pp. 1225-1235.
106. *Nonstoichiometry of ZrO₂ and its relation to tetragonal-cubic inversion in ZrO₂.* **Ruh, R. and Garret, H. J.** 5, 1967, *Journal of the American Ceramic Society*, Vol. 50, pp. 257-261.
107. *Particle Coarsening Influence on Oxygen Reduction in LSM-YSZ composite Materials.* **Farlenkov, A. S., et al.** 1, 2015, *Fuel Cells*, Vol. 15, pp. 131-139.
108. *Impedance of Solid Oxide Fuel Cell LSM/YSZ Composite Cathodes.* **Jørgensen, M. J. and Mogensen, M.** 5, 2001, *Journal of The Electrochemical Society*, Vol. 148, pp. A433-A442.
109. *Silica Segregation in the Ni/YSZ Electrode.* **Hauch, A., et al.** 7, 2007, *Journal of The Electrochemical Society*, Vol. 154, pp. A619-A626.
110. *Electrochemically Scavenging the Silica Impurities at the Ni-YSZ Triple Phase Boundary of Solid Oxide Cells.* **Tao, Y., Shao, J. and Cheng, S.** 2016, *Applied Materials and Interfaces*, Vol. 8, pp. 17023-17027.
111. *Etch rates of crystallographic planes in Z-cut quartz - experiments and simulation.* **Rangsten, P., et al.** 6, 1998, *J. Micromechanical and Microengineering*, Vol. 1, pp. 1-6.

112. *The Effect of HF/NH₄F Etching on the Morphology of Surface Fractures on Fused Silica*. **Wong, L., et al.** 2008, *Journal of Non-Crystalline Solids*, pp. 1-51.
113. *Etch Rates for Micromachining Processing - Part II*. **Williams, K. R., Gupta, K. and Wasilik, M.** 6, 2003, *Journal of Microelectromechanical Systems*, Vol. 12, pp. 761-778.
114. *Etching with Hydrofluoric Acid*. **Microchemicals**. 2013, www.microchemicals.com. Document at URL: https://www.microchemicals.com/technical_information/hf_etching.pdf.
115. *X-Ray attenuation & absorption calculator*. **Weber, G.** 2018, X-Ray attenuation and absorption calculator. Website https://web-docs.gsi.de/~stoe_exp/web_programs/x_ray_absorption/index.php.
116. *The FIT2D Home Page*. **Hammersley, A.** 2016, ESRF-FIT2D. Website <http://www.esrf.eu/computing/scientific/FIT2D/>.
117. *Inorganic Crystal Structure Database*. **ICSD**. 2018, FIZ Karlsruhe. Website http://www2.fiz-karlsruhe.de/icsd_home.html.
118. *High-temperature thermal expansion of six metallic elements measured by dilatation method and X-ray diffraction*. **Suh, I., Ohta, H. and Waseda, Y.** 1988, *Journal of Materials Science*, Vol. 23, pp. 757-760.
119. **Report, ICSD**. *Report on structural parameters and TEC of NiO*. URL at: http://extras.springer.com/2000/978-3-540-64966-3/41d_pdf/68s03d02.pdf.
120. *Spin-glass-like behavior of uncompensated surface spins in NiO nanoparticulated powder*. **Aragón, F.H., et al.** 2012, *Physica*, Vol. 407, pp. 2601-2605.
121. *Effect of porosity on the thermal expansion coefficient: A discussion on the paper 'Effects of mineral admixtures on the thermal expansion properties of hardened cement paste'*. **Ghabezloo, S.** 9, 2010, *Construction and Building Materials*, Vol. 24, pp. 1796–1798.
122. *Effect of Porosity on the Thermal Expansion Coefficient of Porous Materials*. **Ghabezloo, S.** June 2013, Fifth Biot Conference on Poromechanics.
123. *Micromechanical analysis of the effect of porosity on the thermal expansion coefficient of heterogeneous porous materials*. **Ghabezloo, S.** s.l. : 2012, *International Journal of Rock Mechanics & Mining Sciences*, Vol. 55, pp. 97-101.
124. *Effects of mineral admixtures on the thermal expansion properties of hardened cement paste*. **Shui, Z., et al.** 2010, *Construction and Building Materials*, Vol. 24, pp. 1761–1767.
125. **Balasubramanian, V.** *Data Report - 36t34*. *Energy Conversion and Storage*, DTU. 2017.

8. Abbreviations

SOC	solid oxide cell
SOFC	solid oxide fuel cell
SOEC	solid oxide electrolyzer cell
XRD	X-ray diffraction
DFXRM	dark field x ray microscopy
EIS	electrochemical impedance spectroscopy
SEM	scanning electron microscope
YSZ	yttria stabilized zirconia
ScYSZ	scandium yttria stabilized zirconia
LSM	lanthanum strontium manganate
EDS	energy dispersive spectroscopy

9. Appendix

9.1 Notes about experiments and data analysis

The *post-mortem* experiments were carried out in Scandia tube furnace with no gas flow, only the natural gas environment that is inside the furnace they were never completely sealed. The Pt cables run inside an alumina rod with millimeter diameter sized holes. A porous alumina cylinder with a notch having suitable diameter size allows the alumina rod pass through. This ensures a more homogenous distribution of thermal heating, thus better temperature stability, control and measurement and simultaneously provides some air flow (containing oxygen gas), between the interior of the furnace and the outside.

Most of the synchrotron data were analyzed using MatLAB. The raw synchrotron data is given in a specific format from the ESRF beamline data acquisition system. Every image taken by the CCD comes in “.edf” format. Each file is divided basically in two parts: a header of the file, which contains some parameters of the beam, time, date, name of file, size of image, all the motor positions, etc. and the second part, which contains the 2D image (in black and white). All the information of file can be read and extracted by already given MatLAB scripts.

The strain map was obtained by a MatLAB script developed by H. Simons

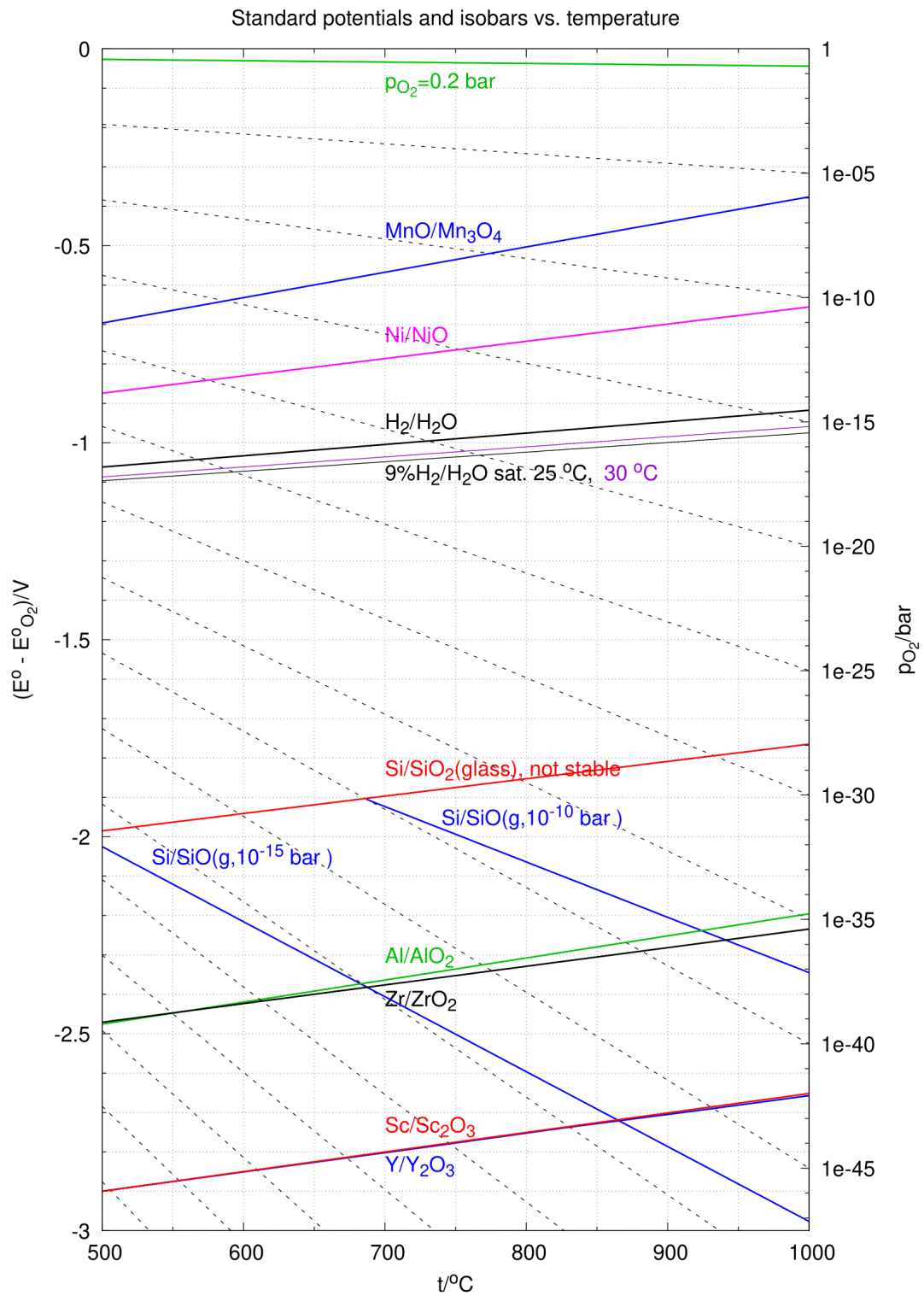


Figure 9.1. Ellingham diagram containing Y, Sc and Zr.

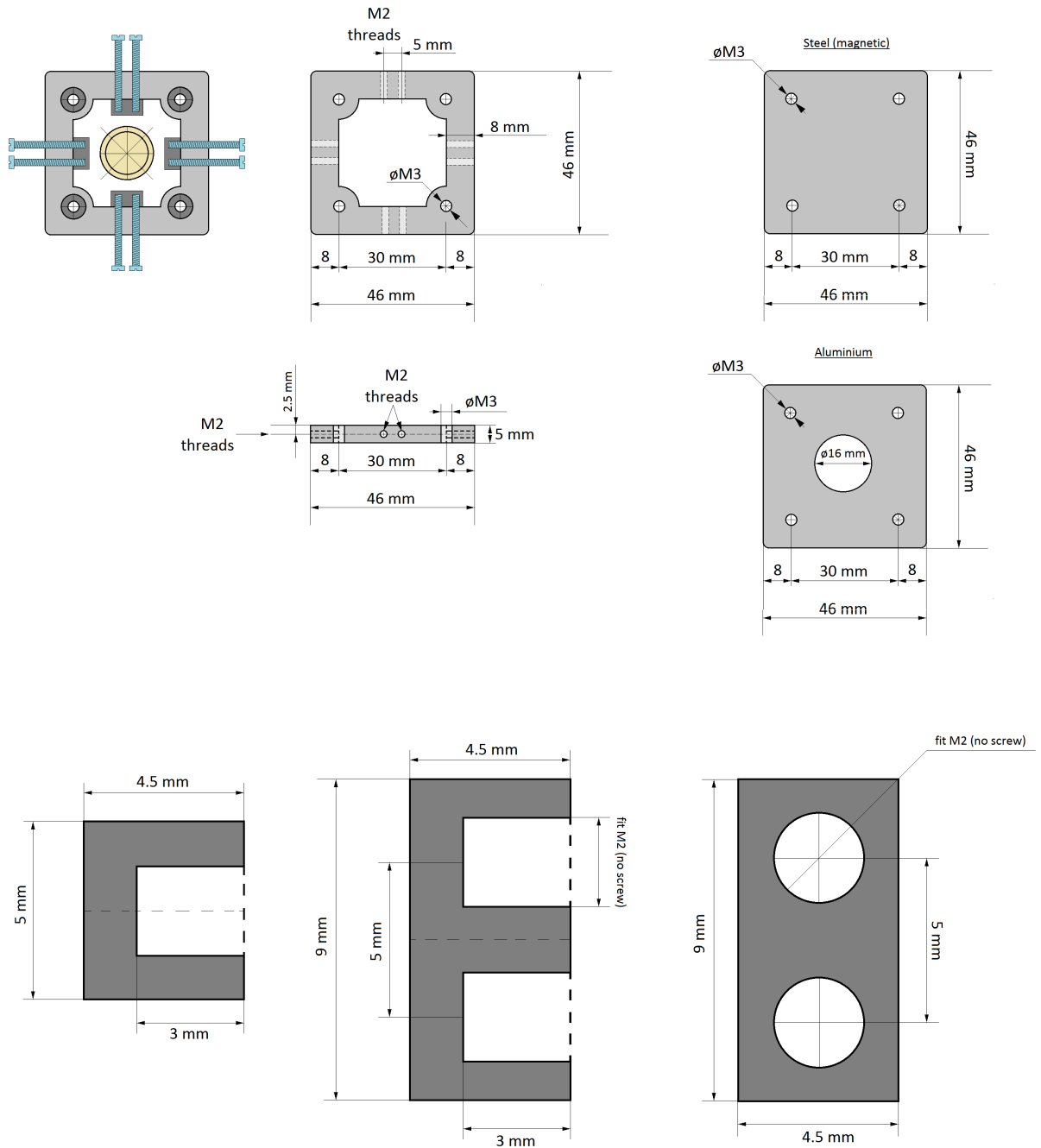


Figure 9.2. Layout of the sample stage designed for the experiment described in Chapter 5.

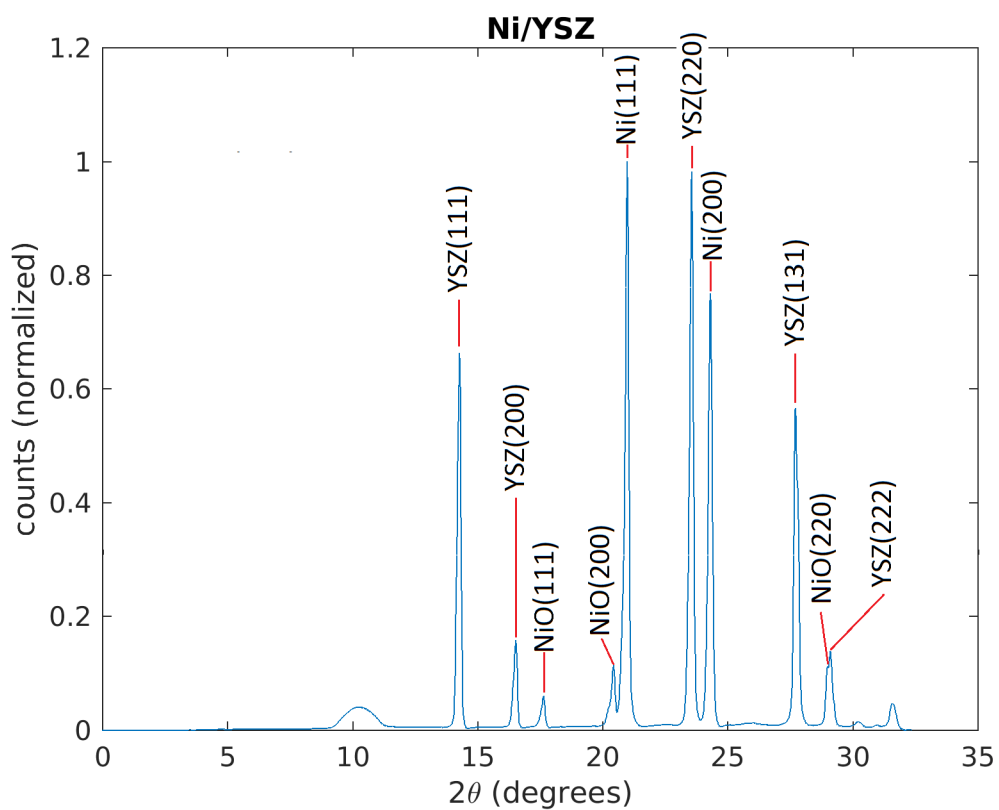


Figure 9.3. Diffraction pattern at the middle of the Ni/YSZ electrode before applying polarization. Notice a peak of the NiO, showing the existence of this phase before starting the polarization. This could mean that the Ni reduction from NiO was not fully achieved. Also EDS perform in this region shows the presence of oxygen in a large Ni grain, which support the idea of the existence of NiO phase in the electrode.

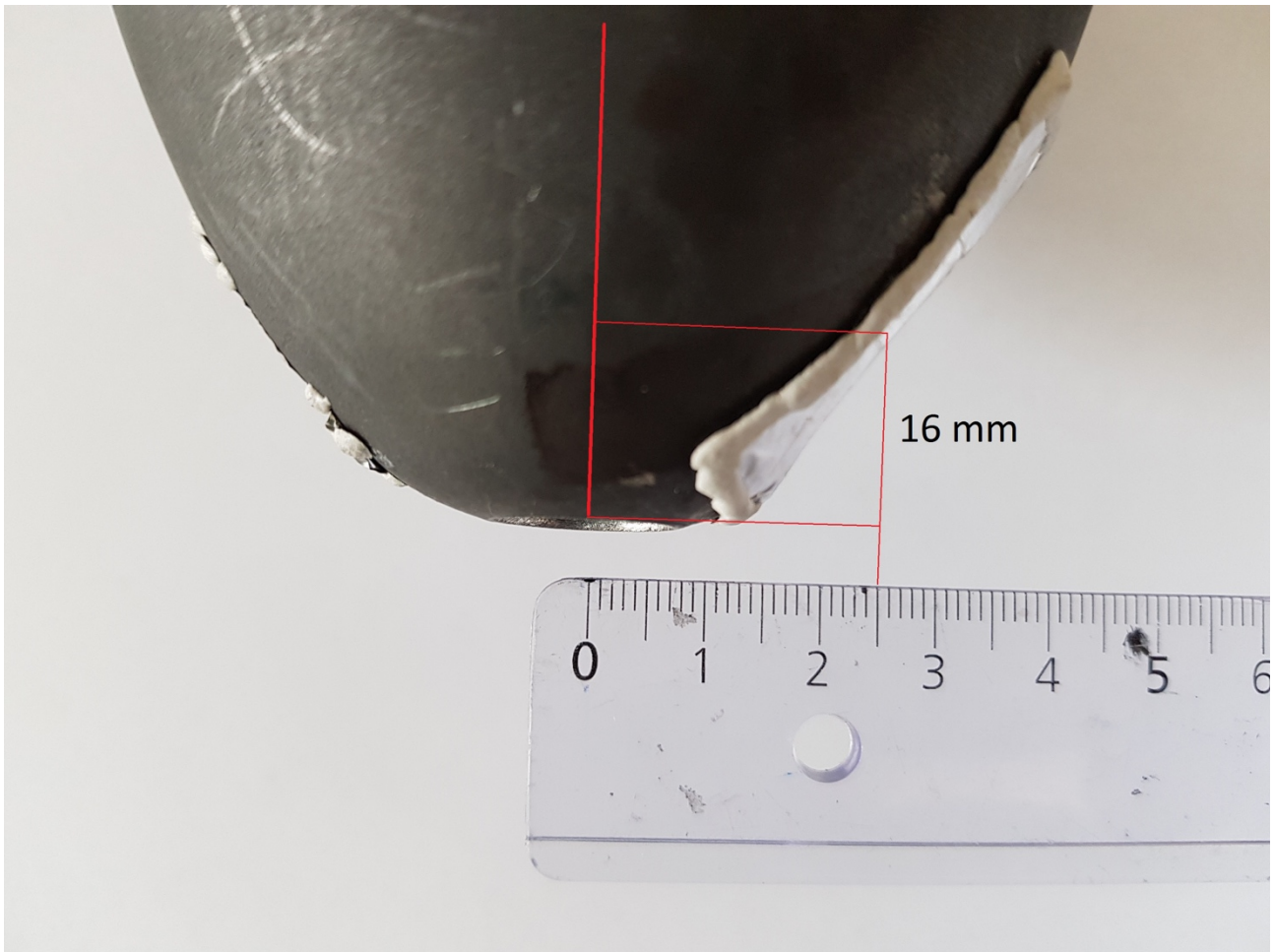


Figure 9.4. Estimation of the distance between the aluminium foil to the sample, based on the distance at which the sample was introduced inside the furnace.

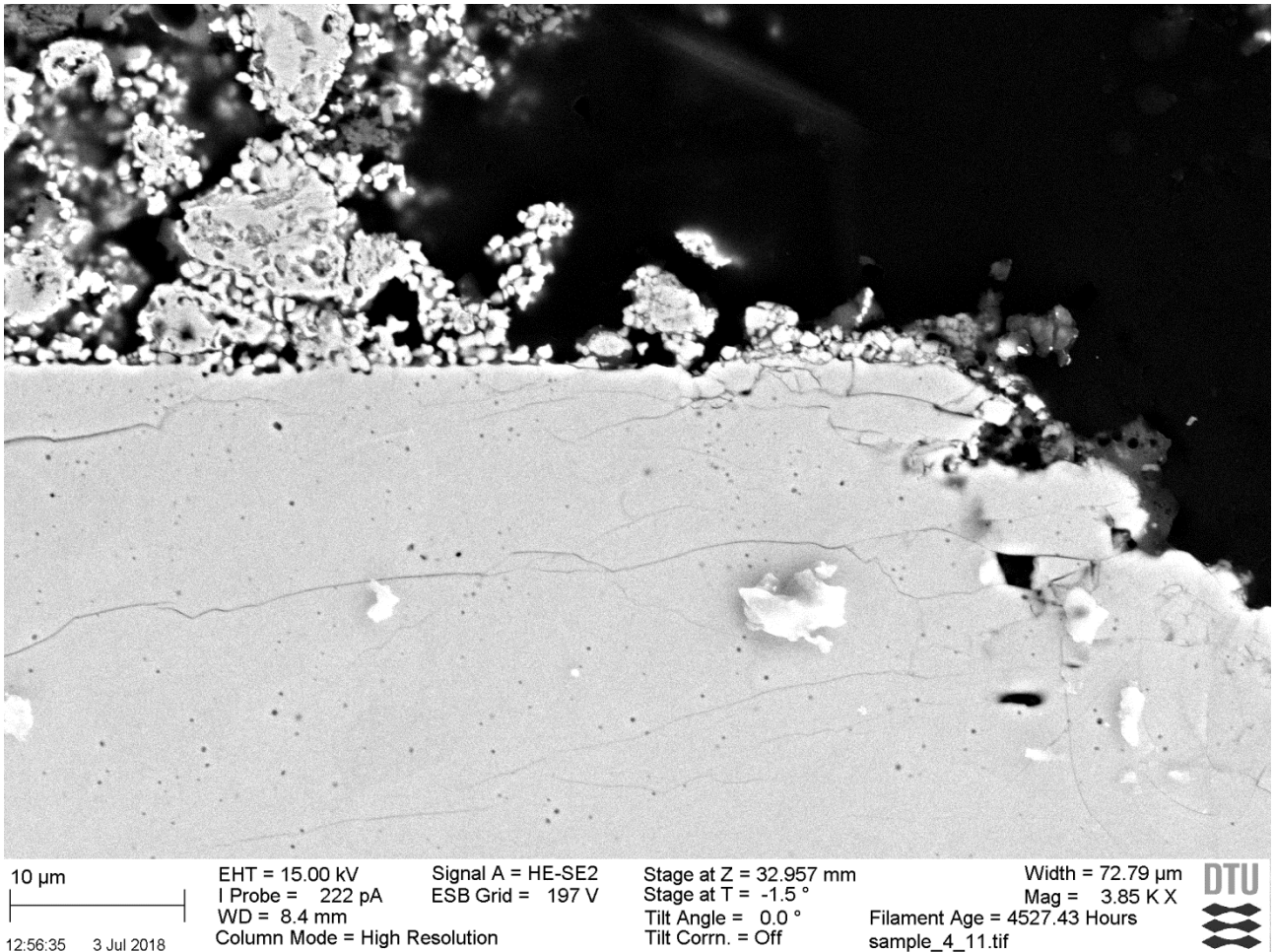


Figure 9.5. Cracks in the YSZ electrolyte close to the cathode interface. These cracks are believed to be caused by the removal of part of the sample during polishing.

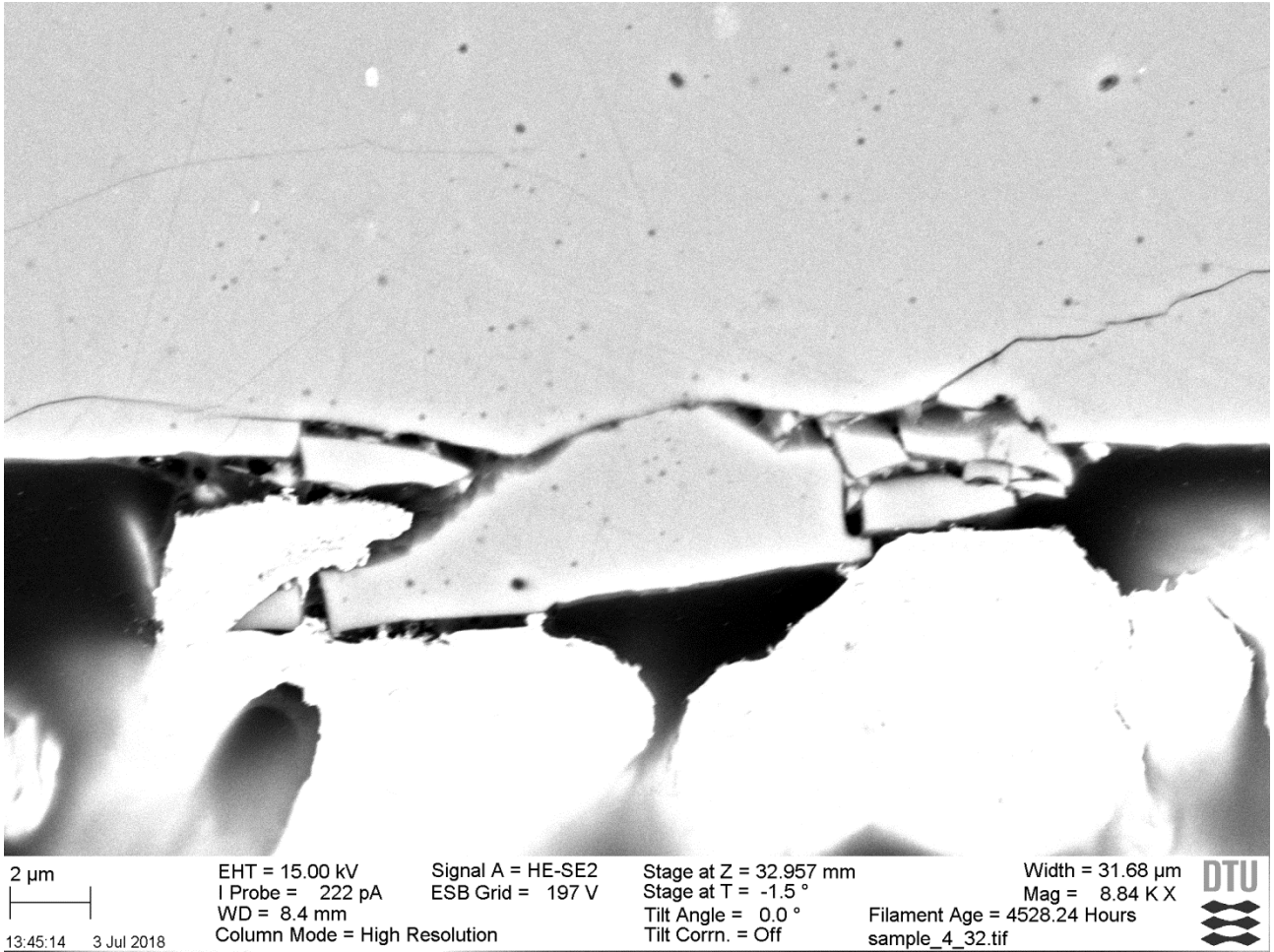


Figure 9.6. Cracks in the YSZ electrolyte close to the anode interface. These cracks are believed to be caused by the removal of part of the sample during polishing.

In-operando observation of microstructural evolution in a solid oxide cell electrolyte operating at high polarization

J. X. Sierra^a, H. F. Poulsen^b, P. S. Jørgensen^a, C. Detlefs^c, P. Cook^c, H. Simons^b, A. C. Jakobsen^b, J. R. Bowen^{*a}

^a Department of Energy Conversion and Storage, Technical University of Denmark, Frederiksborgvej 399, 4000 Roskilde, Denmark

^b Department of Physics, Technical University of Denmark, Anker Engélunds Vej 1 Bygning 101A, 2800 Kgs. Lyngby

^c European Synchrotron Radiation Facility, 71 Avenue des Martyrs, 38000 Grenoble, France

Abstract

In the present work a symmetric scandia yttria stabilized zirconia electrolyte based solid oxide cell is investigated *in-operando* by synchrotron X-ray diffraction as a function of time and position within the electrolyte while annealing at 700°C in air and at a polarization of 2 V. In addition, scanning electron microscopy experiments are carried out on similar cells operating at temperatures of 700, 800 and 900°C. Void formation in the grain boundaries of the electrolyte close to the anode/electrolyte interface is detected as early as 6 hours. No clear trend is observed with respect to cell operation time and temperature in cells with equal grain size. However, grain boundary surface area may be inversely related to the frequency of void observations. A decrease of d-spacing in the anode interface region can be attributed to compressive stress associated with oxygen pressure build up. Decrease of d-spacing in the cathode/electrolyte region could be associated to oxide ion deficiency. Dark field X-ray microscopy is used to map for the first time the strain gradients within an electrolyte grain close to the anode region. Changes in strain domains after 10.5 hours at operating conditions are assumed to be associated with early stages of void formation.

Keywords: solid oxide cell; strain; x-ray diffraction; grain boundary; nanoscale void formation

* Corresponding author: Jacob R. Bowen, jrbo@dtu.dk, +45 21 32 83 84

1. Introduction

Solid oxide cells (SOCs) have acquired increasing interest in energy production and storage applications because of their exceptional electrochemical and physical properties. SOCs can operate efficiently in two modes. In fuel cell mode (solid oxide fuel cell: SOFC) electrical energy is produced by electrochemical reactions involving oxygen and fuel (hydrogen and/or hydrocarbons), while in electrolysis mode (solid oxide electrolysis cell: SOEC) oxygen and hydrogen are produced from steam and/or carbon monoxide and oxygen from carbon dioxide, giving the possibility to store the chemicals for later energy production or chemical synthesis (1) (2) (3).

Due to the electrochemical reactions and the high operating temperature, SOCs exhibit degradation phenomena, which are detrimental to the cells performance and lifetime. In long-term experiments (on the order of hundreds to thousands of hours) severe degradation occurs under high current densities.

Knibbe et al. (4) discovered intergranular and transgranular fractures running along the yttria stabilized zirconia (YSZ) grain boundaries and the formation of pores in the grain boundaries of an YSZ electrolyte based cell. The fuel and oxygen electrodes, which are also known as cathode and anode respectively when running in electrolysis mode, consisted of Ni/YSZ and strontium doped lanthanum manganite/YSZ (LSM/YSZ) and the cell was tested at 850 °C for 188 hours under a current density of -2 A/cm^2 . It was concluded that the porosity is formed during operation at high current density. Energy dispersive X-ray spectroscopy (EDS) revealed the composition of the entrapped gas to be mainly oxygen. Similar pore formations and transgranular fractures were observed by Tietz et al. (5) after 9000 hours at a current density of -1 A/cm^2 in micrographs of fractured surfaces. The cell consisted of an 8%mol-YSZ electrolyte and a porous diffusion barrier layer of gadolinia doped ceria (CGO) with lanthanum strontium cobalt ferrite (LSCF) and Ni/YSZ as the oxygen and fuel electrodes respectively. Sun et al. (6) reported cracks, detachment and cavities close to the anode interface by scanning electron microscopy (SEM) in the polished cross-section of cells with similar electrode/electrolyte composition as in Knibbe et al. (4) after 900 hours at 850 °C and -1.5 A/cm^2 . Graves et al. (2) observed nanosized pores in YSZ electrolyte grain boundaries of a cell composed of Ni/YSZ and LSM/YSZ electrodes, by scanning transmission electron microscopy, after 420 hours in electrolysis mode at 800 °C and -1 A/cm^2 .

It is suggested that this formation of porosity in the grain boundaries of the electrolyte close to the electrolyte/oxygen electrode interface is due to an increase in oxygen activity, caused by the distribution of the electromotive potential and resulting in a high internal oxygen pressure build up

in this region (4) (7) (8). An oxygen partial pressure on the order of 10 MPa has been proposed by Virkar (9), based on brittle materials properties, to cause delamination of the anode at typical temperatures of 800 °C. Therefore, we expect the high oxygen pressure to result in compressive stresses and thus a reduction of electrolyte lattice parameter close to the anode interface.

In order to increase the efficiency of the cell, YSZ electrolytes are commonly co-doped with scandia ($\text{Sc}_2\text{O}_3 - \text{Y}_2\text{O}_3 - \text{Zr}_2\text{O}_3$, ScYSZ) as ScYSZ provides a larger ionic conductivity than YSZ for equivalent temperature (10) (11). Thus, reduction of operating temperatures by 100-200°C is enabled. This in turn improves the degradation behavior of other SOC stack components and reduces mechanical issues associated with thermal expansion mismatches and chemical instabilities (12) (13) (14). To our knowledge, pore formation as observed above in YSZ electrolytes has not been reported for scandia-yttria stabilized zirconia electrolytes in electrolysis mode.

Resolving the cause of the void formation has been hampered by a lack of methods to directly observe the microstructure evolution at the nanometer scale, within the relevant deeply embedded region and during operation of the cell. Thus, here we take advantage of recent advances in synchrotron X-ray diffraction techniques to present a novel in-operando investigation of microstructure evolution within the bulk of ScYSZ electrolyte based symmetrical SOC under high polarization. Changes in lattice parameter across the cell are determined by local X-ray diffraction as a function of depth from electrode interfaces and dark field X-ray microscopy (DFXRM) (15) (16) is used to map internal strain gradients within individual electrolyte grains.

2. Experimental

2.1. Cell design

Symmetric cells were produced with the electrolyte consisting of $(\text{Y}_2\text{O}_3)_{0.01}(\text{Sc}_2\text{O}_3)_{0.10}(\text{ZrO}_2)_{0.89}$ (henceforth denoted ScYSZ) provided by Daiichi Kigenso Kagaku Kogyo Co., LTD. Prepared by tape casting these have an approximate thickness of 180 μm . One half of the ScYSZ sheet was thermally treated at 1600 °C for 1 hour and the other half was left with no thermal treatment. The larger grains of the thermally treated samples allows studying the size dependency of the void formation and results in a suitable grain size for the *in-operando* synchrotron experiments. A 50/50% slurry of LSM/YSZ was sprayed on both sides of each sheet as electrodes, thereby creating a symmetrical cell, suitable for testing at high temperature in air. The cells were then sintered at 600 °C for 4 hours and 1300 °C for 6 hours, with a cooling rate of 60 °C/hour, achieving an electrode thickness of 5-10 μm . Rectangular pieces with dimensions specified in the following sections were

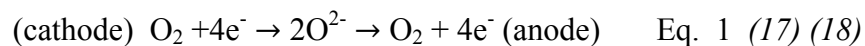
cut using a diamond blade wheel (Minitom, Struers A/S). To ensure electronic conductivity, platinum cables with a 2 mm flattened tip were bonded to the electrodes with platinum paste. To hold all components together an Aron Ceramic, class D inorganic adhesive paste was used. Approximately half of the cell was left exposed to the furnace air atmosphere as the active part.

Two types of experiments were performed. 1) Void statistics experiments, where cells were tested for a specific duration and condition after which their internal structure was examined. 2) *In-operando*, where the structure of grains was probed over time with synchrotron X-rays. A similar sample setup was utilized for both types of experiments primarily dictated by the constraints of the synchrotron experiment, i.e. small cell size, large grain size, atmospheric air gas environment and high polarization to accelerate degradation processes to be detectable within the beamtime duration.

2.2. Void statistics experiments

Samples with dimensions $1.6 \times 5 \text{ mm}^2$ were tested in atmospheric air at 700, 800, and 900 °C. A fixed potential of 2 V was applied for durations of 6 to 48 hours and 6 to 72 hours for thermally treated and non-thermally treated ScYSZ electrolyte based cells respectively. The experiments were carried out in an alumina tube furnace and the cells were placed at a maximum of 15 mm from the thermocouple. The cells were then fractured *post-mortem* close to the interface of the active region and the ceramic paste to perform scanning electron microscopy (SEM) (see §2.4 for details).

According to this configuration, the cell acts as an electrochemical oxygen pump. Oxygen reduction occurs at the cathode/electrolyte interface, oxide ions then conduct through the electrolyte driven by the potential difference at the electrodes, reaching the anode where they are released as oxygen molecules. The overall equation is given by:



2.3. In-operando experiment

2.3.1. Cell characterization

The *in-operando* cell was made using the same procedure as described in the cell design but with dimension 0.33x4x0.18 mm, (see Figure S1 in supplementary material) in directions “x”, “y” and “z” respectively, with reference to the coordinate system in Figure 1.

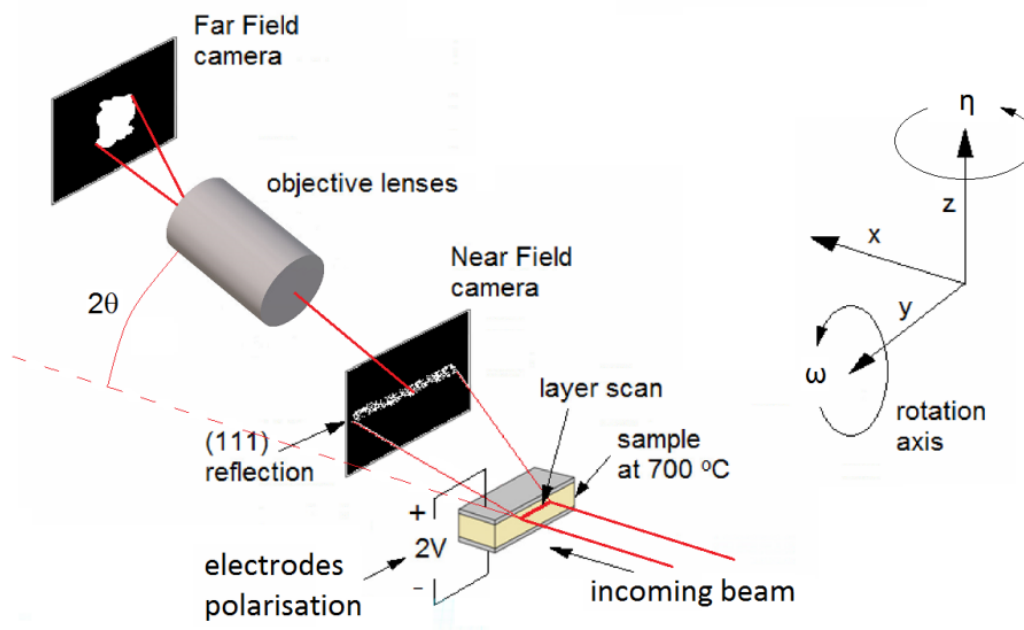


Figure 1. Schematic view of the sample setup at beamline ID06 (furnace is not included). The near field camera can be translated out of the diffracted beam enabling dark field microscopy by means of an X-ray objective.

The experiment took place at the ESRF beamline ID06 using 17 keV X-rays. The cross-section of the incident beam was defined by a silicon condenser – a compound refractive lens – with a resulting FWHM of 350x17 μm in “y” and “z” directions respectively. The cell was electrochemically operated (*in-operando*) in air at 700 °C for a total of 32 hours. It was scanned repeatedly with respect to the beam in the “z” direction in 51 steps covering a range of 0.25 mm, henceforth referred to as a layer scan. The top and bottom of the cell were identified from the absence of the diffracted signal outside the sample. The experimental geometry is sketched in Figure 1. The goniometer allows rotations around both the y- and z-axis. The diffraction signal from ScYSZ (111) was studied using alternately a near field camera and a dark field microscope using a far field camera.

A hot air gas blower with a nominal maximum temperature of 1000 °C was used to provide the high temperature to the cell. The temperature was raised from room temperature to the maximum in approximately 5 hours. Due to the limitations of the furnace-detector geometry, the sample was placed a few millimeters away from the hottest part of the furnace, to allow detection of the (111) diffraction line. Thus, the temperature of the sample was 700 °C, estimated by a thermocouple placed approximately 2 mm away from the sample. The temperature calibration was done as follows. First, the thermocouple was placed in analogous position of the cell by using the same sample holder. Second, the thermocouple was moved 2 mm away to allow the temperature difference to be measured. Finally, the *in-operando* experiment temperature was estimated considering that difference previously measured with the thermocouple at 2 mm from the cell.

After the temperature had stabilized at 700 °C the voltage was set to 2.0 V across the cell. The time of the last layer scan performed was 24.7 h after applying the voltage and the total exposure time at operating conditions was 32 hours. Collection of diffraction data after the 24.7 h measurement was not experimentally possible due to failure in the data acquisition system.

During the high temperature part of the experiment five stages were defined as follows, excluding the room temperature stage as the starting point of the experiment:

- 0V: no applied voltage
- XXh@2V: applied voltage of 2 V for XX hours. XX values are: 0.0, 2.4, 17.0 and 24.7.

After the *in-operando* experiment void formation was investigated by post-mortem SEM on fractured and polished cross-sections (see §2.4).

2.3.2. Near field set-up

The near field set-up involves a FreLoN camera coupled to a scintillator screen, with a resulting effective pixel size of 0.622 μm and 2048x2048 pixels. Placed at a distance of 50 mm from the sample in “x”, a segment of the (111) Debye-Scherrer ring is observed. An example of a raw image can be seen in Figure S2 in the supplementary material. The grains in the illuminated volume give rise to distinct diffraction spots. These are sampled while performing a continuous scan in ω , with a range of 4° in steps of 0.01°. From the center-of-mass position of the spots on the detector we can derive statistics of grain average properties, in particular grain volume, and the average axial strain within a grain (19). From the width of the peaks in the y-direction on the detector and in angle ω , we can determine the mosaic spread of the associated grain.

The near field data was analyzed using the program: “peaksearch” in Fable (20). A background was subtracted from all images. This was defined for each pixel as the median value over 10 subsequent images. The filtering rejected peaks with less than 5 pixels, saturated pixels, and peaks

associated with low integrated intensity and a mosaicity lower than twice the ω step, in order to remove noise and uncertainties in the center of mass position in the images. The average d-spacing of the (111) was estimated by the positions of the filtered peaks in the “z” direction of the near field images at all “ ω ” of each layer.

2.3.3. Dark field set-up

The *dark field microscope set-up* allows mapping of the structure and strain within selected grains. A compound refractive lens composed of 70 beryllium lenses was placed between the sample and the detector. Suitably aligned this acts as an objective, magnifying the projection of a given grain by 16 times. The far field camera was a FreLoN camera coupled to a scintillator screen, with a resulting effective pixel size of 1.4 μm and 2048x2048 pixels. The resulting theoretical spatial resolution of the dark field set-up was approximately 300 nm (21). By tilting the sample in ω and η within the estimated mosaicity range, maps can be made of the orientation gradient within the grain. By scanning the scattering angle 2θ (see Figure 1) the local axial strain component is probed (21). To integrate over the rocking curve during acquisition in such a strain scan the sample was continuously rotated (rocked) over a ± 0.05 range in ω . The data analysis followed the procedure presented by Ahl et al. (22).

2.4. Electron microscopy

A Carl Zeiss SUPRA-35 Gemini FEGSEM scanning electron microscope at an accelerating voltage of 2 kV was used to observe the morphology of the *post-mortem* fractured sample using the secondary electron detector SE2 (Everhart-Thornley). The approximate width of images was 20.5 μm .

Polished cross-sections were also imaged at 2 kV and EDS analysis was carried out at 29 kV to avoid yttrium and zirconium *k*-alpha peak overlap using a ThermoFisher Noran System 6 EDS detector.

3. Results

The measure of the average electrolyte grain size was determined by the linear intercept length method (23) from five SEM images of separated sections of each bulk sample, after applying thermal etching at 1400 °C for 10 minutes, giving 6.3 ± 1.8 and 12.8 ± 4.1 μm (± 1 standard deviation) for pristine and thermally treated ScYSZ electrolyte respectively. For simplicity, cells based on

these electrolytes are forthwith referred to as 6 μm -ScYSZ and 13 μm -ScYSZ respectively and the *in-operando* cell described in §2.2 denoted 13 μm -ScYSZ-op.

Since it is difficult to quantify the effect of the alumina paste and Pt collectors surrounding half of the *in-operando* cell, we consider the active region of the cell the zone that is exposed to the open air. With this consideration the average current density is estimated to be $1.0 \pm 0.2 \text{ A/cm}^2$, which is on the order of current densities necessary to initiate void formation reported in the literature (2) (5).

Two representative examples of void formation on cleaved grain boundaries are shown in Figure 2 for the 13 and 6 μm grain size electrolytes. The structures have a similar appearance as to those reported in the literature, where the void size ranges from a few to approximately 100 nm (5) (24) (4). For comparison, a sample subjected to 850 °C for 72 hours with no potential difference between electrodes was taken as a reference showing no void formation. A representative image is shown in Figure S3 a) in Supplementary Material. Moreover, no void formation was found in any of the cathode/electrolyte interfaces of the samples subjected to a polarization of 2 V, a representative image is shown in Figure S3 b) in Supplementary Material.

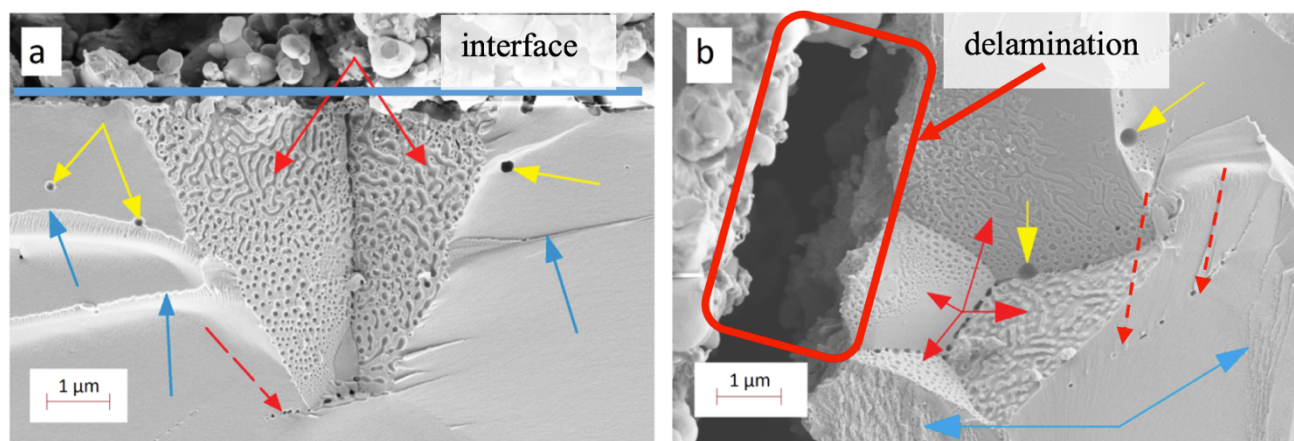


Figure 2. Examples of void formation indicated by red arrows, mainly in the grain boundaries of a) 13 μm -ScYSZ at 900 °C for 12 hours and b) 6 μm -ScYSZ at 900 °C for 72 hours. The anode/electrolyte interface in a) is indicated by the horizontal blue line and a delamination of the anode can be observed in b) indicated by the red box. Blue arrows indicate intra-grain structures when fracturing the sample, yellow arrows indicate intrinsic pinholes and dashed red arrows indicate void formation that could possibly be on a plane non-parallel to the fractured surface.

Regions pointed out by blue arrows in Figure 2 indicate surfaces where the fracture surface passes through grain interiors (intra-granular fracture) during the sample preparation. These fracture

surfaces contain features typical of fracture in low toughness materials. No extended surface areas of void formation were found in these regions, only lines of voids (dashed red arrows) were observed. These, “pearl-on-a-string” voids decorate grain boundaries oriented approximately orthogonal to the SEM images and represent a cross-section of the void patterns indicated by the red arrows on cleaved grain boundaries. Extensive void formation indicated by the red arrows corresponds to regions where the fracture path has followed grain boundaries weakened by void formation. Yellow arrows correspond to pre-existing pinholes and are identified by different characteristics compared to void clusters. For example, pinholes were observed randomly inside grains and on grain boundaries, their size, in many cases is significantly larger than the observed voids and are more isolated in a similar manner to untested material.

Void formation was also observed adjacent to edges of pinholes and at intragranular cracks, as observed in Figure 3. Also in typical surveyed images, with pixel size of 10 nm, the smallest individual voids that can be distinguished are estimated to be between 20-30 nm, however, occurrences of voids were only quantified when observed as an agglomeration of voids. Isolated voids were not considered significant. An example of the smallest voids is shown in Figure S6. These observations of voids close to pinholes, cracks and in the majority of the cases on grain boundaries may suggest that these defects can act as nucleation sites for voids.

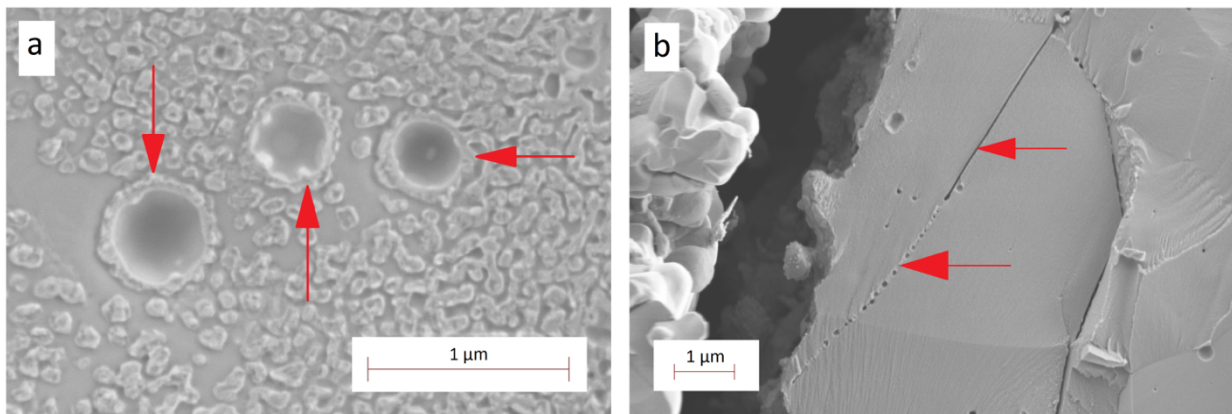


Figure 3. Void formation found in 6µm-ScYSZ at 900 °C for 72 hours a) surrounding intrinsic pinholes and b) continuing a crack in the electrolyte material, indicated by the red arrows.

3.1. Cavity formation close to the anode/electrolyte interface

Figure 4 shows the results of the SEM analysis of the void statistics experiments in terms of the ratio between the number of images with observed void formation and the total images along the interface for each case (denoted in the figure as the ratio of images), and their maximum observed electrolyte depth below the anode/electrolyte interface at different test durations and temperatures.

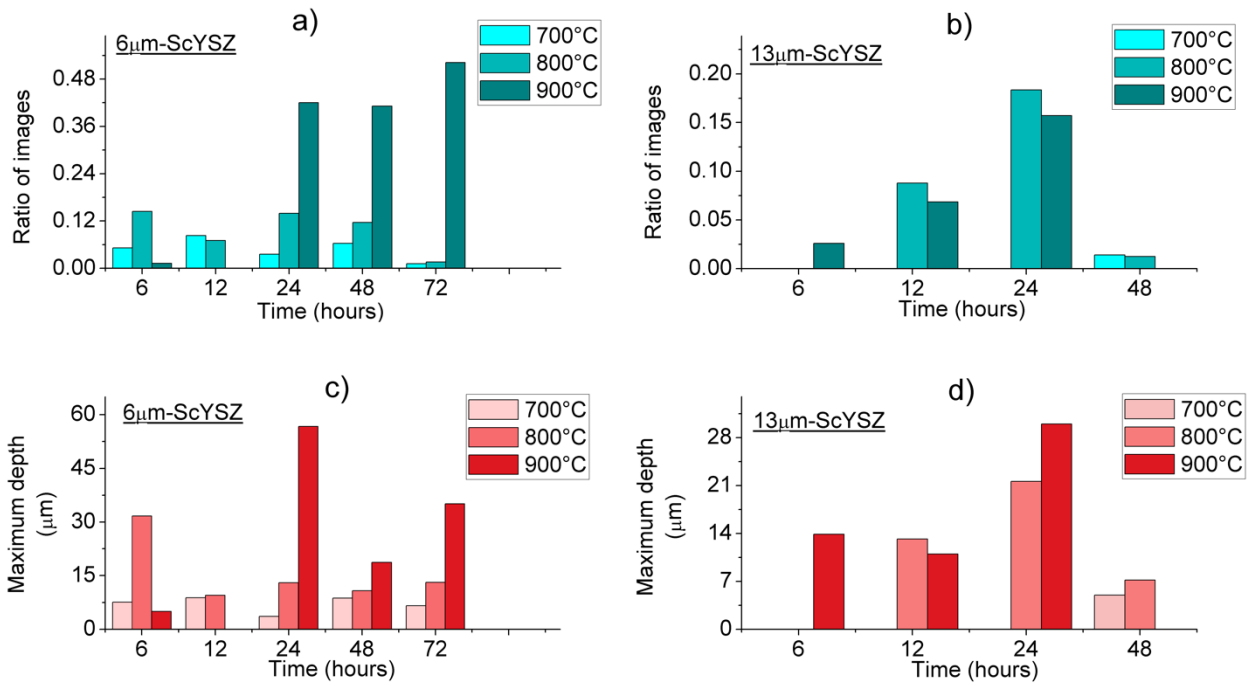


Figure 4. Statistics of void formation in ScYSZ. Column bars in a) and b) indicate the ratio of images where the void formation was observed for 6µm-ScYSZ and 13µm-ScYSZ respectively. Column bars in c) and d) indicate the maximum depth at which voids were found below the anode/electrolyte interface.

Note that the cells were tested in the full range of temperatures and durations. Therefore, a missing bar indicates a tested cell where no images containing void formation were recorded. In the cases with most occurrences, the ratio of images with voids is close to 50%, so void formation should not be considered a rare event in general.

As shown in Figure 4 a) for 6µm-ScYSZ cavity formation was observed after all tests and temperatures, with exceptions of 900 °C for 12 hours. In the cells subjected to an applied potential for 24 to 72 hours the occurrences of void formation, in general, increases with the temperature at each equivalent time. Only at 72 hours, the ratio of images remains practically the same at 700 and 800 °C, but then increases at 900 °C to a value consistent to what is observed at 24 and 48 hours. No clear trend was observed in this case for different operando times at the same temperature. A different scenario is observed in the case of the 13µm-ScYSZ cells, in Figure 4 b) where it appears that the larger grain size delays the onset of void formation at the lowest temperature of 700 °C. From Figure 4 it can be seen that statistics derived from quantifying void formation under optimized imaging conditions is limited by the stochastic nature of fracture surfaces between samples.

In Figure 4 c) for 6 μm -ScYSZ the maximum depth where voids were found below the anode/electrolyte interface shows an increase with temperature at each equivalent time: 24, 48 and 72 hours, while no clear relation is observed at 6 and 12 hours. In Figure 4 d) there is no observable correlation for 13 μm -ScYSZ regarding time and maximum depth in the cells; discussion of the observed poorer statistics of this case, compared to 6 μm -ScYSZ, is given later.

It also should be noted that the detection of voids by SEM is dependent on the local fracture path during *post-mortem* sample preparation and the lack of detection is not necessarily an absolute verification of absence of cavities. Several inconsistencies in the trends of number of images and maximum observed depth can be observed in Figure 4. We attribute this scatter to hidden variables. Although great care was taken in following the same protocol by the same person for testing and sample preparation, some variables such as slight differences in the fracturing method could have affected some of the observations. This means that the confidence level in reporting the presence of void formation is significantly higher than in reporting its absence. More work is necessary in order to improve statistics of void observation and thus determine more rigorously the presence/absence of void formation and more reliable incubation periods. An alternative method to quantify void formation is to examine the cross-section of samples after mechanical polishing. Measuring microstructural features on polished planar cross-sections provides stereologically correct quantification features (25), in our case void number density per cubic micrometer. However due to the scale of the voids it is our experience that mechanical polishing obscures the majority of voids due to mechanical damage.

3.2. *In-operando study of grain-averaged electrolyte lattice parameter change*

In Figure 5 the evolution of the average d-spacing is shown as a function of distance from the positive electrode, with reference to the cell at 700 °C and no applied voltage (black horizontal line at 0 relative d-spacing). The various lines represent the different combinations of applied voltage and electrochemical operation time. The location of the vertical dash-dotted lines delimit the anode and cathode / electrolyte interfaces as determined by the number of diffraction spots on the detector as the 17 μm FWHM line beam was scanned across the cell edge. The complete graph, including standard deviations of the d-spacings and absolute d-spacing is shown in Figure S5 of supplementary material.

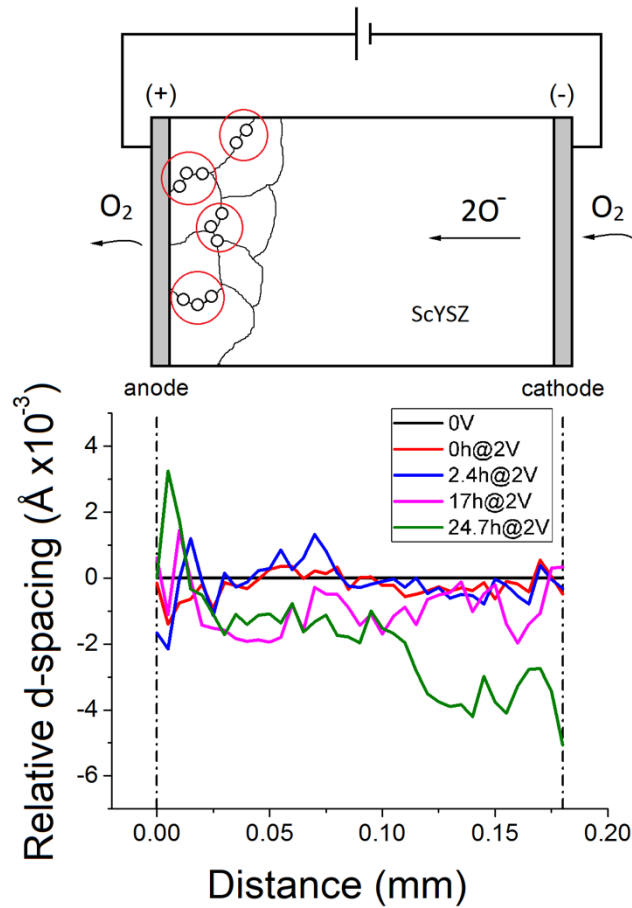


Figure 5. In-operando study. Top: a schematic view of the electrochemical cell setup with the expected oxygen void formation close to the anode. Irregular black lines and small black circles are representations of grain boundaries and void formation, marked with red circles. Bottom: evolution of d-spacing as a function of distance from the positive electrode relative to the reference condition, at 700 °C and 0 V (black horizontal line).

Within statistical uncertainty, there is no immediate change in d-spacing when applying the voltage, as evidenced by the black and red lines in Figure 5. The d-spacing did not change significantly during the first 2.4 hours either, see blue line. After 17 hours a decrease of d-spacing in the order of $1\text{-}2 \times 10^{-3} \text{ \AA}$, relative to the previous stage, was observed in the region from the electrolyte/anode interface to the middle of the electrolyte. However, an even more distinct change in d-spacing was observed at 24 hours, see green line, with a strong decrease of d-spacing towards the cathode/electrolyte region in the order of $4 \times 10^{-3} \text{ \AA}$. The fluctuations within the first 0.015 mm of the electrolyte from both electrode/electrolyte interfaces can be attributed to the geometry of the

cell, the beam width, and a relatively poor grain statistic. A more stable behavior was observed close to the cathode/electrolyte interface.

3.3. In-operando mapping of the strain evolution within a ScYSZ grain

To investigate the feasibility of mapping changes in the internal strain within a grain during cell operation, one average sized grain was selected and subjected to dark field microscopy at regular intervals during the annealing in the *in-operando* experiment. This grain was located less than 25 μm from the anode/electrolyte interface. By combined translation/rotation of the objective and a translation of the detector (see Figure 1) we effectively scanned the scattering angle 2θ around its nominal position of 14.186° within a range of $\pm 0.05^\circ$. In this way, maps of the axial strain were provided (22). These maps are 2D projections of the grain, as the beam height is larger than the grain size. Shown in Figure 6 are strain maps acquired initially – at room temperature – and after 10.5 hours of operation at 2 V.

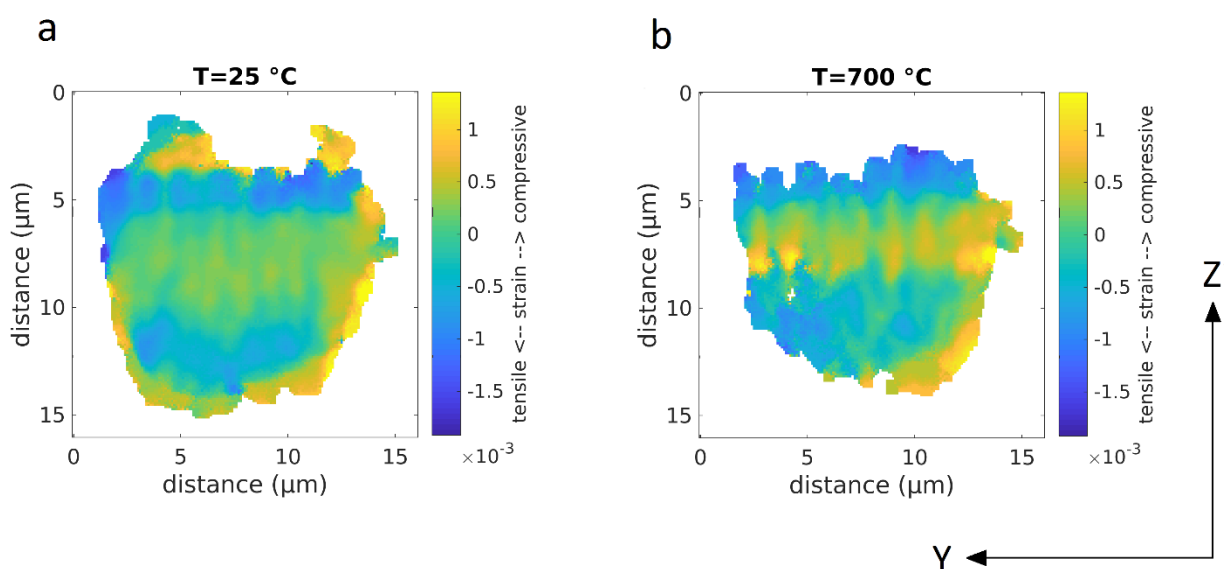


Figure 6. Strain maps of a single grain close to the anode/electrolyte interface. Positive and negative values imply compressive and tensile strain respectively. a) Grain at room temperature and no applied voltage. b) The same grain at 700 °C and 2 V polarization after 10.5 hours at operating conditions. The anode/electrolyte interface is above the image. The “y” axis is defined in Figure 1 while the z' -axis represents the axis perpendicular to the 2θ direction and the “y” axis. The pixel size is 0.1 μm and the color bars have the same scale.

At initial conditions, regions with compressive strain in the order of 1×10^{-3} and larger are localized mostly close to the grain exterior. Regions with strain between 0.5×10^{-3} and -0.5×10^{-3} are distributed inside the grain. After 10.5 hours, an increase of local compressive strain in the central regions from approximately 0.7×10^{-3} to more than 1×10^{-3} is observed.

3.4. Characterization of grain boundary void formation after operation

A *post-mortem* analysis of the $13 \mu\text{m}$ -ScYSZ-op cell by SEM is shown in Figure 7. It reveals void formation in the grain boundaries of the electrolyte close to the anode/electrolyte interface. These appear at a maximum depth into the electrolyte from the anode/electrolyte interface of approximately $10 \mu\text{m}$, similar to the range observed in the $13 \mu\text{m}$ -ScYSZ *post-mortem* sample as shown in Figure 4.

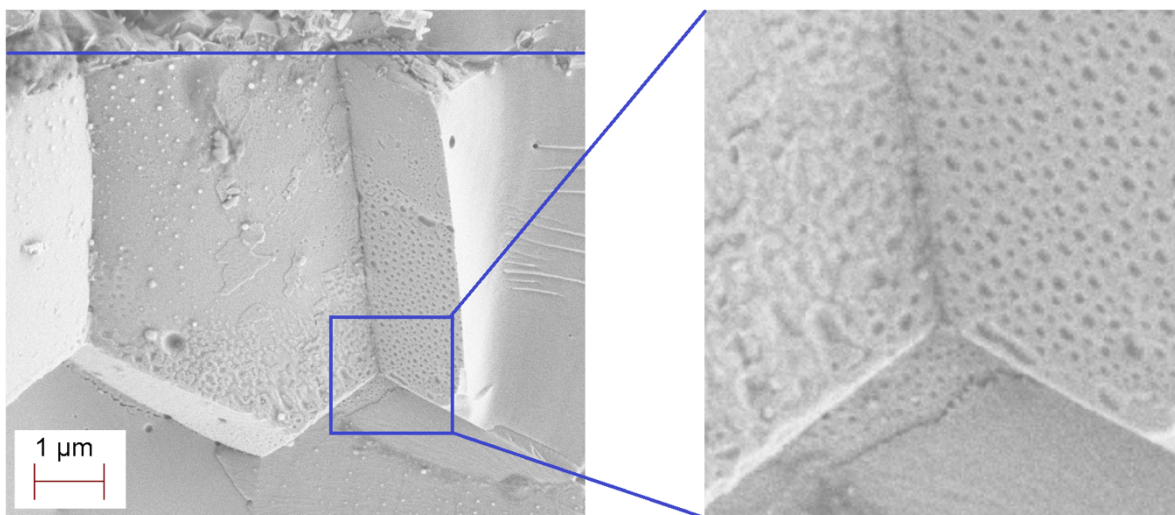


Figure 7. SEM micrographs of the fractured $13 \mu\text{m}$ -ScYSZ-op revealing void formation in the electrolyte near the anode/electrolyte interface. The blue horizontal line marks the interface between electrolyte (below) and anode (above). To the right a 4.2X magnified image of the area indicated by the blue box is shown.

4. Discussion

4.1. Conditions and factors influencing void formation

The present work, as illustrated in Figure 4 shows that under realistic operating conditions at high polarization, electrolyte grain boundary void formation onset commences within a few hours and is relatively independent of typical operation temperatures. In the case of $6 \mu\text{m}$ -ScYSZ the incubation period appears to be shorter than 6 hours at all three temperatures. The presence/absence of void

formation for 13 μ m-ScYSZ, in comparison to 6 μ m-ScYSZ where voids are present for all conditions, suggests that the grain size has an effect on the incubation period, as there appears to be a great absence of voids at the lower temperatures. An analogous hypothesis of an incubation period is also supported by Graves et al. (2), in which a YSZ cell with Ni-YSZ and LSM/YSZ as fuel and oxygen electrodes respectively was reversibly tested at 800°C, in cycles of electrolysis and fuel cell mode every 5 hours each under a current density of -1/+0.5 A/cm² respectively. This treatment limited the cell voltage to 1.33 V in electrolysis mode in comparison to a cell run at equivalent electrolysis conditions where the cell voltage climbed steadily to 1.73V in over 400 h. No significant degradation occurred in cycling mode, with no void observation after hundreds of hours of test. For the cell at constant current, void formation was observed under continual electrolysis operation after reaching high values of cell potential. This suggests that an incubation period exists in which the critical level of high internal oxygen pressure is not reached and oxygen pore formation can be avoided by maintaining a low cell voltage. Alternatively, if void formation occurs, it is hypothesized by Graves et al. (2) that in the fuel cell mode voids can be removed by pumping the oxygen, when the pO_2 is lowered. However, no microstructural evidence is provided, establishing that either void formation occurs continuously with increasing cell voltage or that a limiting cell voltage for void formation initiation exists. Furthermore, no evidence exists to our knowledge that once a void is formed for a given cell voltage that void can be removed again.

To our knowledge, void formation has previously only been reported for YSZ (5) (2) (4). The present work reveals that void formation occurs under similar operating conditions and with a similar morphology in ScYSZ. Moreover, the incubation time is shown to be as short as 6 hours, comparable to what was observed by Graves et al. (2). Consistent void formation in both these materials thus suggests that the stabilizing dopant Y₂O₃ / Sc₂O₃ does not have a significant effect on void formation based on our available results. A systematic study exploring varying dopant ionic conductivity is therefore needed to establish dopant effects on the evolution of void formation.

The higher occurrence of void observations in 6 μ m-ScYSZ in comparison to 13 μ m-ScYSZ in the addressed temperature and time range may suggest a dependence of this effect on the grain size, and thus the grain boundary specific interface area. This, in addition to the observation of voids close to pinholes and cracks, may suggest that reducing and/or eliminating these defects and reducing the grain boundary interface area could be a mitigation mechanism to reduce the nano-sized void formation, thus increasing the lifetime of the cell.

Void formation is believed to be caused by a build-up of oxygen pressure due to the distribution of electrochemical potential inside the electrolyte (4) (5) (7). Kim et al. (26) suggested that the detected presence of La, Sr and Mn impurities along the grain boundaries of YSZ by EDS could be

considered as a sink to release electrons from the oxide ions, where oxygen gas builds up, thus resulting in high oxygen gas pressure at grain boundaries and intergranular fracture. However, diffusion of these elements into the ScYSZ was not detected in our case, based on the sensitivity of our EDS analyses.

4.2. Microstructural changes close to the anode/electrolyte interface

As shown in Figure 7, the *in-operando* cell 13 μ m-ScYSZ-op, shows void formation after 32 hours. As we evidently have no similar analysis at shorter times, we cannot prove the existence of void formation at earlier times. However, the decrease of d-spacing at 17h@2V and 24.7h@2V (see Figure 5) indicates an increase of compressive stress at the anode side. Assuming that all changes in lattice parameter are stress induced, using a Young's Modulus of 158 GPa for 6mol%ScYSZ at 700 °C (27), the axial stress is up to 100 MPa within the first 100 μ m of the electrolyte for the 24.7 hour case (see also Figure S6 in supplementary material). This value of stress estimated above is one order of magnitude larger than the 10 MPa predicted by Virkar et al. (9) to be sufficient to cause delamination of the anode, although no void formation is mentioned in that study. In the present study both delamination and voids were observed only in the SEM images related to the most extreme case: 6 μ m-ScYSZ at 900 °C for 72 hours. Analogous delamination have been observed by Chen et al. (28) in cells composed by LSM electrodes and YSZ electrolyte under current densities of 0.5 A/cm² in electrolysis mode at 800 °C in air, with an increase of anodic polarization potential from 1.12 to 1.73 V, where a proposed mechanism of this effect is also described.

The maximum depth at which voids were detected in this cell was approximately 13 μ m. Considering the uncertainty of the d-spacing near the anode/electrolyte interface and the validity of the assumption above we are unable to establish an explicit correlation between the void formation depth and stress magnitude.

4.2.1. Local strain within a grain

The unique x-ray microscopy results presented in Figure 6 demonstrate the feasibility of *in operando* mapping of the individual grains. The increase of local strain areas in Figure 6 b) is consistent with an increase of the overall strain of the grains close to the anode/electrolyte interface as evidenced by Figure 5. We interpret the changes between the left and the right figure as indicative of strain localization at the grain boundaries: the pre-cursor of the pore formation. More specifically:

- The morphology of the grain projection is not the same in the two maps in Figure 6. In particular, some areas are missing in the outer parts of the treated grain where these locations no longer locally meet the Bragg condition. This indicates that these zones either experience: a) local crystal rotation greater than the $\pm 0.05^\circ$ rotation in rocking angle performed during each scan and/or b) extremely high axial strain corresponding to variations in the lattice parameter of $\Delta 2\theta > 0.05^\circ$, i.e. on the order of $\pm 35 \times 10^{-3}$ or larger. However, elastic axial strains at these extremes are unlikely as they correspond to stresses on the order of 5 GPa and would thus either result in fracture, or local lattice rotation consistent with a). In other words, regions at the grain boundaries are experiencing significant local deformation. Kim et al. (26) reported complete separation of grain regions as intergranular cracks in a YSZ electrolyte operated at 750 °C for 120 hours in air under high current density. It should be noted that the outer shape of the grain and values of inner strain may be influenced by the chosen level of background intensity, which is selected visually by setting a suitable value to remove single and weak pixels without removing what appears to be the grain. However, in our case the same procedure is applied in both images.
- The horizontal band with nearly regularly spaced yellow vertical intensity ridges appearing in Figure 6 b) may indicate an array of hot spots appearing at the top or bottom surface of the grain investigated. Notably the local strain would be substantially larger than the 10^{-3} indicated, as the figure is a projection over the entire grain.

4.3. *d-spacing decrease close to the cathode/electrolyte interface*

The observed decrease in *d*-spacing near the cathode side of the electrolyte at 24.7 hours at operating conditions is an unexpected result and presently there are no definitive mechanisms available to explain this phenomenon. A rigorous investigation for sources of experimental artefacts that could replicate this observation was performed. The relevant sources of error are associated with sample or detector drift during the course of the 24-hour scan. Investigation of potential drifts for each detector/sample coordinate axis however proved to be internally consistent. It was thus concluded, within the resolution limits, that the potential artefacts do not explain the magnitude of the observed change in lattice parameter in Figure 5.

We speculate that the effect of *d*-spacing decreasing may be related to an increase in oxygen vacancy concentration close to the cathode region and/or the cathode itself. Studies by Ruh and Garret (29) have revealed a decrease in the unit cell volume of oxygen-deficient ZrO_2 when firing and quenching it at high temperature. It is suggested in their work that the decrease of lattice parameter is due to oxygen missing rather than additional Zr in the structure. More recently,

Marrocchelli et al. (30) concluded that oxygen vacancy formation results in a decrease of lattice parameter due to electrostatic interactions, based on atomic scale computer simulations by molecular dynamics and density functional theory using ZrO_2 . According to their calculations, when doping with Sc, the chemical expansion coefficient is negative, resulting in a decrease of the lattice parameter, hence a chemical contraction. However, in their work the chemical expansion/contraction was not investigated under realistic SOC operating conditions.

If the oxygen reduction rate at the cathode/electrolyte interface is limited, insufficient oxide ions will be supplied via the electrolyte to the anode. In this case, it is reasonable to assume that oxygen from the ScYSZ lattice can be extracted in order to maintain the electrochemical reaction, promoting an oxygen deficiency in the structure close to the cathode. Causes for oxygen deficiency could be potentially related to the following mechanisms: a decrease in TPB length due to coarsening of LSM phase (31), oxygen depletion due to gas diffusion limitation in the LSM cathode (32) or partial delamination and/or microcracks at the cathode/electrolyte interface.

This oxygen deficiency or increase in oxygen vacancy concentration in the electrolyte region close to the cathode may explain the large decrease of d-spacing after 24.7 hours under operating conditions. In addition, the negligible d-spacing change at 17h@2V in comparison to 0h@2V close to the cathode/electrolyte interface region may indicate a threshold time in which oxygen vacancy concentration starts to increase, shown in the right side of the plot in Figure 5.

4.4. Instrumental outlook

A strength of the set-up used is the ability to swap between strain mapping at the scale of the device (Figure 5) and dark field microscopy at the scale of a grain (Figure 6). With the ad hoc set up used at the time of this experiment, the scans in Figure 5 took 70 minutes while the microscopy scans took approximately 16 minutes. However, periodically relocating the same grain in reciprocal and real space and finding new grains took several hours, which is not convenient in a beamtime period of a few days. Since the experiment, a dedicated instrument has been commissioned and the time for alignment is much reduced. Hence, it is now realistic to perform dark field microscopy on several grains interchangeably during an annealing, thus improving statistics and insight.

Furthermore, with the upgrade of ESRF to become an ultimate storage ring in 2020, we anticipate that scan times can be reduced by an order of magnitude. This will make it feasible to reduce the height of the incoming beam to say $1\ \mu\text{m}$, and to scan the grain of interest with respect to the beam. In this way, one would replace 2D projections of a grain – as shown in Figure 6 - with a real 3D grain map.

5. Conclusions

Solid oxide cells are organized structurally on multiple length scales. To understand degradation mechanisms and verify materials models it is of interest to develop *non-destructive* tools for multiscale structural characterization, enabling to zoom in and out in 3D in an actual device during an experiment. To our knowledge, this study is the first demonstration of such a tool. Two novel synchrotron methods are combined for use on SOCs. On the device scale, classical x-ray powder diffraction is replaced by strain mapping using multigrain crystallography methods, in order to overcome the problem of grain statistics. On the grain scale, we introduce dark field x-ray microscopy. Targeting the question of void formation and delamination during operation at high polarization, the x-ray methods are combined with extensive SEM post mortem studies.

The ScYSZ electrolyte based cells were tested at 700, 800 and 900 °C during 6 to 72 hours of operation at 2 V in air. For the first time void formation was shown to form as early as 6 hours in ScYSZ. These appeared at the grain boundaries close to the anode/electrolyte interface and also surrounding pinholes. For 6 μ m-ScYSZ correlations were found for void occurrences and maximum observed depth with increasing temperature at equivalent operando times between 24 and 72 hours.

The x-ray studies provide a coherent picture of the degradation mechanism taking place within the electrolyte near the anode/electrolyte interface. Within the grains, dark field X-ray microscopy showed an increase in local compressive strain inside the projection of the grain and rotated regions at the edges after 10.5 hours - both consistent with strain localization at the boundary of the grain. After 17 hours this phenomenon is evident as an increase in the grain average axial strain in a 100 μ m region near the interface. Thus void formation, as evidenced by the post mortem SEM study, leads to lattice strain.

An unexpected decrease of electrolyte d-spacing close to the cathode interface was observed and is tentatively associated to an increase of oxygen vacancy concentration in this region due to oxygen deficiency caused by degradation factors occurring at the cathode. Further investigations need to be made in order to elucidate the responsible mechanism.

Acknowledgements

The authors would like to thank ESRF for granting the beamtime and DTU DANCHIP for manufacturing the X-ray condenser lenses used at beamline ID06. We also acknowledge financial support from the ERC Advanced Grant, d-TXM and travel support for synchrotron experiments via

the DANSCATT grant from the Danish Council for Independent Research. We thank Sonja R. Ahl, Karin V. Hansen, Torben Jacobsen, Mogens B. Mogensen, Ming Chen, Christodoulos Chatzichristodoulou and Bhaskar Reddy for stimulating discussions; and technicians at DTU Energy: E. Abdellahi, A. Mikkelsen and J. Johnson for their support on sample preparation and experiments. We also thank Innokenty Kantor for his support during beamtime.

6. Bibliography

1. *Solid Oxide Fuel Cell Technology*. **Huang, K. and Goodenough, J. B.** 2009, Woodhead Publishing.
2. *Eliminating degradation in solid oxide electrochemical cells by reversible operation*. **Graves, C., et al.** 2014, *Nature Materials*, pp. 239-244.
3. *High Temperature Electrolysis in Alkaline Cells, Solid Proton Conducting Cells, and Solid Oxide Cells*. **Ebbesen, S. D., et al.** 2014, American Chemical Society, pp. 10697-10734.
4. *Solid Oxide Electrolysis Cells: Degradation at High Current Densities*. **Knibbe, R., et al.** 2010, *Journal of The Electrochemical Society*, pp. 1209-1217.
5. *Degradation phenomena in a solid oxide electrolysis cell after 9000 h of operation*. **Tietz, F., et al.** 2013, *Journal of Power Sources*, pp. 129-135.
6. *Durability of Solid Oxide Electrolysis Cell and Interconnects for Steam Electrolysis*. **Sun, X., et al.** 1, 2013, *The Electrochemical Society*, Vol. 57, pp. 3229-3238.
7. *The Course of Oxygen Partial Pressure and Electric Potentials across an Oxide Electrolyte Cell*. **Jacobsen, T. and Mogensen, M.** 2008, *The Electrochemical Society*, pp. 259-273.
8. *Understanding degradation of solid oxide electrolysis cells through modeling of electrochemical potential profiles*. **Chatzichristodoulou, C., et al.** 2016, *Electrochimica Acta*, pp. 265-282.
9. *Mechanism of oxygen electrode delamination in solid oxide electrolyzer cells*. **Virkar, A. V.** s.l. : Elsevier Ltd, 2010, *International Journal of Hydrogen Energy*, Vol. 35, pp. 9527-9543.
10. *Oxygen permeation flux through $10\text{Sc}1\text{YSZ-MnCo}2\text{O}_4$ asymmetric membranes prepared by two-step sintering*. **Pirou, S., et al.** 2016, *Fuel Processing Technology*, Vol. 152, pp. 192-199.
11. *Analysis of Electric Properties of $\text{ZrO}_2\text{-Y}_2\text{O}_3$ Single Crystals Using Terahertz IR and Impedance Spectroscopy Techniques I*. **Artemov, V. G., et al.** 7, 2014, *Russian Journal of Electrochemistry*, Vol. 50, pp. 690-693.
12. *Preparation of Yttria-Stabilized Zirconia by the Reverse Microemulsion Method and the Effect of Sc and Ce Doping on Microstructure and Ionic Conductivity for Solid Oxide Fuel Cell Applications*. **Oksuzomer, F., et al.** 2011, *International Journal of Applied Ceramic Technology*, pp. 42-48.
13. *Investigation of scandia–yttria–zirconia system as an electrolyte material for intermediate temperature fuel cells - influence of yttria content in system $(\text{Y}_2\text{O}_3)_x(\text{Sc}_2\text{O}_3)_{(11-x)}(\text{ZrO}_2)_{89}$* . **Politova, T. I. and Irvine, J. T. S.** 2004, *Solid State Ionics*, pp. 153-165.
14. *Co-doping of scandia–zirconia electrolytes for SOFCs*. **Irvine, J. T. S., et al.** 2006, *The Royal Society of Chemistry*, Vol. 134, pp. 41-49.
15. *Dark-field X-ray microscopy for multiscale structural characterization*. **Simons, H., et al.** 2015, *Nature Communications*, pp. 1-6.
16. *Multiscale 3D characterization with dark-field x-ray microscopy*. **Simons, H., et al.** 2016, *MRS Bulletin*, Vol. 4, pp. 454-459.
17. *Influence of oxygen partial pressure on surface tension of molten silver*. **Ozawa, S., et al.** 2010, *Journal of Applied Physics*, Vol. 107, pp. 014910-1 - 014910-7.

18. *YSZ-Based Oxygen Sensors and the Use of Nanomaterials: A Review from Classical Models to Current Trends*. **Lopez, C., Ramos, F. M. and Cirera, A.** 2009, Journal of Sensors, Vol. 2009, p. 15.
19. *Three-Dimensional X-Ray Diffraction Microscopy - Mapping Polycrystals and their Dynamics*. **Poulsen, H. F.** 2004, Springer, Vol. 205.
20. *Tutorial and source code of ImageD11*. **Wright, J.** s.l. : sourceforge, <https://github.com/jonwright/ImageD11>.
21. *X-ray diffraction microscopy based on refractive optics*. **Poulsen, H. F., et al.** 2017, Journal of Applied Crystallography, Vol. 50, pp. 1441-1456.
22. *Dark field X-ray microscopy for studies of recrystallization*. **Ahl, S. R., et al.** 2015, Materials Science and Engineering.
23. *Average Grain Size in Polycrystalline Ceramics*. **Mendelson, M. I.** 1969, Journal of the American Ceramic Society, pp. 443-446.
24. *Electrolyte degradation in anode supported microtubular yttria stabilized zirconia-based solid oxide steam electrolysis cells at high voltages of operation*. **Laguna-Bercero, M. A., et al.** 2011, Journal of Power Sources, pp. 8942-8947.
25. *Quantitative Stereology*. **Underwood, E. E.** 1970, Addison-Wesley.
26. *Degradation mechanism of electrolyte and air electrode in*. **Kim, J., et al.** 2013, International Journal of Hydrogen Energy, pp. 1225-1235.
27. *High temperature mechanical properties of zirconia tapes used for electrolyte supported solid oxide fuel cells*. **Fleischhauer, F., et al.** 2015, Journal of Power Sources, Vol. 273, pp. 237-243.
28. *Failure mechanism of (La Sr) MnO₃ oxygen electrodes of solid oxide electrolysis cells*. **Chen, K. and Jiang, S. P.** 36, 2011, International Journal of Hydrogen Energy, pp. 10541-10549.
29. *Nonstoichiometry of ZrO₂ and its relation to tetragonal-cubic inversion in ZrO₂*. **Ruh, R. and Garret, H. J.** 5, 1967, Journal of the American Ceramic Society, Vol. 50, pp. 257-261.
30. *Understanding Chemical Expansion in Non-Stoichiometric Oxides: Ceria and Zirconia Case Studies*. **Marrocchelli, D., et al.** 2012, Advanced Functional Materials, Vol. 22, pp. 1958-1965.
31. *Particle Coarsening Influence on Oxygen Reduction in LSM-YSZ composite Materials*. **Farlenkov, A. S., et al.** 1, 2015, Fuel Cells, Vol. 15, pp. 131-139.
32. *Impedance of Solid Oxide Fuel Cell LSM/YSZ Composite Cathodes*. **Jørgensen, M. J. and Mogensen, M.** 5, 2001, Journal of The Electrochemical Society, Vol. 148, pp. A433-A442.